SANDIA REPORT
S A N D 2 0 0 6 - 7 0 2 0
Unlimited Release
Printed November 2006

Superhydrophobic Surface Coatings for Microfluidics and MEMs

Eric D. Branson, Seema Singh, Jack E. Houston, Frank van Swol, and C. Jeffrey Brinker

Prepared by
Sandia National Laboratories
Albuquerque, New Mexico 87185

Sandia is a multiprogram laboratory operated by Sandia Corporation,
a Lockheed Martin Company, for the United States Department of Energy's
National Nuclear Security Administration under Contract DE-AC04-94AL85000.

Issued by Sandia National Laboratories, operated for the United States Department of Energy by Sandia Corporation.

Available to DOE and DOE contractors from
U.S. Department of Energy
Office of Scientific and Technical Information
P.O. Box 62
Oak Ridge, TN 37831

Telephone: (865) 576-8401
Facsimile: (865) 576-5728
E-Mail: reports@adonis.osti.gov
Online ordering: http://www.osti.gov/bridge

Available to the public from
U.S. Department of Commerce
National Technical Information Service
5285 Port Royal Rd.
Springfield, VA 22161

Telephone: (800) 553-6847
Facsimile: (703) 605-6900
E-Mail: orders@ntis.fedworld.gov
Online order: http://www.ntis.gov/help/ordermethods.asp?loc=7-4-0#online

SANDIA REPORT
S A N D 2 0 0 6 - 7 0 2 0 xx
Unlimited Release
Printed November 2006

Superhydrophobic Surface Coatings for Microfluidics and MEMS

Eric D. Branson [a], Seema Singh [a], Jack E. Houston [b], Frank van Swol [b,d], C. Jeffrey Brinker [c,e]

[a] Ceramic Processing and Inorganic Materials Department, Sandia National Laboratories, PO Box 5800, Albuquerque, NM 87185-1349

[b] Surface and Interface Sciences Department, Sandia National Laboratories, PO Box 5800, Albuquerque, NM 87185-1415

[c] Self-Assembled Materials Department, Sandia National Laboratories, PO Box 5800, Albuquerque, NM 87185-1349

[d] Chemical & Nuclear Engineering Department, University of New Mexico, Albuquerque, NM 87106

[e] Chemical & Nuclear Engineering Department, Center for Micro-Engineered Materials, University of New Mexico, Albuquerque, NM 87106

Abstract

Low solid interfacial energy and fractally rough surface topography confer to Lotus plants superhydrophobic (SH) properties like high contact angles, rolling and bouncing of liquid droplets, and self-cleaning of particle contaminants. This project exploits the porous fractal structure of a novel, synthetic SH surface for aerosol collection, its self-cleaning properties for particle concentration, and its slippery nature

to enhance the performance of fluidic and MEMS devices. We propose to understand fundamentally the conditions needed to cause liquid droplets to roll rather than flow/slide on a surface and how this “rolling transition” influences the boundary condition describing fluid flow in a pipe or micro-channel. Rolling of droplets is important for aerosol collection strategies because it allows trapped particles to be concentrated and transported in liquid droplets with no need for a pre-defined/micromachined fluidic architecture. The fluid/solid boundary condition is important because it governs flow resistance and rheology and establishes the fluid velocity profile. Although many research groups are exploring SH surfaces, our team is the first to unambiguously determine their effects on fluid flow and rheology. SH surfaces could impact all future SNL designs of collectors, fluidic devices, MEMS, and NEMS. Interfaced with inertial focusing aerosol collectors, SH surfaces would allow size-specific particle populations to be collected, concentrated, and transported to a fluidic interface without loss. In microfluidic systems, we expect to reduce the energy/power required to pump fluids and actuate MEMS. Plug-like (rather than parabolic) velocity profiles can greatly improve resolution of chip-based separations and enable unprecedented control of concentration profiles and residence times in fluidic-based micro-reactors. Patterned SH/hydrophilic channels could induce mixing in microchannels and enable development of microflow control elements.

Acknowledgements

This work was funded by Sandia National Laboratory’s Laboratory Directed Research & Development program (LDRD). Some coating processes were conducted in the cleanroom facility located at the University of New Mexico’s Center for High Technology Materials (CHTM). SEM images were performed at UNM’s Center for Micro-Engineering on equipment funded by a NSF New Mexico EPSCoR grant.

Table of Contents

Introduction

This is a concluding SAND report of the three year LDRD project # 73185. It is divided into chapters focusing on the six main research themes explored during the course of this project: 1) Synthesis and patterning of superhydrophobic surfaces, 2) Neutron Reflectivity of superhydrophobic/water interfaces, 3) Slip on superhydrophobic surfaces, 4) Characterization of slip using acoustic wave techniques, 5) Cavitation and long range hydrophobic interactions probed by interfacial force microscopy, and 6) Cavitation Analysis. Each chapter is self contained and has its own figures, tables, references and conclusions. The Supplementary Information section includes research that was not included in the chapters 1-6 but that is relevant to the project goals.

Chapter 1. Synthesis and Patterning of Super-hydrophobic Films

Introduction

Over the last decade there has been a growing interest in superhydrophobic (SH) surfaces stimulated by a wide range of potential applications. It has been suggested that contamination, corrosion, oxidation, current conduction and flow resistance can all be reduced on superhydrophobic surfaces[1] where superhydrophobicity is loosely defined as contact angles of H_2O exceeding ~ 150º. The waxy micro and nano structured topography found on plant surfaces, makes water droplets roll rather than flow.[2, 3] The rolling droplet picks up dust and contaminants thereby cleaning the leaf's surface. This phenomenon has spurred industrial applications such as self cleaning windows and water repellent fabrics.[4,5] However previous approaches to SH surfaces are complicated and often surface specific. A need exists for simple SH coating procedures that are applicable to arbitrary surfaces.

The Young's equation describes the geometry of a liquid droplet on a flat (smooth) solid surface. The contact angle (θ) of a liquid droplet on a smooth solid surface is given by:

$$\cos\theta = \frac{\gamma_{sv} - \gamma_{sl}}{\gamma_{lv}} \qquad (1)$$

where γ_{sl}, γ_{sv}, and γ_{lv} are the interfacial free energy per unit area of the solid-liquid, solid-vapor, and liquid-vapor interfaces, respectively. However, this equation can be applied only to smooth surfaces. Wenzel, and Cassie-Baxter proposed different modifications to the Young's equation in order to apply it to rough surfaces.[6-8] Wenzel modified Young's equation by introducing a dimensionless roughness factor r ($r \geq 1$), which is defined as the ratio of the actual area of a rough surface to the projected area.

$$\cos\theta' = \frac{r(\gamma_{sv} - \gamma_{sl})}{\gamma_{lv}} = r\cos\theta \qquad (2)$$

Here θ indicates the intrinsic contact angle of a smooth sample, and θ' indicates the macroscopic contact angle. Cassie-Baxter considered the contact angle θ' on a

heterogeneous surface composed of two different materials. When a unit area of the surface has a surface area fraction f_1 with a contact angle θ_1 and an area fraction f_2 with a contact angle θ_2, the contact angle on the surface can be expressed as a linear combination:

$$\cos\theta' = f_1 \cos\theta_1 + f \cos\theta_2 \quad (3)$$

For a SH surface, material #2 will be trapped air/ vapor, and hence θ_2 = 180° Thus using $f_2 = 1 - f_1$ and dropping the subscripts one gets

$$\cos\theta' = -1 + f(1 + \cos\theta) \quad (4)$$

where f is the fraction of the projected area that is in contact with liquid.[9,10] While the Wenzel equation is valid when the liquid droplet enters the valleys and completely wets the surface topography, the Cassie-Baxter model requires the presence of a liquid-vapor interface below the droplet[11]. At constant surface roughness, the surface chemistry can be designed to
convert the contact angle behavior from the Wenzel regime to the Cassie-Baxter regime.[12]

In recent years, SH surfaces have been prepared by various methods such as solidification of alkylketene dimer (AKD),[13] vacuum deposition of PTFE thin films,[14] anodic oxidation of aluminum surfaces,[15] mixing of a sublimation material with silica or bohemite,[16] plasma polymerization,[17,18] pulsed plasma deposition of nanospheres,[19] a porous microsphere/nanofiber composite film,[20] by dissolution of polymers with rapid cooling,[21] densely packed aligned carbon nanotubes,[22] aligned polyacrylonitile nanofibers,[23] the sol-gel process to make SH foams,[24] and lithographic patterning of silicon wafers.[25]

In most of the cited cases, the synthesis procedure is quite complex and can not be deposited on various surfaces by simple coating techniques such as – spray, dip or spin. We have developed a simple, evaporation-driven procedure to deposit SH coatings on arbitrary surfaces. The advantage of our approach compared to many others is that our SH surfaces form by (evaporation-induced) reassembly from a very low viscosity sol under standard laboratory conditions. This makes our procedure amenable to coating small features and virtually any kind of substrate. Applied to

plastic, glass, paper, textile and silicon substrates, our SH coatings are optically transparent with contact angles exceeding 155°. In addition, we have developed a lithographic technique enabling optical adjustment of the water contact angle from 170° to < 10°.[12]

Experimental methods

Sol preparation

Tetramethylorthosilicate (TMOS) along with 3,3,3-trifluoropropyltrimethyoxysilane (TFPTMOS) was used as silica precursor to make the SH coatings. In a typical preparation of the alcogel, TMOS, methanol, ammonium hydroxide (35% NH3), TFPTMOS, and deionized water were mixed in a molar ratio of 1:41.56:0.003:0.33:5.85. The mixture was stirred for 10 minutes and aged for 48 hours at 50°C. After aging, the gelled mixture was subjected to two cycles of pore-fluid exchange by methanol in space of two hours. It was then subjected to similar pore-fluid exchange cycles with hexane. The gel was then kept immersed in a 5% by volume of hexamethyldisilazane (HMDS) in hexane for 22 hours at 50°C to achieve surface derivatization of the hydroxyl groups. The gel was washed with hexane twice in two hours, and then twice with ethanol in the next two hours. The gel was diluted with 1:1 ethanol and kept for sonication for reliquefication. Ethanol was added at various intervals to maintain the same level of the fluid. The re-dispersed sol was filtered through a 1-micron glass fiber filter. Filtered sol was ready for spin, dip or spraycoat.[26] Here with, we will refer to this sol's film or powder as TF1; similarly films and powder prepared without TFPTMOS will be referred to as TM1.

Film preparation

While coating the substrate on a Si wafer or glass slide, the sol was diluted with different solvents to get films with varying thickness. The films were heated to 100°C for 15 minutes to remove residual alcohol. Top surface derivatization was achieved by treatment with HMDS vapor for 10 minutes at 100°C.

Characterization

The materials were characterized by small-angle X-ray scattering (SAXS), Scanning electron microscopy (SEM), transmission electron microscopy (TEM), scanning force microscopy (SFM), nuclear magnetic resonance (NMR), infrared spectroscopy (FTIR), contact angle measurement, nitrogen sorption analysis, and thermogravimetric / differential thermal analysis (TGA/DTA).

SAXS equipment

Both bulk materials and thin-film samples were analyzed to determine fractal nature of the material by small-angle X-ray scattering (SAXS) on the pinhole rotating-anode instrument Rotaflex, Rigaku, 4 kW, CuKα wavelength. A special sample holder was constructed and utilized to study thin film samples in grazing incidence geometry (GISAXS). In this way, it was possible to adjust the angle of incidence of the primary X-ray beam to approach the angle of total reflection of thin-film samples, thereby obtaining maximum scattering intensity. A 2D wire detector was used, and the sample was kept under vacuum during the measurement. The range of available values for the scattering vector s was s = 0.05-1.4 nm^{-1}, where $s = 2\sin(\theta)/\lambda$, 2θ is the scattering angle, and λ is the CuKα wavelength. The large range of s values was achieved by varying the sample-detector distance.

Other characterization techniques

Scanning electron microscopy (SEM) was performed on a Hitachi S-5200 Nano SEM. Transmission electron microscopy (TEM) measurements were performed on a JEOL 2010 microscope to investigate the internal fractal structure of the aerogel film. Scanning force microscopy (SFM) measurements were performed on a Digital Instruments Nanoscope IIIa SPM Controller (noise < 0.3 Å RMS in vertical, i.e. z-dimension, with vibration isolation) in contact mode.[12] VCA Optima XE 2500 was used to measure advancing and receding contact angles. NMR spectra were obtained on a

Bruker Avance 400 using a 2.5 mm MAS probe spinning between 28 and 35 kHz. The nitrogen sorption experiments were carried out at 77 K using an Autosorb-1 from Quantachrom Instruments (Florida, USA). Water sorption experiments were performed using a "Hydrosorb" instrument of Quantachrom Instruments (Florida, USA) at various temperatures. FTIR data were obtained on a Bruker Vector 22 Instrument using KBr pellets under an atmosphere of flowing nitrogen to study surface chemical modification of the material. The thermal stability of the SH powder was studied by thermogravimeter and differential thermal analyzer (DTA) SDT 2960 TA universal instruments, USA.

Results and discussion

SAXS evaluation

In general, SAXS data on aerogel materials provide less information on the mass distribution and the nature of the interface between the pores and the void on the nanometer scale. Usually, aerogels do not show distinct reflections ("peaks") in SAXS, but still the analysis of the asymptotic behavior of such featureless curves at larger *s* allows for a determination of the average pore size and of local curvature properties, in particular the fractality of the pore system. While sharp interfaces between the pores and voids produce an asymptotic behavior of $I(s) \propto s^{-4}$ (Porod's law), where *I (s)* is the scattering intensity as a function of the scattering vector *(s),* fractal pore morphologies show $I(s) \propto s^{-v}$ with $1 < v < 3$ for mass fractals and $3 < v < 4$ for surface fractals.[27] In the present case, significant differences are observed depending on the nature of the materials. Sample TM1 (aerogel powder) exhibits almost perfect Porod's law behavior over a wide range of scattering vectors, suggesting a well-defined and sharp pore interface. In contrast, sample TF1 film and powder both exhibited a significant deviation from Porod's law with $s^{-2.7}$ and $s^{-2.3}$ (figure 1) respectively, which is consistent with a mass fractal behavior. In essence, our SAXS results suggest that, under comparable preparation conditions, a larger hydrophobicity of the porous silica also corresponds to a larger deviation from the ideal Porod's law, indicating a higher degree of "fractality". Interestingly, only a few studies have addressed a possible relationship between the

fractality and hydrophobicity of porous silicas obtained by sol-gel methods. Sun et al. reported a systematic study on different hydrophobic silanes.[28] More importantly, Okabayashi and coworkers performed detailed SAXS studies on fluoro-containing silanes and reported mass fractals for corresponding porous silicas, obtained from an acid-catalyzed sol-gel process.[29] It has been suggested that the fractality of such materials can be attributed to a different hydrolysis, while the condensation may not be the crucial step. Since hydrolysis is based on an electrophilic attack to the Si atom, bulky substituents such as the trifluoropropyl group could perhaps provide a substantial steric effect, impeding the formation of dense, smooth "non-fractal" surfaces. Further systematic studies are needed to clarify if indeed the hydrophobicity of the silica precursors directly affects the final fractality of the porous material.

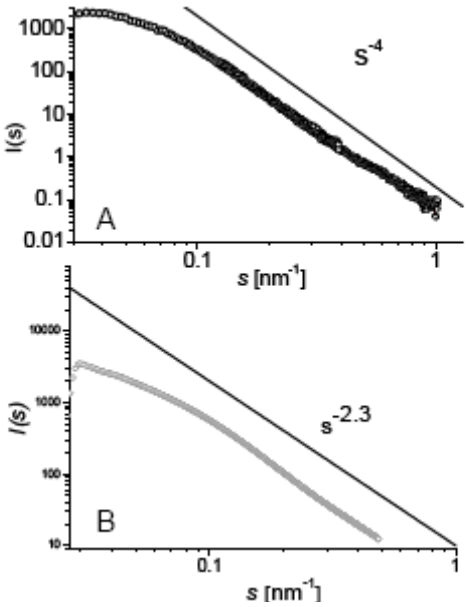

Figure 1: SAXS scattering curves, A- TM1 hydrophobic aerogel powder, B- TF1 SH powder

Sorption analysis

The TF1sample was studied by nitrogen physisorption at 77 K and water sorption at 25ºC to determine the porosity and the hydrophobicity of the pore walls. N_2 sorption revealed a significant uptake, corresponding to a quite high total pore volume of 0.95ml/g and a BET surface area of ca. 850 m^2/g (figure 2).

The adsorption and desorption branches did not coincide at low relative pressures; this hysteresis could not be eliminated by applying longer equilibration times and

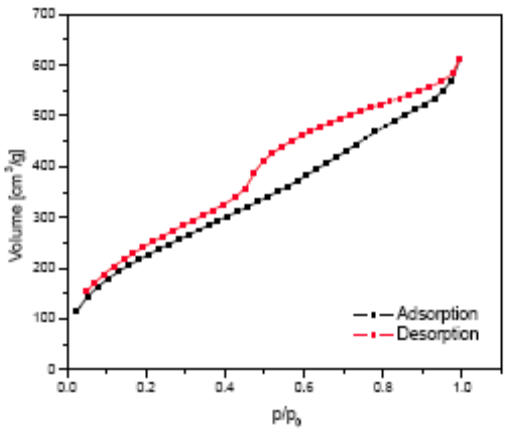

Figure 2: Nitrogen sorption of sample TF1at 77 K

which is frequently observed for organically modified silicas. This effect is probably due to the flexibility of the organic moieties, causing changes in the skeleton density under these conditions. Taking into account the peculiarity of the adsorption and desorption branches, the average pore size was determined as 4V/A, where V is the total pore volume and A is the BET surface area, providing a formal average mesopore size of ca. 4.5 nm. However, the adsorption branch already indicates a quite broad pore size distribution, in accordance with fractal pore morphology. The step in the desorption branch can be attributed to either cavitation or pore blocking effect, and therefore probably does not reflect the complete emptying of pores of a well-defined size. Water sorption experiments were performed at room temperature (25 °C) to study the uptake of a hydrophilic adsorbate. However, the material showed only a very weak total uptake of ca. 0.01 ml/g, even upon a variation of the equilibrium time. This low value for water adsorption results from the outer surface of the grains, but not from true micro- or mesoporosity. Taking into account the marked accessible porosity obtained from nitrogen sorption, and the significant time of the sorption experiment (ca. 5 h), this experiment provides an evidence of pronounced hydrophobicity of the pore surface, which makes the material almost inaccessible to water.

NMR

There are 5 ^{1}H resonances observed in the NMR spectrum of dry TF1 powder. The data shown in figure 3 clearly indicates that there was no water present in the initial film or after 24 hours exposure to the water because there is no peak observed at δ ~ 4.5 ppm. Again, there is no indication of Si-OH group, which typically appears around ~ 1.3 ppm. Considering these data it can be inferred that there was no chemical change due to exposure of water – i.e. none of the chemical species are significantly converted to new species. However, the spectrum did shift 1ppm towards the left without any significant changes

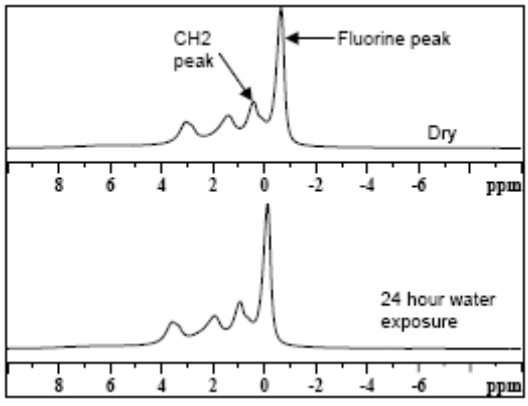

Figure 3: Spectra for the $_{1}$H MAS NMR for the TF1powder for different exposure conditions

in the peaks. This result conforms to the water sorption observations.

Contact angle measurements and Self cleaning behavior

Sessile drop contact angle measurements on SH films of thickness 500-600 nm, indicate an apparent water contact angle of 164 ± 2° (figure 4). We have observed high contact angles of around 158 ± 2° even for very thin SH films (37-50 nm). However, thick SH films show reduced contact angle hysteresis (6-7°) compared too thin SH films (15-20°). This phenomenon is relevant to determining the minimum thickness / roughness requirement for low sliding angles. The effect of various thickness /roughness parameters of SH film topic will be left for another communication.

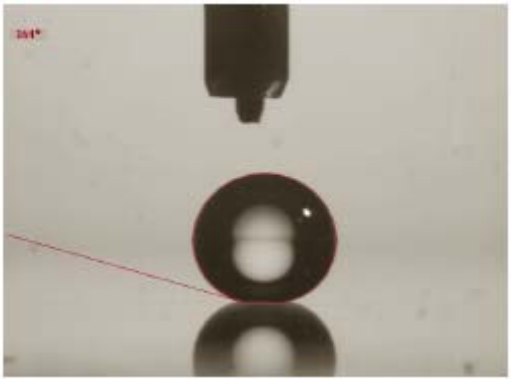

Figure 4: Representative image of a sessile drop measurement of water contact angle on a TF1 film showing a contact angle of 164±2°.

Self cleaning behavior

We performed various experiments to demonstrate that surfaces coated with a SH layer/film exhibit self-cleaning behavior similar to lotus leaves. Water droplets have the ability to roll on top of the surface, collecting any debris or impurities that have come to rest on the surface. As shown in figure 5A and 5B a water droplet captures the contaminant (eg. coffee / sugar) as it rolls over the surface and then carries the contaminant to a hydrophilic patterned collection point or completely off the surface.

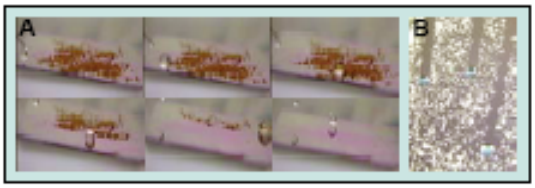

Figure 5: A: Coffee granules on SH surface (TF1) cleaned by water droplets, B: water droplets pick up sugar powder

SEM/TEM/SFM

Figures 6A and 6B show the SEM images of the film's cross section and the top

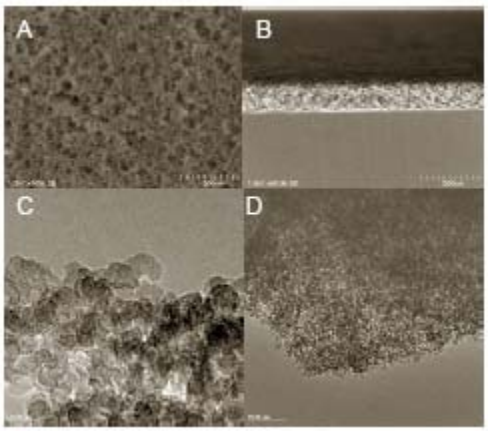

Figure 6: A/B: SEM image of a SH Film-TF1, C/D: TEM images of the SH film-TF1

surface. The scale and nature of roughness that imparts the film its SH character is evident from these images. TEM images (figures 6C and 6D) show the porous nature of the film. This open cell structure exhibits fractal porosity with a wide pore size distribution.

Scanning Force Microscope (SFM) was used to image SH surfaces and calculate roughness. The root mean square (RMS) roughness calculation is based on finding a median surface level for the image and then evaluating the standard deviation within the image. The expression for the surface roughness used in our study is:

$$R_Q = \sqrt{\frac{\sum_{i=1}^{N}\sum_{j=1}^{N}\left(H(i,j)-\overline{H}\right)^2}{N^2}}$$

where *i* and *j* are the x and y pixel locations on the SFM image, *H* is the average value of the height across the entire image and *N* is the number of data points in the image. SFM images were stored as 512 × 512 data arrays. Figures 7A and 7B show a representative 3D surface profile of our fractal SH surface and figure 7C shows 1D line roughness profile of a 445 nm thick SH film (figure 7A). The calculated RMS roughness is 39 nm with pillar like high aspect ratio features. In general, the SFM tip's shape and size will affect the roughness measurement and under-estimate the calculated roughness. However, a very sharp silicon cantilever was used (~15 nm) to minimize this type of effects. Interestingly, both 445 nm and 40 nm thick films gave surface roughness ranging from 27-39 nm. This may be dictated by the aerogel particle size. Multi-scale lotus leaf-like roughness appears to be important in achieving high contact angle (superhydrophobicity) and low rolling angle. Our SFM images clearly show micron scale terrain (figure 7A) with nanometer scale features (figure 7B and 7C), contributing to contact angle > 160°.

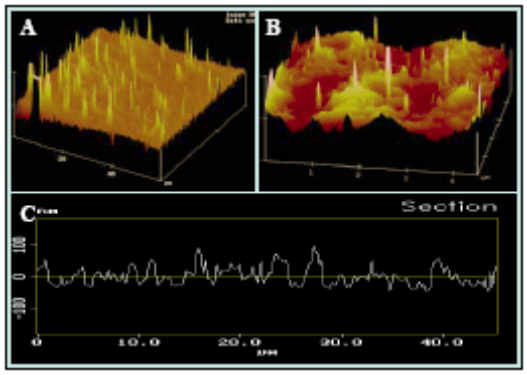

Figure 7: SFM Images: A: thick (445 nm) and B: thin (~40 nm) SH film (TF1) showing 3D surface profile of fractally rough surface. The height (z-scale) is 150 nm/div (A) / 25 nm/div (B). C: represents 1D section analysis showing roughness profile of figure 7A.

Patterning of SH coatings

An uncoated mercury grid lamp was utilized for the UV/Ozone treatment on SH coatings to vary contact angles between 160° and 15°, as illustrated in figure 8A. The complexity of patterning is limited only by the detail of the mask. Figure 8B shows the variation of the contact angle with exposure time to the UV light. Films exhibit lower contact angles after UV/Ozone treatment. Once re-treated with HMDS vapors the films recover contact angles back up to 150 degrees, almost entirely regaining the water repelling tendencies of the original SH films. SH films can also be patterned to create optically defined regions, such as micro channels or even more complicated patterns and images. These patterns allow exposed areas to become hydrophilic while the covered areas remain hydrophobic.

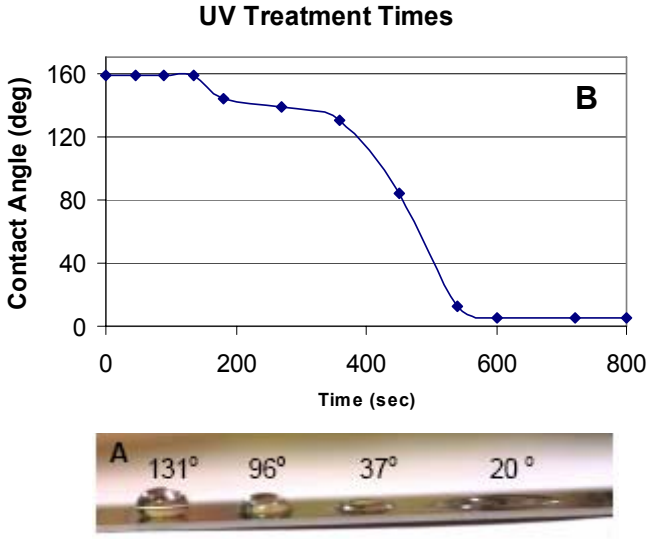

Figure 8: A) Controlled contact angles, B) Contact angles varying with UV exposure time.

FTIR

In order to study the change in surface chemistry upon UV/ozone treatment, FTIR spectra were gathered for SH powder (TF1) before and after UV/ozone exposure (figure 9). Before UV exposure strong peaks between

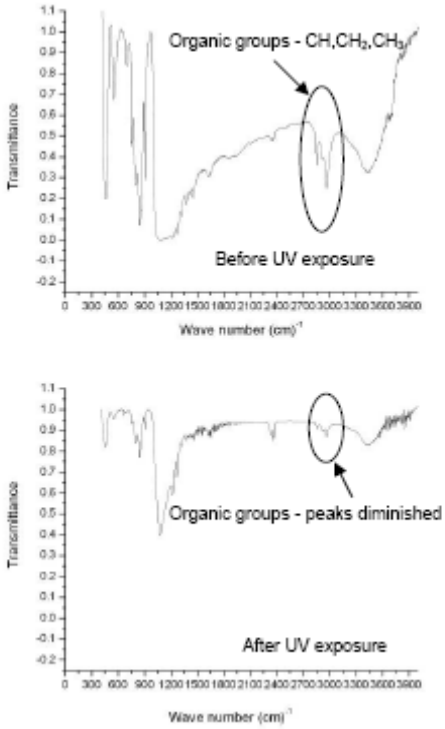

Figure 9: FTIR spectra of SH powder (TF1) before and after UV exposure

2750-2950 cm^{-1} wave numbers were observed.[30,31]

These peaks mainly represent CH, CH_2, and CH_3 groups. Some peaks between 1380 and 1460 cm^{-1} were also observed representing organic moieties such as CH_2 and CH3.[32] The peaks at 1270 and 840 cm^{-1} corresponds to Si–C bonds. The peak at 1100 cm^{-1} is due to Si–O–Si bonding.[32] The organic peaks were diminished after UV exposure for 10 minutes. UV light creates ozone in an oxygen environment and eventually ozone scavenges the organics from the surface of the material. The results of the FTIR studies confirm the contact angle measurements as shown in figure 8 A.

Thermogravimetric analysis

The TGA-DTA results for the SH powder (TF1) are depicted in figure 10. The resulting graphs (figure 10) are indicating that up to a temperature of 320°C, there was a very little weight loss, and further increase in temperature causes sudden weight loss, along with two strong exothermic peaks corresponding to the oxidation of organic (CH3/CF3) groups. The average bond energies required to break the C-H and C-F bond are 413 and 485 KJ/mol respectively,[33] so the first peak between 380-430°C possibly corresponds to breakage of all surface CH3 groups and second peak between 450-480°C corresponds to the mixture of CF_3 and CF_3-CH_2-CH_3 groups.

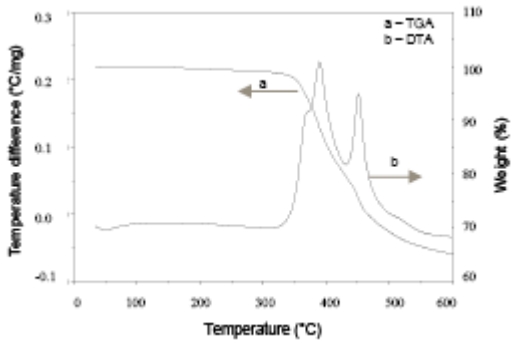

Figure 10: TGA and DTA analyses of SH powder (TF1)

After heating to a temperature of around 500°C, possibly all the organic groups are lost. This value is the same as the Si–C bond stability temperature (500°C).[34]

Conclusion

We have mimicked the surface texture of the well-known lotus leaf at the nano level by developing simple sol-gel technique. The inherent fractal and hydrophobic nature of SH film avoids the two step approach of creating roughness on the application surface and then applying hydrophobizing agents. With a similar synthesis procedure,

precursor TMOS alone does not produce a fractal surface, while mixing with TFTMOS, it produces a fractal powder as well as fractal films. Self cleaning behavior of our SH coating indicates high contact angle with low contact angle hysteresis. SH-film thicknesses of 37-50nm show high contact angle of around 158° and SFM images of both 445 nm and 40 nm thick SH-films show similar surface roughnesses ranging from 27-39 nm. Photocalcination procedures made SH surface to be patterned in various features ranging from microchannels to more complicated patterns and images. These patterned surfaces were made hydrophobic once again by treating them with HMDS. Simple evaporation driven coating system and adherence to various substrates inspires us to investigate more specific issues such as corrosion resistance, bio-fouling and micro mixing.

References

1. Lin Feng, S. L., Yingshun Li, Huanjun Li, Lingjuan Zhang, Jin Zhai, Yanlin Song, Biqian Liu, Lei Jiang, and Daoben Zhu, Superhydrophobic surfaces from natural to artificial. *Advanced Materials* **2002,** 14, (24), 1857-1860.
2. Barthlott, W.; Neinhuis, C., Purity of the sacred lotus, or escape from contamination in biological surfaces. *Planta (Heidelberg)* **1997,** 202, (1), 1.
3. Neinhuis, C.; Barthlott, W., Characterization and distribution of water-repellent, self-cleaning plant surfaces. *Annals of Botany (London)* **1997,** 79, (6), 667.
4. Inoue, Y., Recent technological trends with ultrahydrophobic surfaces. *Journal of Japanese Society of Tribologists* **2002,** 47, (5), 353.
5. Blossey, R., Self-cleaning surfaces – virtual realities. *Nature Materials* **2003,** 2, (5), 301.
6. Cassie, A. B. D., CONTACT ANGLES. *Discussions of the Faraday Society* **1948,** 3, 11.
7. Cassie, A. B. D.; Baxter, S., Wettability of porous surfaces. *Transactions of Faraday Society* **1944,** 40, 546-551.
8. Wenzel, R. N., Resistance of solid surfaces to wetting by water. *Industrial and Engineering Chemistry* **1936,** 28, (8), 988.
9. Bico, J., Thiele, U., Quere, D., Wettting of textured surfaces. *Colloids and Surfaces A (Physicochemical and Engineering Aspects)* **2002,** 206, 41-46.
10. Patankar, N. A., On the Modeling of Hydrophobic Contact Angles on Rough Surfaces. *Langmuir* **2003,** 19, 1249-1253.
11. Bico, J.; Marzolin, C.; Quere, D., Pearl drops. *Europhysics Letters* **1999,** 47, (2), 220. 12. Doshi, D. A.; Shah, P. B.; Singh, S.; Branson, E. D.; Malanoski, A. P.; Watkins, E. B.; Majewski, J.; van Swol, F.; Brinker, C. J., Investigating the interface of superhydrophobic surfaces in contact with water. *Langmuir* **2005,** 21, (17), 7805.

13. Onda, T.; Shibuichi, S.; Satoh, N.; Tsujii, K., Super-water-repellent fractal surfaces. *Langmuir* **1996,** 12, (9), 2125.
14. Miller, J. D., Veeramasuneni S, Drelich J, *Polymer Engineering and Science* **1996,** 36, (14), 1849-1855.
15. Tsujii, K.; Yamamoto, T.; Onda, T.; Shibuichi, S., Super oil-repellent surfaces. *Angewandte Chemie-International Edition in English* **1997,** 36, (9), 1011.
16. Nakajima, A., Fujishima, A., Hashimoto, K.,Watanbe, T., *Advanced Materials* **1999,** 11, 1365.
17. Shirtcliffe, N. J., Thiemann, P., Stratmann, M.,Grundmeier, G., *Surface & Coatings Technology* **2001,** 142, 1121-1128.
18. Coulson, S. R., Woodward, I., Badyal,J.P.S., Brewer, S.A.,Willis, C., *Phys.Chem.B* **2000,** 104, (37), 8836-8840.
19. D. O. H. Teare, C. G. S., P. Ridley, E. J. Kinmond, V. Roucoules, and J. P. S. Badyal, Pulsed Plasma Deposition of Super-Hydrophobic Nanospheres. *Chem. Mater.* **2002,** 14, 4566-4571.
20. Lei Jiang, Y. Z., Jin Zhai, A lotus-leaf-like Superhydrophobic Surface: A porous Microsphere/nanofiber composite film prepared by electrohydrodynamics. *Angewandte Chemie-International Edition* **2004,** 43, 4338-4341.
21. H. Yıldırım Erbil, A. L. D., Yonca Avcı,Olcay Mert, Transformation of a Simple Plastic into a Superhydrophobic Surface. *science* **2003,** 299, 1377-1379.
22. Kenneth K. S. Lau, † Jose´ Bico,‡ Kenneth B. K. Teo,§ Manish Chhowalla,| Gehan A. J. Amaratunga,§ William I. Milne,§ Gareth H. McKinley,‡ and Karen K. Gleason†, Superhydrophobic Carbon Nanotube Forests. *Nano Letters* **2003,** 3, (12),1701-1705.
23. Feng, L.; Li, S. H.; Li, H. J.; Zhai, J.; Song, Y. L.; Jiang, L.; Zhu, D. B., Super-hydrophobic surface of aligned polyacrylonitrile nanofibers. *Angewandte Chemie-International Edition* **2002,** 41, (7), 1221.
24. Shirtcliffe, N. J.; McHale, G.; Newton, M. I.; Perry, C. C., Intrinsically superhydrophobic organosilica sol-gel foams. *Langmuir* **2003,** 19, (14), 5626.
25. Oner, D., McCarthy, T. J., *Langmuir* **2000,** 16, 7777-7782.
26. Prakash, S. S.; Brinker, C. J.; Hurd, A. J., Silica aerogel films at ambient pressure. *Journal of Non-Crystalline Solids* **1995,** 190, (3), 264.
27. Smarsly, B. A., M.; Wolff, T., *chem. phys.* **2002,** 116, 2618.
28. Xu Y, W. D., Sun YH, Li ZH, Dong BZ, Wu ZH, *JOURNAL OF NON-CRYSTALLINE SOLIDS* **2005,** 35, (3), 258-266.
29. Ogasawara T, I. K., Hattori N, Okabayashi H, O'Connor CJ, *COLLOID AND POLYMER SCIENCE* **2000,** 278, (4), 293-300.
30. M. Laczka, K. C.-K., M. Kogut, *Journal of Non-Cryst. Solids* **2001,** 287, 10.
31. N. Hering, K. S., R. Riedel, O. Lichtenberger, J.Woltersodorf, *Appl. Organometal. Chem.* **2001,** 15, 879.
32. A. Venkateswara Rao, M. M. K., D.P. Amalnerkar, Tanay Seth, Superhydrophobic silica aerogels based on methyltrimethoxysilane precursor. *Journal of Non-Crystalline Solids* **2003,** 330, 187-195.
33. Brown, L., Bursten, *Chemistry, the central science*. sixth ed.; p 271/1045.
34. Powell, P., *Principles of Organometallic Chemistry*. Chapman and Hall: London, 1988; p. 2, 98.

Chapter 2. Investigating the Interface of Superhydrophobic Surfaces in Contact with Water

We all can recall seeing water droplets "bead up" on the leaves of plants. Most famous is the Lotus leaf, called the "symbol of purity" because of its self-cleaning properties. At very shallow angles of inclination or with the slightest wind, water droplets roll rather than flow.[1,2] The rolling droplets entrain particle contaminants and parasites, thereby cleaning them from the Lotus leaf surface. It is now recognized that the fascinating fluid behaviors observed for the Lotus plant, like the rolling and bouncing of liquid droplets and self-cleaning of particle contaminants, arise from a combination of the low interfacial energy and the rough surface topography of waxy deposits covering their leaves.[3]

Phenomenologically, Cassie and Baxter postulated that the cosine of the contact angle on a heterogeneous solid/air surface is the sum of the cosine of the contact angles of the respective homogeneous surfaces weighted by the surface fraction of the solid,[4,5] $\cos \theta^{\alpha} = -1 + \Phi_s (1 + \cos \theta)$, where θ^{α} is the apparent contact angle, -1 is the cosine of the contact angle of the air surface, and Φ_s is the surface fraction of solid. As the ratio of the pillar width to interpillar distance of a regular lithographically defined surface decreases[6] or the roughness of a random, porous (e.g., fractal) surface increases, Φ_s approaches zero, and θ^{α} approaches 180°. Interestingly, Herminghaus postulates that hierarchical roughness could render any surface (independent of microscopic contact angle) superhydrophobic[7], but this has not yet been observed. Wenzel had put forward a different relationship for contact angles on rough surfaces:[8] $\cos \theta^{\alpha} = r \cos \theta$, where r is the roughness parameter defined by the ratio of the real surface area to the projected surface area. Because $r \geq 1$, roughness on a hydrophobic surface ($\theta > 90°$) renders it more hydrophobic, whereas on a hydrophilic surface ($\theta < 90°$) roughness has the opposite effect, decreasing θ toward 0°. Although the Wenzel equation is valid when the liquid droplet enters the valleys and completely wets the surface topography, the Cassie – Baxter model requires the presence of a liquid-vapor interface below the droplet.[9] At constant surface roughness, the surface chemistry can

be designed to have the contact-angle behavior go from the Wenzel regime to the Cassie – Baxter regime.

Devising synthetic methods to produce superhydrophobic (SH) surfaces is the subject of intensive, ongoing, worldwide research.[10-32] SH properties such as self-cleaning, water exclusion, avoidance of corrosion, and promotion of slip suggest numerous applications from protective coatings, MEMS, and aerosol collection to new protective fabrics for military use.[33,34] The nature of the water/SH surface is crucial to the realization of these practical applications. Of particular interest is understanding how this solid-liquid-vapor interface controls phenomena such as rolling[35] instead of sliding of individual droplets and avoiding the nearly ubiquitous no-slip boundary condition.[36-41]

We have developed a simple, evaporation-driven procedure to deposit fractal SH coatings on arbitrary surfaces. It is derived from our earlier work on low-temperature/low-pressure aerogel coatings.[42] In this process, surface derivatization of silica sols with fluroalkyl groups[28] causes drying shrinkage to be reversible. Springback at the final stage of drying results in a hierarchical fractal surface decorated with hydrophobic ligands. The advantage of our approach relative to many others is that SH surfaces form by (evaporation-induced) reassembly from a very low viscosity sol under standard laboratory conditions. This makes our procedure amenable to coating small features and virtually any kind of substrate. Applied to plastic, glass, metal, and silicon substrates and textiles, our SH coatings are optically transparent with contact angles exceeding 155°. In addition, we have developed a lithographic technique enabling optical adjustment of the water contact angle from 170° to <10°.

SH fractal surfaces with surface fractal dimension of 2.2 – 2.3 have also been formed by freezing an alkylketene dimer wax[31,43] or by surface treatment of anodically oxidized alumina films with fluoroalkyl ligands,[32,44] whereas for our SH aerogel films a mass fractal dimension of 2.7 is measured using small-angle X-ray scattering.

Although scanning electron microscopy (SEM) and atomic force microscopy (AFM) have been used routinely to image SH surfaces in air, a noninvasive technique such as X-ray or neutron scattering is required to study the buried water – SH film interface. Neutrons are particularly useful for such a study because of their large

penetration depth, isotopic sensitivity, and ability to contrast match portions of the system. Neutron reflectivity (NR) has been used to study buried thin films and their interfaces;[45-47] it provides information about the scattering-length density, thickness, and interfacial roughness of different layers in a system.

Here, neutron reflectivity is used to understand the properties of SH films in contact with water. UV/ozone treatment is used to vary the water contact angle and understand the resulting effect on the SH film interaction with deuterated water (D_2O). Comparing AFM results, DFT simulations, and NR, we arrive at the location, width, and nature of the SH-water interface.

Experimental Methods

SH Film Preparation. The superhydrophobic coatings were made from a precursor solution containing mixed alkoxides 3,3,3-trifluoropropyl-trimethoxysilane (TFPTMOS) and tetramethyl orthosilicate (TMOS) using a variation of the aerogel thin film process reported by Prakash et al.[42] The filtered sol was further diluted with ethanol and other solvents to obtain a final film thickness of ~50 nm. Water contact angles consistently reached 155-160°, and angles up to 170° have been observed. The advancing and receding contact-angle hysteresis is typically 5°. The effect of various process parameters on the superhydrophobic behavior of the aerogel films is the topic of another communication.

To prevent the potential dissolution of underivatized silica in the aqueous subphase[48,49] during the long acquisition times of NR (approximately 4 h), the D_2O subphase used in this study was made acidic by adding D_2SO_4 so as to make the final acid concentration 0.01 N (approximately equivalent to pH 2). No treatment to remove dissolved gases from D_2O was performed. To investigate the SH-water interface further, contrast matching experiments were performed with an acidic water subphase composed of a mixture of H_2O and D_2O (referred to as HDO henceforth) in the v/v ratio of 17:4, resulting in a water subphase scattering-length density (SLD) of 0.75×10^{-6} Å^{-2}. Contrast matching techniques allow certain regions of the film to be enhanced or diminished with respect to neutron scattering. UV/ozone treatment was performed to photocalcine the organic ligands.[50,51] The time of exposure controlled the surface

occupancy of the CH_3 and CF_3 groups, thereby adjusting the apparent contact angle, θ^{α}, while maintaining constant porosity, Φ_s, and roughness.

AFM/SEM/TEM. Various microscopies were used to investigate the surface and bulk structure of the SH films. Scanning electron microscopy (SEM) was performed on a Hitachi S-800, equipped with a Gatan CCD (charged coupled device) camera at an operating voltage of 20 kV. Samples were coated with a thin gold film to prevent charging. Transmission electron microscopy (TEM) measurements were performed on a JEOL 2010 microscope to investigate the internal fractal structure of the aerogel film. Film fragments were scraped from the substrate and transferred onto a holey carbon grid for investigation. Atomic force microscopy (AFM) measurements were performed on a Digital Instruments Nanoscope IIIa SPM controller (noise < 0.3 Å rms in the vertical, i.e., *z*, dimension, with vibration isolation) in contact mode. A cantilever with a nominal spring constant of 0.1 N/m was used with minimum force (the tip was withdrawn stepwise and brought back stepwise to track the surface). The images are 512 pixels x 512 pixels in size; hence the scan size determined the resolution.

DFT Simulations. To investigate the contact region of a fluid and a rough substrate, we performed lattice modeling. On a 3D lattice, we constructed a wall with a regular array of square pyramids. The wall sites that make up the pyramids interact with the fluid via a short-ranged one-body external field whose strength is such that a smooth wall of these sites would have a contact angle somewhat larger than 90°. The fluid in question is a lattice gas model fluid with short-range attractions that reach to the next nearest neighbor sites. The temperature is about halfway between the triple and critical points, and together with the choice of overall density, this ensures that two-phase coexistence will be maintained. We used lattice density functional theory (DFT) in the canonical ensemble to minimize the total Helmholtz free energy and solve for the equilibrium density profile.[52,53] The initial configuration consisted of an isolated drop in the middle of the box. The drop can then be lowered, for instance, by applying a slight gravitational field. Ultimately, the drop enters the interaction range of the patterned wall, and the drop adjusts its shape to minimize the surface free energy.

Neutron Reflectivity. The reflectivity *R* of a surface is defined as the ratio of the number of particles (neutrons or photons) elastically and specularly scattered from the surface to the number of incident particles. When measured as a function of wave vector transfer, Q_z (defined below), the reflectivity curve contains information regarding the profile of the in-plane average of the coherent scattering cross sections normal to the substrate (silicon surface). If one knows the chemical constituents of the investigated system and the concentration of a given atomic species at a particular depth, *z*, then the scattering length density (SLD) distribution, $\beta(z)$, can be calculated from

$$\beta(z) = \frac{1}{v_m(z)} \sum_i^m b_i(z)$$

where b_i is the bound coherent scattering length of the *i*th of *m* atoms in the molecule with molecular volume v_m at location *z*. In the first Born approximation, the specular reflectivity, *R*, is related to the Fourier transform of the spatial derivative of the scattering-length density profile, $d\beta/dz$, by

$$R(Q_Z) = R_F(Q_z)\left|\frac{1}{\beta_s}\int_{-\infty}^{+\infty}\frac{d\beta(z)}{dz}\exp(-iQ_z z)dz\right|^2$$

where R_F is the Fresnel reflectivity of the substrate and β_s is the substrate scattering-length density. Neutron reflectivity measurements were performed on the SPEAR beamline, a time-of-flight reflectometer, at the Manuel Lujan Neutron Scattering Center, Los Alamos National Laboratory (http://lansce.lanl.gov/ lujan/index_lujan.htm). The neutron beam is produced by the spallation of neutrons from a tungsten target using a pulsed beam (20 Hz) of 800 MeV protons. A partially coupled liquid hydrogen moderator at 20 K modifies the neutron energy spectrum. Neutrons with wavelengths of λ=2-16 Å are selected by means of choppers and frame-overlap mirrors (http://www.lansce.lanl.gov/lujan/ER1ER2/SPEAR/index.html). The scalar value of momentum transfer vector Q_z is determined from Q_z) $4\pi \sin(\alpha)/\lambda$ (where α is the angle of incidence measured from the sample surface and λ is the wavelength of the probe), and its range is covered by performing measurements at two angles of incidence, typically 0.5 and 2.5°. The beam footprint was 8 mm x 60 mm. The background limits

the Q_z range over which reflectivity data can be collected; scattering from the subphase makes a significant contribution to the background. Hence, we designed a cell made of Maycor (Ceramic Products Inc, Palisades Park, NJ, containing SiO2/MgO/Al2O3/K2O/B2O3/F in the weight ratio 46:17:16:10:7:4) to minimize the incoherent scattering from the cell, and the O-ring groove was machined to achieve a subphase reservoir depth of about 50 μm (Figure 1). The reflectivity data is normalized by the Fresnel reflectivity of the substrate, R_F, and plotted versus Q_z to compensate for the sharp decrease in the reflectivity[54] as described by Fresnel's law: $R \alpha Q_z^{-4}$.

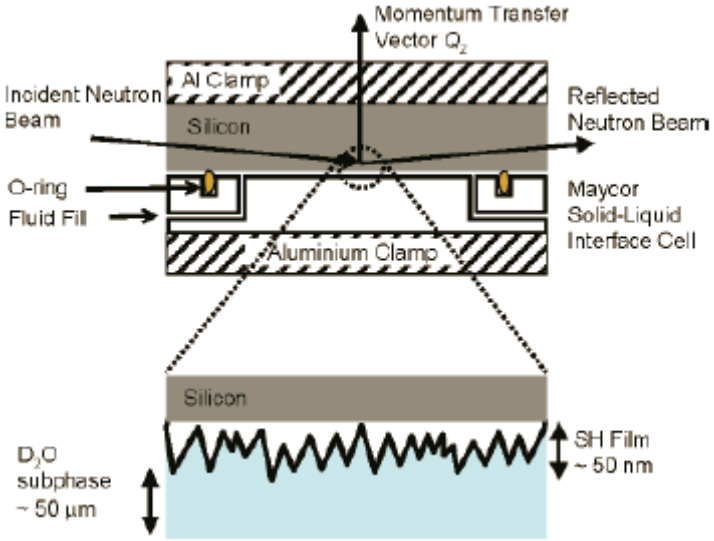

Figure 1. Schematic of the setup used for neutron reflectivity measurements

The intensity of the specular reflectivity and the real-space SLD are related by a transformation. Because phase information is lost when collecting the specular reflectivity, as in most scattering experiments, and because of the nonlinear nature of the inverse transformation, a unique solution to the problem cannot be obtained analytically. The reflectivity data were analyzed by a model-dependent Parratt formalism[55] that requires a priori knowledge of the composition of the sample (SLD profile). Here our philosophy was to use the simplest possible model of physical relevance. In this model, the scattering-length density distribution $\beta(z)$ is described by a sequence of n slabs, each of constant scattering-length density. Two adjoining layers i and $i + 1$ are connected by β_{int}, a sigmoidal function profile that describes the interfacial (chemical) roughness given by

$$\beta_{\text{int}}(z) \propto erf\left(\frac{z - z_{mid}}{\sigma}\right)$$

The error function is symmetric around z_{mid}, and so is the resulting interface profile. This is used as a convenient, well accepted model. We recognize that

interfaces may not be symmetric, but because of the lack of a priori information from other experiments and theory, we are limited to the use of symmetric profiles to reduce the number of parameters in the fit and arrive at the simplest possible model.

Results and Discussion

Surface Characterization. Superhydrophobic (SH) films were spin coated onto 10-cm-diameter, 6-mm-thick silicon substrates. Spectroscopic ellipsometry measurements indicate a film thickness of 440 Å and a refractive index of n_f = 1.1188. Assuming an all-silica skeleton (Xray photon spectroscopy measurements indicate low amounts of organics (C, H, F)), the *z*-averaged film porosity can be determined from the Lorenz-Lorentz relationship[49]

$$\frac{n_f^2 - 1}{n_f^2 + 1} = (1 - \phi)\frac{n_s^2 - 1}{n_s^2 + 2}$$

where n_s is the refractive index of the solid skeleton and Φ is the film porosity. Using the above equation and n_s = 1.458, we obtain a porosity value of Φ = 0.72. (This value

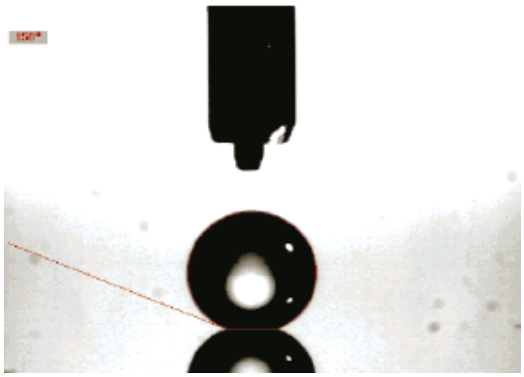

Figure 2. Representative image of a sessile drop measurement of the water angle on a superhydrophobic aerogel film showing a contact angle of 158±2º.

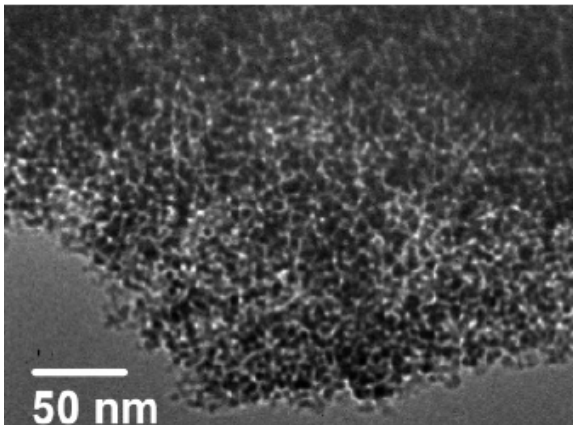

Figure 4. Transmission electron micrograph of the SH aerogel film. The darker regions correspond to silica, whereas the lighter regions represent the porous network.

represents a lower bound for the porosity due to the presence of C, F, and H.) Sessile drop contact-angle measurements on SH films indicate an apparent water contact angle of 158 ± 2° (Figure 2).

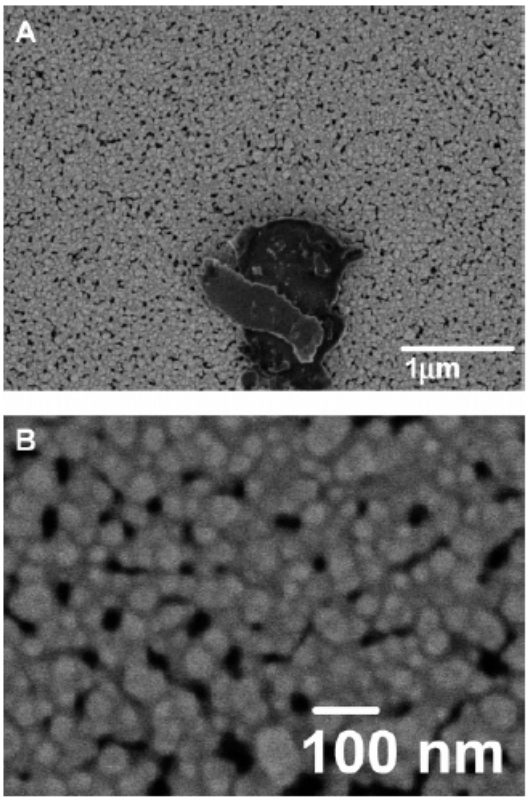

Figure 3. Scanning electron micrographs of the SH film. (A) Top view of the SH film. The dust particle at the bottom center is used as a focusing aid. (B) Higher magnification image of the same film. The slight rounding of the features is due to the gold coating. The lighter regions correspond to silica, whereas the dark regions represent pores in the network.

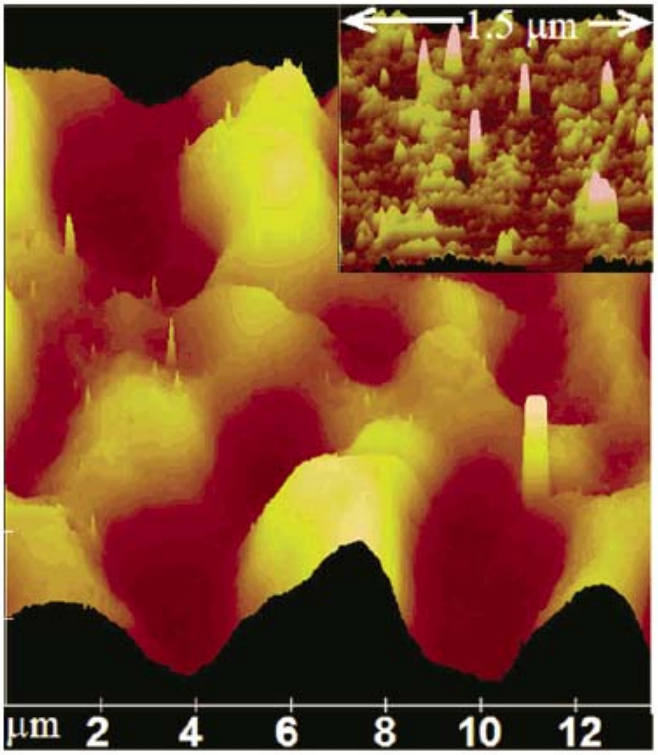

Figure 5. AFM image of SH film in air measured over an area of 13.5 μm x 13.5 μm. The inset shows another image at a higher magnification measured over an area of 1.5 μm x 1.5 μm.

Panels A and B of Figure 3 show SEM micrographs of the film surface. The lighter regions correspond to silica, whereas the dark regions represent pores in the network. The globular morphology typical of a base-catalyzed silica gel is seen. The broad distribution of globular building blocks that results in the rough surface and imparts to the film its superhydrophobic character is evident from these images. The TEM image in Figure 4 shows the porous nature of the film. The darker regions correspond to silica, whereas the lighter regions represent the porous network. This open-cell structure exhibits fractal porosity with a wide pore-size distribution ranging from 1 to 500 nm.[56] Figure 5 shows a contact-mode AFM image of

the rough SH film in air. The calculated rms roughness, measured over the area 13.5 μm x 13.5 μm, is σ_{AFM} = 123 Å. The inset in Figure 5 shows a higher-resolution AFM image with a 1.5 μm x 1.5 μm scan size. The inset shows the presence of roughness at various length scales, and the calculated rms roughness is 11 Å. Because the coherence of the incident neutron beam in the neutron reflectivity measurements is approximately 10 μm, for a comparison of roughness with neutron reflectivity data the larger scan size image in Figure 5 is relevant.

Neutron Reflectivity. Figure 6A shows the normalized reflectivity data for SH aerogel films in contact with two different aqueous environments. The use of 100% D_2O and a H_2O/D_2O mixture (referred to as HDO) allows us to study the system using two different scattering contrasts. The corresponding SLD profiles are shown in Figure 6B. It is evident from the SLD profile, especially in the case of a 100% D_2O subphase, that the porous SH film experiences minimal water penetration into the film bulk. Assuming no water penetration and a pure silica matrix with an SLD value of 3.47x 10^{-6} $Å^{-2}$ (neglecting the contribution from theCH_3 andCF_3 groups), we find that an SLD value of (0.353 ± 0.12) x 10^{-6} $Å^{-2}$ for the SH film (see region 20 Å < *z* < 200 Å in Figure 6B) corresponds to a porosity of {(1 - (0.353/3.47)} x 100 = 90 ± 3%, which is consistent with nitrogen adsorption measurements.[42,56] The film thickness obtained from the fit, *t* = 425 ± 6 Å, is consistent with ellipsometry data. The fitted value of the roughness of the SH film-water interface

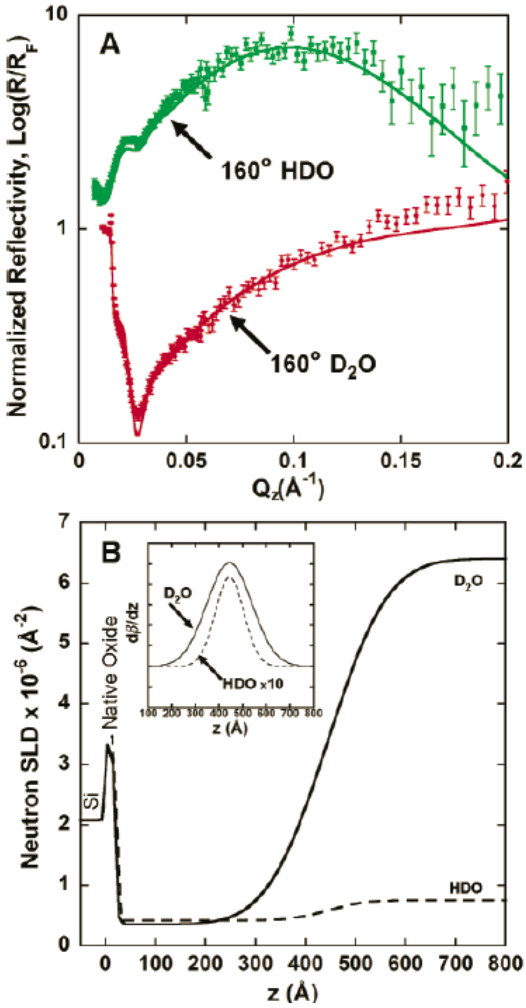

Figure 6. (A) Fresnel normalized reflectivity data and fit for a SH film with a water contact area of 160° in contact with 100% D_2O-H_2O mixture (labeled HDO). (B) Corresponding SLD profile for the fits in A. (Insert in B) Derivative of the SLD profiles in B, showing the location and the width of SH film – water interface.

using an error function profile, erf{(z - z_{mid})/σ}, is $\sigma_{SH\text{-}D2O}$ = 95 ± 3 Å. This value is comparable to the rms roughness determined from AFM experiments.

As mentioned earlier, studying the same system against a different subphase contrast provides additional information about the system and also corroborates the values of the fit parameters. For the SH film measured against a H_2O/D_2O mixture (HDO), the SLD of the bulk SH film described by the region with uniform SLD (20 Å < z < 200 Å in Figure 6B) is comparable to the case when the subphase is 100% D_2O. The fitted thickness of the SH film, 422 ± 10 Å, is again similar to the previous case. The inset in Figure 6B shows the derivative of the SLD profile, dβ/dz, where the lower full width of the Gaussian (the derivative of an error function is a Gaussian) in the case of the HDO indicates a smaller interfacial roughness of $\sigma_{SH\text{-}HDO}$ = 60 ± 4 Å. This apparent reduction in roughness can be attributed to the lower SLD contrast between the SH film and bulk water, where certain valleys in the surface topography that may be filled with the water subphase cannot be discerned from the bulk water or the bulk film. The difference in the SLD as one approaches bulk water can be written as

$$\Delta\beta = \beta_{film}\varepsilon_{film} + \beta_{water}(1-\varepsilon_{film}) - \beta_{water} = (\beta_{film} - \beta_{water})\varepsilon_{film}$$

where ε_{film} is the areal fraction occupied by the film at a particular z value, β_{film} = 0.35 x 10^{-6} Å^{-2}, β_{D2O} ≈ 6.3 x 10^{-6} Å^{-2}, and $\beta_{H2O/D2O}$ = 0.75 x 10^{-6} Å^{-2}. Given a constant $\Delta\beta$ resolving ability of NR, the apparent bulk water will be detected at a lower ε_{film} value for the mixed H_2O/D_2O subphase, which corresponds to a smaller z value. A reduction of approximately 100 Å in the z location of bulk water (seen clearly by the tail of the Gaussian peak in the dβ/dz profile in the Figure 6B inset) for the mixed H_2O/D_2O subphase suggests that water penetrates to a depth of at least 100 Å from the thickest location of the SH film.

The neutron reflectivity (NR) data also helps us eliminate certain possibilities that one might envisage for the nature of the water-film interface. We have considered alternative scenarios; one probable one is where a flat, smooth water surface spans the peaks of the surface roughness without entering the valleys. A model constrained to include a rough film surface but with a smooth water surface cannot fit the NR data. This information along with the fact that different subphase contrast experiments (D_2O

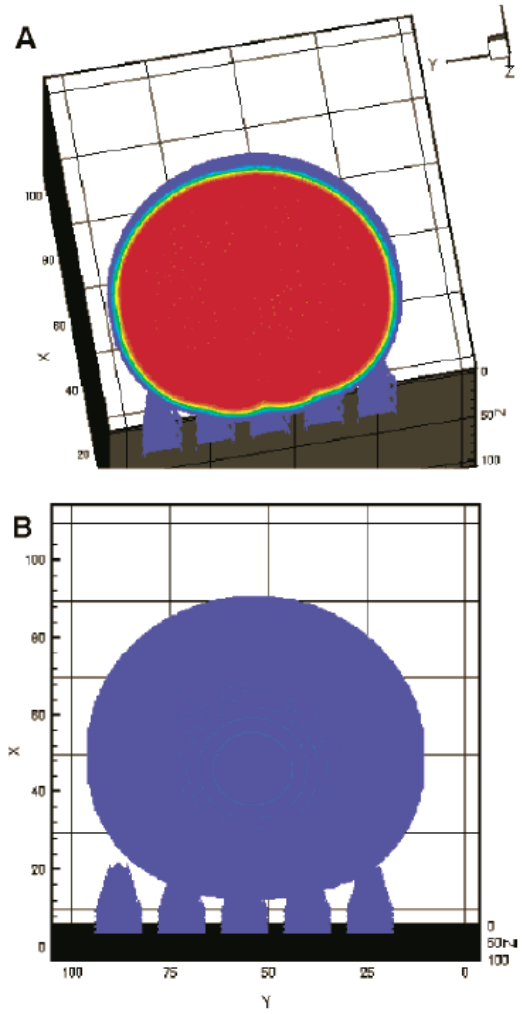

Figure 7. DFT simulation of a 40nm water droplet on a rough surface: (A) a top-angled view and (B) a side cross-sectional view

and HDO subphase) show different roughness suggests that the real situation is akin to an Indian fakir on a bed of nails with his skin sagging between the nails.

The proposed situation is described by the DFT simulations in Figure 7, where we display the final 3D contour level density profile of the drop as it has come to rest on the pyramids. The results demonstrate that

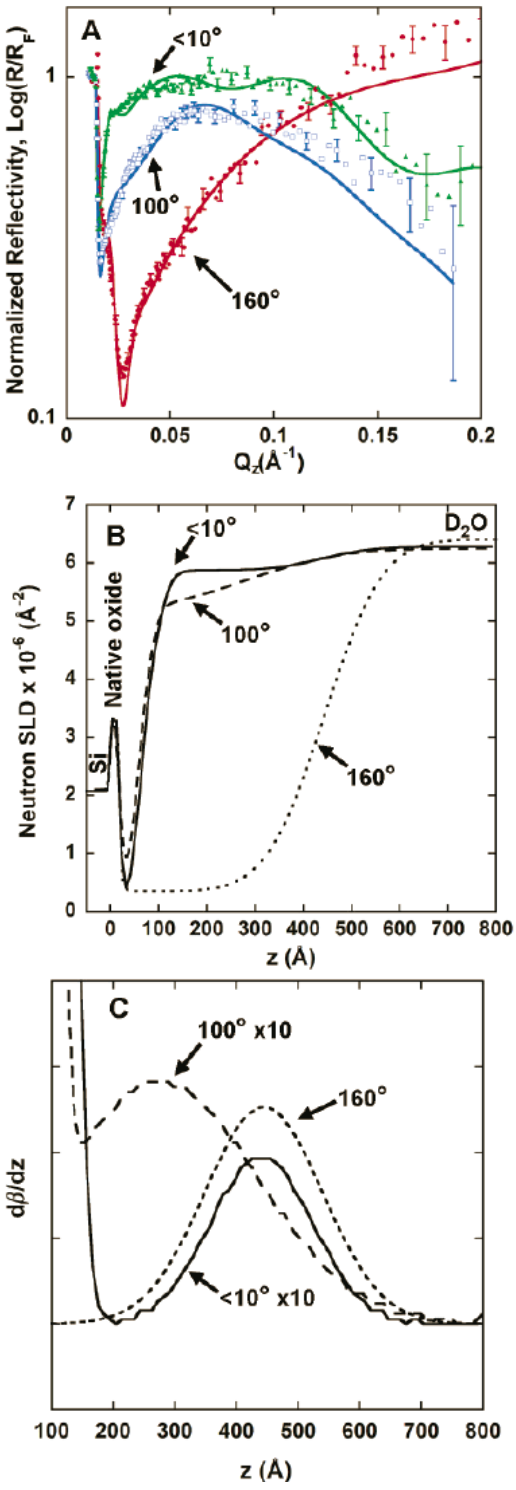

Figure 8. (A) Fresnel normalized reflectivity data and fit for films with different contact angles in contact with D_2O. (B) Corresponding SLD profile for the fits in A. (C) Derivative of the SLD profiles in B, showing the location and width of interfaces in the system.

whereas the local contact angle (where fluid and pyramids meet locally) is indeed slightly larger than 90° the overall effective contact angle is close to 180°. The limited contact points between the liquid droplet and the solid surface as seen from Figure 7B may aid the rolling motion of the droplet as seen for the lotus leaf, as opposed to sliding.

Figure 8A shows normalized neutron reflectivity data and fits for aerogel films with water contact angles of < 10, 100, or 160° in contact with D_2O. The corresponding SLD profile derived from box model fits is shown in Figure 8B. It is evident from the SLD profiles that the superhydrophobic film with a contact angle of 160° shows minimal water infiltration, as evident by the low SLD values next to the silicon substrate (same data as in Figure 6).

In the case of a film subjected to 30 min of photocalcination to remove the hydrophobic groups and render it hydrophilic (water contact angle of <10°) but maintain its surface topography (roughness), we do observe D2O infiltration into the porous aerogel matrix. The SLD of the D_2O filled film (region 100 Å < z < 220 Å in Figure 8B) is (5.87 ± 0.04) x 10^{-6} $Å_{-2}$, and that of the bulk D_2O subphase (z > 600 Å) is 6.27 x 10^{-6} $Å^{-2}$. These values indicate a D_2O volume occupancy of (5.87 - 0.353)/6.27 x 100 = 87 ± 3% in the aerogel film, which, considering complete infiltration into open pores, is consistent with the earlier deduced porosity of 90 ± 3%. The small difference can be attributed to 3.3% closed and/or inaccessible pores. Furthermore, the location of the average film-D_2O interface, marked by the inflection point in the SLD profile or, alternatively and more clearly, the position of the Gaussian peak (Figure 8C) in the derivative of the SLD profile is preserved for both the <10 and 160° contact angle samples. The fitted roughness value is $\sigma_{10deg\text{-}D2O}$ = 86 ± 20 Å.

For an SH film subjected to partial photocalcination such that its surface exhibits a water contact angle of 100°, we observe behavior that is intermediate between that of the 160º and <10° contact-angle samples. From the normalized reflectivity curve in Figure 8A, we see that the intensity increases toward unity with decreasing contact angle. That is, the difference between the sample reflectivity, R, and the Fresnel reflectivity, R_F, decreases, indicating a reduction in the contrast between the bulk and the porous film (due to filling of the pores with D_2O). The SLD profile for the 100° film indicates the existence of a continuous gradient from bulk D_2O into the film. This

gradient can be attributed to the distribution of pockets of pores that are not filled by water. Pores with a surface contact angle greater than 90° should not get filled with water. Because the film surface contact angle is amplified by its roughness,[5,8] the corresponding contact angle for identical surface chemistry that exists within the pores may be less than 90°. This allows water to infiltrate pores of size greater than a certain critical size, resulting in a distribution of water-filled and empty (air-filled) pores. This distribution results in a chemical roughness (roughness in SLD) to which the neutrons are sensitive. The peak in the SLD derivative profile seen around 300 Å (Figure 8C) does not imply that the average film thickness has been reduced to 300 Å. Instead, it is a manifestation of the chemical roughness. There is consistency in the three contact-angle films studied regarding the *z* location of bulk D_2O that is found at about 600 Å.

A feature that is common to the <10 and 100° contact angle films and might also be present in the 160° contact angle film is the presence of a buried layer of 33-37 Å thickness at the substrate film interface (20 Å < *z* < 60 Å) that exhibits almost no D_2O penetration. Its presence and length scale can also be seen from the normalized reflectivity curves that show a broad but definite envelope with an approximate width of $\Delta Q_z = 2\pi/37 = 0.16$ Å^{-1}, a feature that is clearly absent in the 160° SH film data. The presence of this layer can be explained by either (i) trapped and stabilized gas bubble pockets during cell filling or (ii) a different film morphology that forms during the coating or the photocalcination process next to the solid substrate compared to the bulk and gives rise to a more closed-cell structure preventing water penetration.

Figure 9 shows the normalized neutron reflectivity and SLD profiles for films with contact angles of 160 and 100° exposed to a saturated D_2O vapor environment. The lack of scattering contrast between the SH film (160°) and the D2Ovapor, coupled with a high surface roughness, results in an almost featureless reflectivity curve. Hence, the SH film thickness and interfacial roughness parameter σ were fixed, on the basis of values obtained previously against a D_2O subphase, at 425 and 95 Å, respectively. A bulk film SLD of 0.62×10^{-6} Å^{-2} was obtained. The increase in the SLD value from that of 90% porous silica may be due to D_2O condensation into defects and/or the constrained fit. However, this provides a baseline to compare qualitatively with a film prepared with a surface water contact angle of 100° shown in Figure 9. The reflectivity

curve for the 100° film shows a clear oscillation in the Q_z range of 0.01 - 0.03Å^{-1}. This oscillation most likely arises from a layer of higher SLD contrast and/or greater smoothness. The SLD profile for this film shows evidence of water condensation into the pores of the film. The region 120 Å < z < 300 Å in Figure 9B exhibits an SLD of (0.94 ± 0.05) x 10^{-6} Å^{-2} indicating approximately 10% of the pore space to be filled with condensed D_2O. A smoother interface is also seen as a narrower peak width in the derivative profile in the inset of Figure 9B. This maybe attributed to a skin of water-filled pores forming at the film surface reducing the effective chemical (SLD) roughness seen by neutrons.

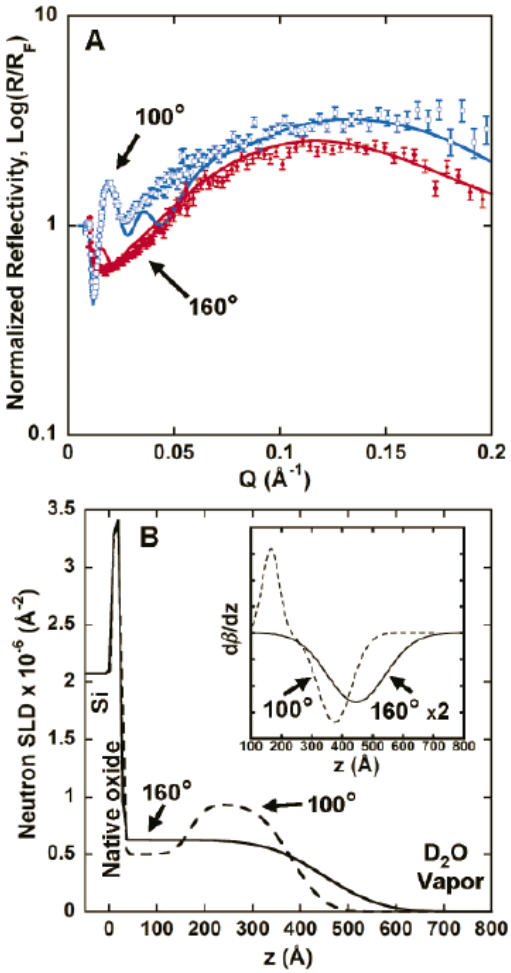

Figure 9. (A) Fresnel normalized reflectivity data and fit for films with different contact angles in contact with D_2O vapor. (B) Corresponding SLD profile for the fits in the A. (Insert in B) Derivative of the SLD profiles in B, showing the location and width of interfaces in the system.

Conclusions

NR combined with additional structural analyses and molecular simulations has established the nature of rough silica surfaces submerged in water or exposed to 100% RH. For SH surfaces characterized by water contact angles of ~160°, water penetrates to a depth of about 100 Å, which is on the order of the surface roughness probed by AFM. At this level of penetration, the interface comprises about 5% solid, and the interface is defined by the topology of the pinned solid/liquid/vapor contact points. Using 5% solid and 91° for θ, we derive an apparent contact angle, θ^{α}, of 154° from the Cassie-Baxter relationship. The complete removal of hydrophobic ligands via photocalcination (θ < 10°), while preserving the roughness, should yield θ^{α} > 130° according to the Cassie-Baxter relationship. However, this is not observed, which suggests that we are in the Wenzel regime. The inherent presence of air in the porous aerogel films may be a

contributing factor to the validity of the Cassie-Baxter regime, but when the hydrophobic ligands are removed, the Wenzel regime is thermodynamically favorable. This mix of trapped air and surface roughness makes these films an interesting system to study from a theoretical viewpoint. Observing such a high water contact angle for a film of <500 Å thickness is remarkable when compared to the micrometer-scale roughness developed in most synthetic SH surfaces and found in nature.[2,3] Photocalcination procedures allow a change in surface chemistry with minimal effect on surface topography. A systematic trend of increased water infiltration with decreasing surface coverage of the hydrophobic ligands is observed. Surprisingly, a ~35 Å buried layer with low scattering-length density is observed in photocalcined films. Its origin is not well understood and will be the subject of future investigations.

(1) Barthlott, W.; Neinhuis, C. *Planta (Heidelberg)* **1997**, *202*, 1.
(2) Neinhuis, C.; Barthlott, W. *Ann. Bot. (London)* **1997**, *79*, 667.
(3) Koch, K.; Neinhuis, C.; Ensikat, H. J.; Barthlott, W. *J. Exp. Bot.* **2004**, *55*, 711.
(4) Cassie, A. B. D. *Discuss. Faraday Soc.* **1948**, *3*, 11.
(5) Cassie, A. B. D.; Baxter, S. *Trans. Faraday Soc.* **1944**, *40*, 546.
(6) He, B.; Patankar, N. A.; Lee, J. *Langmuir* **2003**, *19*, 4999.
(7) Herminghaus, S. *Europhys. Lett.* **2000**, *52*, 165.
(8) Wenzel, R. N. *Ind. Eng. Chem.* **1936**, *28*, 988.
(9) Bico, J.; Marzolin, C.; Quere, D. *Europhys. Lett.* **1999**, *47*, 220.
(10) Chen, A. C.; Peng, X. S.; Koczkur, K.; Miller, B. *Chem. Commun.* **2004**, 1964.
(11) Favia, P.; Cicala, G.; Milella, A.; Palumbo, F.; Rossini, R.; d'Agostino, R. *Surf. Coat. Technol.* **2003**, *169/170*, 609.
(12) Feng, L.; Li, S. H.; Li, Y. S.; Li, H. J.; Zhang, L. J.; Zhai, J.; Song, Y. L.; Liu, B. Q.; Jiang, L.; Zhu, D. B. *Adv. Mater.* **2002**, *14*, 1857.
(13) Flemming, M.; Hultaker, A.; Reihs, K.; Duparre, A. *Proc. Soc. Photo-Opt. Instrum. Eng.* **2003**, *5250*, 56.
(14) Khorasani, M. T.; Mirzadeh, H.; Sammes, P. G. *Radiat. Phys. Chem.* **1996**, *47*, 881.
(15) Klein, R. J.; Biesheuvel, R. M.; Yu, B. C.; Meinhart, C. D.; Lange, F. F. *Z. Metallkd.* **2003**, *94*, 377.
(16) Nakajima, A.; Abe, K.; Hashimoto, K.; Watanabe, T. *Thin Solid Films* **2000**, *376*, 140.
(17) Ren, S. L.; Yang, S. R.; Zhao, Y. *Acta Mech. Sinica* **2004**, *20*, 159.
(18) Sasaki, M.; Kieda, N.; Katayama, K.; Takeda, K.; Nakajima, A. *J. Mater. Sci.* **2004**, *39*, 3717.
(19) Shirtcliffe, N. J.; Sanaa, A.; Evans, C.; McHale, G.; Newton, M. I.; Perry, C. C.; Roach, P. *J. Micromech. Microeng.* **2004**, *14*, 1384.
(20) Teare, D. O. H.; Spanos, C. G.; Ridley, P.; Kinmond, E. J.; Roucoules, V.; Badyal, J. P. S.; Brewer, S. A.; Coulson, S.; Willis, C. *Chem. Mater.* **2002**, *14*, 4566.

(21) Woodward, I.; Schofield, W. C. E.; Roucoules, V.; Badyal, J. P. S. *Langmuir* **2003**, *19*, 3432.
(22) Feng, L.; Li, S. H.; Li, H. J.; Zhai, J.; Song, Y. L.; Jiang, L.; Zhu, D. B. *Angew. Chem., Int. Ed.* **2002**, *41*, 1221.
(23) Zhang, X.; Shi, F.; Yu, X.; Liu, H.; Fu, Y.; Wang, Z. Q.; Jiang, L.; Li, X. Y. *J. Am. Chem. Soc.* **2004**, *126*), 3064.
(24) Shin, J. Y.; Kuo, C. W.; Chen, P. L.; Mon, C. Y. *Mater. Res. Soc. Symp. Proc.* **2004**, *823*, 181.
(25) Shirtcliffe, N. J.; McHale, G.; Newton, M. I.; Chabrol, G.; Perry, C. C. *Adv. Mater.* **2004**, *16*, 1929.
(26) Kijlstra, J.; Reihs, K.; Klamt, A. *Colloids Surf., A* **2002**, *206*, 521.
(27) Brevnov, D. A.; Barela, M. J.; Brooks, M. J.; Lopez, G. P.; Atanassov, P. B. *J. Electrochem. Soc.* **2004**, *151*, B484.
(28) Roig, A.; Molins, E.; Rodriguez, E.; Martinez, S.; Moreno-Manas, M.; Vallribera, A. *Chem. Commun.* **2004**, 2316.
(29) Shang, H. M.; Wang, Y.; Limmer, S. J.; Chou, T. P.; Takahashi, K.; Cao, G. Z. *Thin Solid Films* **2005**, *472*, 37.
(30) Rao, A. V.; Kulkarni, M. M.; Amalnerkar, D. P.; Seth, T. *J. Non-Cryst. Solids* **2003**, *330*, 187.
(31) Onda, T.; Shibuichi, S.; Satoh, N.; Tsujii, K. *Langmuir* **1996**, *12*, 2125.
(32) Shibuichi, S.; Yamamoto, T.; Onda, T.; Tsujii, K. *J. Colloid Interface Sci.* **1998**, *208*, 287.
(33) Inoue, Y. *J. Jpn Soc. Tribol.* **2002**, *47*, 353.
(34) Blossey, R. *Nat. Mater.* **2003**, *2*, 301.
(35) Richard, D.; Quere, D. *Europhys. Lett.* **1999**, *48*, 286.
(36) Barrat, J. L.; Bocquet, L. *Phys. Rev. Lett.* **1999**, *82*, 4671.
(37) Baudry, J.; Charlaix, E.; Tonck, A.; Mazuyer, D. *Langmuir* **2001**, *17*, 5232.
(38) Tretheway, D. C.; Meinhart, C. D. *Phys. Fluids* **2002**, *14*, L9.
(39) Zhu, Y. X.; Granick, S. *Phys. Rev. Lett.* **2002**, *88*, 106102.
(40) Granick, S.; Zhu, Y. X.; Lee, H. *Nat. Mater.* **2003**, *2*, 221.
(41) Ou, J.; Perot, B.; Rothstein, J. P. *Phys. Fluids* **2004**, *16*, 4635.
(42) Prakash, S. S.; Brinker, C. J.; Hurd, A. J.; Rao, S. M. *Nature* **1995**, *374*, 439.
(43) Shibuichi, S.; Onda, T.; Satoh, N.; Tsujii, K. *J. Phys. Chem.* **1996**, *100*, 19512.
(44) Tsujii, K.; Yamamoto, T.; Onda, T.; Shibuichi, S. *Angew. Chem.,Int. Ed. Engl.* **1997**, *36*, 1011.
(45) Fragneto-Cusani, G. *J. Phys.: Condens. Matter* **2001**, *13*, 4973.
(46) Krueger, S. *Curr. Opin. Colloid Interface Sci.* **2001**, *6*, 111.
(47) Wu, W. L.; Orts, W. J.; Majkrzak, C. J.; Hunston, D. L. *Poly. Eng. Sci.* **1995**, *35*, 1000.
(48) Iler, R. K. *The Chemistry of Silica*; Wiley: New York, 1979¢¢.
(49) Brinker, C. J.; Scherer, G. W. *Sol-Gel Science: The Physics and Chemistry of Sol-Gel Processing*; Academic Press: San Diego, CA, 1990.
(50) Clark, T.; Ruiz, J. D.; Fan, H. Y.; Brinker, C. J.; Swanson, B. I.; Parikh, A. N. *Chem. Mater.* **2000**, *12*, 3879.
(51) Dattelbaum, A. M.;Amweg,M.L.; Ruiz, J. D.; Ecke, L. E.; Shreve, A. P.; Parikh, A. N. *Mater. Res. Soc. Symp. Proc.* **2003**, *788*, 371.

(52) VanSwol, F.; Malanoski, A. P. *Phys. Rev. E: Stat. Phys., Plasmas, Fluids, Relat. Interdiscip. Top.* **2002**, *66*, 041603/1.
(53) VanSwol, F.; Malanoski, A. P. *Phys. Rev. E: Stat. Phys., Plasmas, Fluids, Relat. Interdiscip. Top.* **2002**, *66*, 041602/1.
(54) Als-Nielsen, J. *Physica A* **1986**, *140*, 376.
(55) Parratt, L. *Phys. Rev.* **1954**, *95*, 359.
(56) Prakash, S. S.; Brinker, C. J.; Hurd, A. J. *J. Non-Cryst. Solids* **1995**, *190*, 264.

Chapter 3. Effective slip on textured super-hydrophobic surfaces

An interface between a viscous fluid and a solid surface is usually characterized by a no-slip boundary condition, although the notion of possible slip on the boundary was introduced almost 200 years ago.[1] Slip on the boundary can occur on the scale on the order of tens of nanometers,[2–4] but the effects of this phenomenon are not appreciable for macroscopic flows. In countless applications, a limited slip boundary condition would be highly desirable. The motivations include, but are not limited to, drag and pressure drop reduction. Recent advances in materials science have led to creation of superhydrophobic (SH) surfaces with unusual contact properties and motivated new research on the boundary conditions near the latter,[5] although apparently there is no macroscopic slip near SH surfaces produced by application of SH coating to a smooth substrate.

The defining property of SH surfaces is a very high contact angle u, measured as the angle between the plane of the surface and the tangent to the surface of a droplet resting on it: θ >140° [Fig. 1a]. We show that in fluid flow near a textured SH surface (e.g., a drop moving down an incline), due to this high θ, the contact area between the fluid and the surface is reduced, producing effective macroscopic slip on scales consistent with the characteristic size of the surface features.

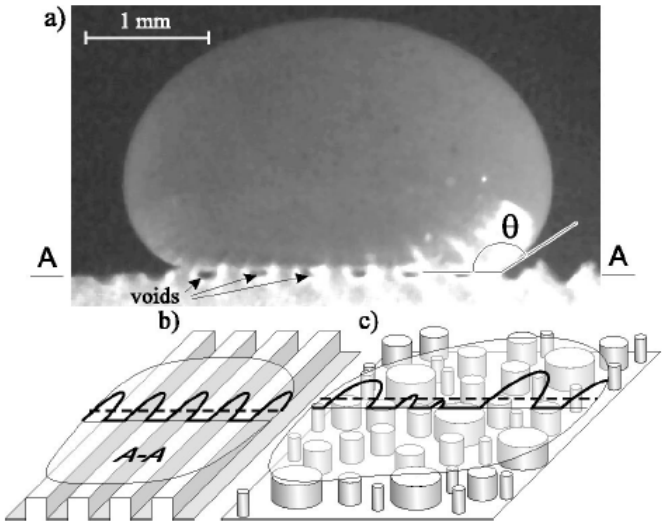

Figure 1. Schematics of fluid behavior near a SHsurface: (a) side view of a droplet on regularly grooved surface with voids (no-contact areas) and contact angle θ shown, *A-A* indicates the location of the plane of the nominal fluid boundary, (b) perspective view of the grooved surface showing fluid velocity profile in the *A-A* plane with the dashed line indicating average (i.e., slip) velocity, (c) perspective view of an idealized irregularly textured surface showing the fluid velocity profile and effective slip velocity at the fluid boundary.

Our basic notion of the flow behavior near a textured SH surface is illustrated in Fig. 1. The

characteristic size of the texture is much larger than any surface roughness associated with the SH coating itself, but smaller than the capillary length (2.7 mm for water). The texture can be regular (e.g., grooves) or irregular (random peaks). The direct contact area between the surface and the fluid is limited to the protruding parts of the surface (lands for the regular texture, peaks for the irregular texture), with free fluid surface areas above the depressed parts (grooves for the regular texture, valleys for the irregular texture). We assume that these areas exist because there is insufficient energy to deform the fluid boundary to bring it in contact with all the surface [Fig. 1a]. This will lead to a velocity profile in the plane of the lands with zero velocity in the contact area and nearly parabolic velocity distribution in the grooves. A velocity average at the nominal fluid boundary (the plane of the lands) would be greater than zero [Fig. 1b]. Similar behavior can be expected for an irregular texture [Fig. 1c], although the shape of the real-life boundary of the fluid in the latter case is likely more complicated.

For a flow inside a round pipe with alternating slip/noslip boundary condition, an analytical solution manifests nontrivial effective slip velocity.[6] For a fixed ratio between the widths of the lands and the grooves, this solution predicts effective slip to increase linearly with the land width. To visualize a plausible velocity distribution near a surface in partial contact with fluid, we conducted a simple finite-element numerical simulation of a Poiseuille flow in a circular cross-section tube with alternating boundary conditions (Fig. 2) for a 1:1 ratio between the widths of the lands (no slip) and the grooves (slip). The simulation shows effective slip increasing with the land width linearly in good agreement with the analytical results.[6] Thus one should expect macroscopic effective slip velocity to emerge on the boundary as the no-contact areas reach macroscopic size (for water, at least microns).

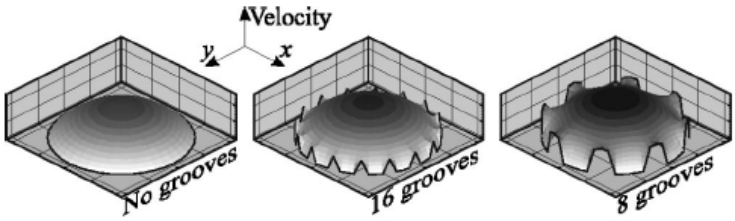

Figure 2. Velocity distributions obtained by numerical simulation of Poiseuille flow in a circular channel with alternating no-slip and free-surface boundary conditions. Left, uniform no-slip boundary; center, a pattern of 16 lands and 16 grooves of equal width; right, similar pattern with 8 pairs of lands and grooves. Note the increase in maximum flow velocity with groove size.

In real life, the fluid boundary is not perfectly flat, and the patterns shown in Fig. 1 can only be sustained for feature sizes below a certain limit dictated by the capillary length. Moreover, surface deformation in areas above the protruding features (grooves, peaks) is likely to contribute to the overall energy balance of the flow above the surface. Thus one could expect some optimal size for the surface features that maximizes effective slip. An earlier investigation of textured SH surfaces[7] indicates that the pattern of the texture influences the water-repelling properties of the surface, with regular grooved design being optimal for surface drag reduction and maximization of effective slip, as confirmed recently.[8] With these considerations taken into account, we conducted two simple experiments to benchmark the properties of smooth and textured SH surfaces.

In the first experiment, drops move down an inclined surface. The angle of the incline attached to a self-leveling support is measured with a high accuracy (up to 0.5 arc min). 20 cm long samples of materials are placed on the incline. At the elevated end of the sample, a syringe pump dispenses 1.5 mm radius drops. The working fluid is water or a mixture of water and zinc chloride, with a range of densities ρ from 1 g/cc to 1.9 g/cc and a corresponding range of kinematic viscosities from 10^{-6} m/s^2 to 10^{-5} m/s^2, the former values corresponding to pure water and the latter to a solution with a 2:1 $ZnCl_2$:water mass ratio. The characteristic Bond number for a water droplet of radius R=1.5 mm produced in this arrangement is $Bo = \rho g R^2 / \sigma = 0.30$, where σ =0.0728 N/m is the surface tension coefficient of water. For a same-size drop of the 2:1 zinc chloride solution, the Bond number is 0.15. Based on the rms velocity of a rolling solid sphere averaged over the extent of the slide for a 2° tilt angle, we estimate the characteristic velocity to be U_r=9.7 cm/s. Thus the capillary number for a water droplet is $Ca = \upsilon \rho U_r / \sigma = 10^{-13}$. The small value of the capillary number indicates that the shape of the droplet is not significantly affected by the motion.[9] The parameters of our experiment are somewhat consistent with the Bo « 1 (i.e., surface tension effects dominate gravity effects), Ca « 1 assumptions of the theory describing the motion of nonwetting rolling droplets.[9] Our droplet diameter is slightly larger than the capillary length though, so it would be unrealistic to expect good agreement with this theory. For a rolling droplet, the advancing and receding contact angles are not equal. Hysteresis

between them for the rolling droplet would be an interesting subject for future study. Reduction of the difference between the advancing and receding angles was reported to make it easier for the droplet to start rolling.[10] The drag reduction due to the emergence of noncontact areas described here, however, should not be directly influenced by the contact angle hysteresis.

The second experiment is a study of water flow near a Joukovsky hydrofoil with chord length L=4.3 cm, span 3.2 cm, and thickness 25% of the chord. The hydrofoil is installed in a water tunnel at a zero angle-of-attack and attached to a force transducer measuring the drag force. The flow speed U_∞ can be varied to produce a range of Reynolds numbers $\mathrm{Re} = U_\infty L / \upsilon$ from 1,500 to 11,000.

SH coating was prepared by a variation of the low temperature/pressure aerogel thin film process[11] wherein tetraethylorthosilicate was replaced with a 1.0:0.3 molar ratio of tetramethylorthosilicate:trifluoropropyltrime-thoxysilane. Drying results in a fractally rough surface terminated with trimethylsilyl and trifluoropropyl ligands. This coating process can be applied to many materials. In the experiments presented here, the materials are limited to sandpaper (aluminum oxide particles on paper substrate) and smooth acrylic polymer. Scanning electron microscope images of the coated acrylic polymer and sandpaper (characteristic feature size 15 μm) are shown in Fig. 3. The thickness of the coating is about half a micron, and on micron and submicron scales the surface features in both cases are fairly similar, including the microcracks.

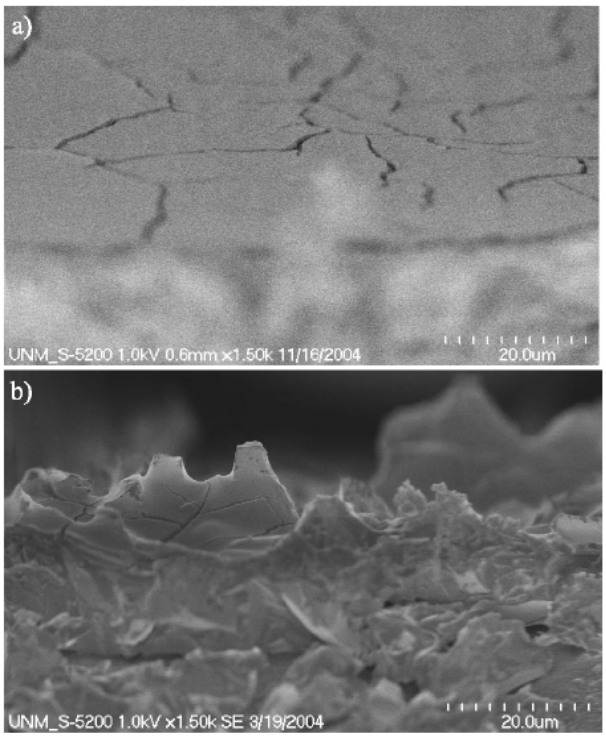

Figure 3. SEM images of SH-coated surfaces: (a) smooth acrylic polymer, (b) sandpaper (characteristic roughness 15 μm). Note that the submicron surface features produced by the SH coating are much smaller than the substrate roughness in the latter case.

SH coating applied to a smooth acrylic substrate produces a contact angle of 156° with water. Coated sandpaper has an irregularly textured surface not unlike those considered in Ref. 5. Some preliminary experiments were also conducted with grooved SH-coated surfaces. For these, photographs of a drop resting on the surface [Fig. 1a] clearly showed alternating contact-no-contact areas, as also previously reported in Ref. 9.

In experiments with the inclined surface, the tilt angle of the incline was varied from 1° to 3°, and a 30 frame-per-second digital video camera (720 by 480 resolution) was mounted at 90° to the plane of the sample. Here we present observations with three types of SH-coated samples: 1,200 grit sandpaper (irregular surface texture, characteristic feature size 15 μm), 2,400 grit sandpaper (similar texture with feature size 8 μm), and mirror-smooth acrylic substrate. From here on, this surface will be referred to as "untextured" or "smooth," although it still has surface features due to the application of the SH coating. Without the coating, each of the materials is hydrophilic. For each material, at least two samples were coated and mounted on the incline. Video records were analyzed to produce sequences of centerline positions for drops moving down the incline. These sequences were then ensemble averaged for each material type, solution type (pure water, 2:1 $ZnCl_2$:water, etc.), and tilt angle.

Figure 4 shows ensemble-averaged trajectories for water drops, tilt angle 2°. Drops move down surfaces with irregular textures faster than down the untextured surface, suggesting that macroscopic motion of the drops down the textured incline can be interpreted as a combination of rolling and sliding with a nonzero effective slip velocity produced by a mechanism similar to that shown in [Fig. 1d]. Not unexpectedly, comparison with the trajectories for

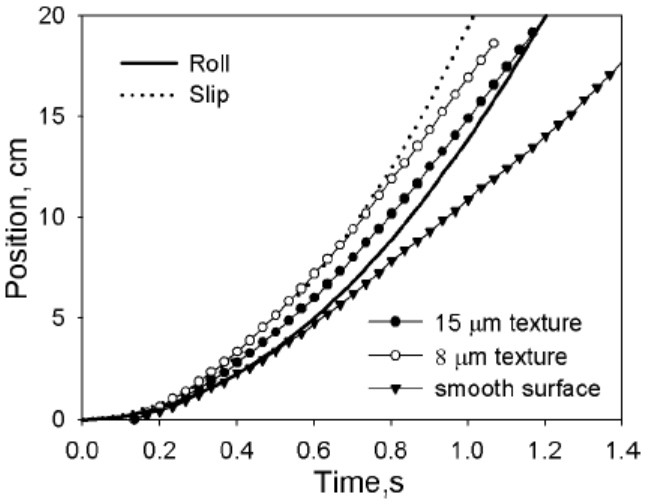

Figure 4. Ensemble-averaged position of the drop rolling down the SH-coated surface vs time. Plots for each material are labeled in the graph. For reference, graphs for a solid-body rolling and frictionlessly sliding down the

the ideal cases of solid-body roll and slide show that the drops are initially moving faster than they would if they were in solid-body rolling mode. Untextured SH-coated surface is characterized by much lower velocities than the textured surfaces, and the drop on this surface reaches a terminal velocity of about 16 cm/ s, compared with 25 cm/ s for the 15 μm and 26 cm/ s for the 8 μm surfaces. Experiments with 1:1 and 2:1 $ZnCl_2$:water solutions show similar results, but with decreasing terminal velocities. The theoretical terminal velocity of the water drop[9] is on the order of meters per second for our parameter values. This disagreement is not surprising: our drops are larger and much less viscous than the glycerol drops for which the terminal velocity results were consistent with the theory.[12]

In hydrofoil experiments, we measure the drag for the following surface types: SH-coated textured surface with 15 μm and 8 μm roughness, the same rough surface without the coating, and coated smooth acrylic surface. Once again, the SH coating of the surface with 8 μm roughness manifests the greatest apparent drag reduction – 18% compared with the untextured hydrofoil for Re=1,500. This consistency with the droplet experiment is in agreement with our notion of the similar physical mechanism responsible for effective slip velocity in both cases. As Re increases, the drag reduction becomes smaller (7% at Re=11,000). The same textured surface *without* the SH coating is characterized by a several percent *increase* in drag compared with the untextured surface. Figure 5 shows the

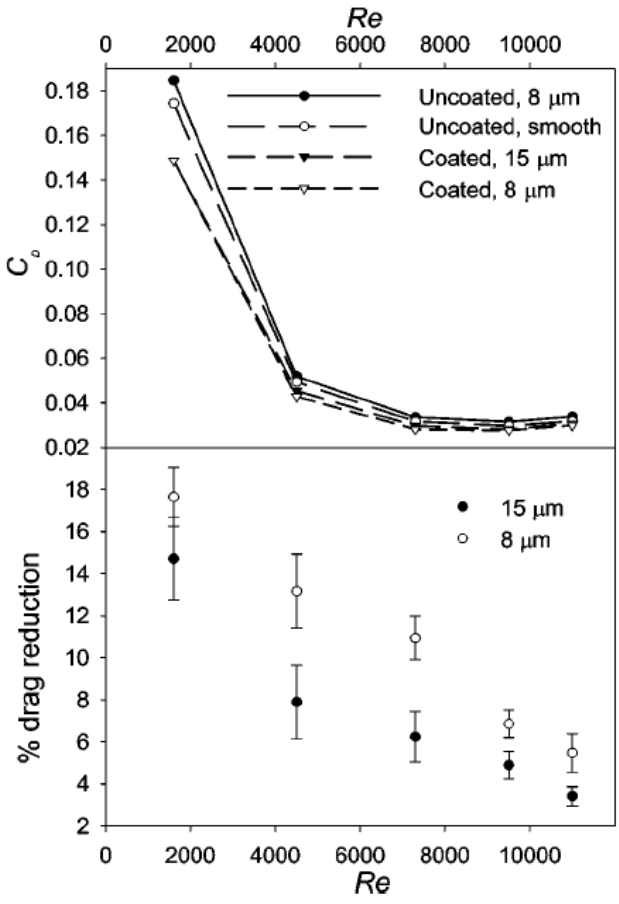

Figure 5. Top—drag coefficient *CD* on a Joukovsky hydrofoil in a water tunnel as the function of Reynolds number for different surface treatments. Curves corresponding to each surface type are labeled in the graph. Bottom—drag reduction for coated textured surfaces compared with smooth surface.

dependence of drag coefficients of each surface on Re, as well as the percentage of drag reduction for the textured surfaces compared with the untextured surface. Drag coefficient C_D represents the normalized drag force D: $C_D = 2D/(\rho U_\infty^2 S)$, where S is the cross-sectional area of the hydrofoil in the direction of the freestream.

The drag force can be related to the average value of the skin friction coefficient: $D \sim A\overline{\tau_w} = A\nu\rho(\overline{\partial U/\partial y})_w$, where A is the hydrofoil surface area, denotes averaging over this area, the subscript w indicates the value on the surface (wall), and y is the local coordinate normal to the surface. Usually the boundary of the fluid and the surface coincide. In our case, this condition is violated on the scales commensurate with the characteristic texture size of the SH coated surface. Equation (1) should still hold on the macroscopic scale that does not resolve the surface features. The actual velocity on the fluid boundary will alternate between zero in contact areas and nonzero in areas above voids [Fig. 1a], but on the same macroscopic scale it will average to a nonzero slip velocity U_s.

For the hydrofoil experiments, the ratio U_s/U_∞ can be inferred from the drag reduction. We can estimate the boundary layer thickness δ at mid-chord $x=L/2$ using the Blasius similarity solution for the flat plate.[13] $\delta \sim 5\sqrt{\nu x/U_\infty}$. For the range of the Reynolds numbers we investigated, δ is on the order of 1 mm, large compared with the characteristic scale associated with the surface texture (10 μm). Thus we assume that the boundary layer thickness on the hydrofoil is unaffected by the surface texture and coating. Further we assume that the velocity profile for the textured surface can be related to that for the smooth surface as follows. For the smooth surface $U=0$ at $y=0$; for the textured surface $U=U_s$ at $y=0$, but the shape of the profile of $U-U_s$ in the boundary layer is still described by the same similarity solution as that of U in the smooth surface case. Then from simple geometric considerations it follows that $U_s/U_\infty = 1-\tau_{w,t}/\tau_{w,s}$ where the subscripts t and s correspond to the estimates of t_w for the cases of textured and smooth surface using our drag measurements and Eq. (1). For the best-case scenario (textured SH-coated surface with feature size ~ 8 μm), this slip velocity estimate is 0.5 cm/s for Re =1,500, U_∞=3.7 cm/s and 1.4 cm/s for Re=11,000, U_∞ =25.6 cm/ s. Overall, the ratio U_s/U_∞ appears to decrease with Re.

The measurements reported here are rather preliminary, and a more thorough study of the combined effects of surface texturing and SH coating on the fluid flows near the surface is certainly warranted. Specifically, measurements of rolling drop and external flow properties near regularly textured (grooved) surfaces would be very interesting. For the external flow, it would also be highly desirable to acquire the velocity profiles in the immediate vicinity of the surface, especially near the leading edge of the hydrofoil, where the boundary layer is the thinnest and where most of the drag accumulates. In this area, the effective slip length might well be on the order of 10% of the boundary layer thickness, which would explain the considerable drag reduction observed. Any future study should also concentrate on determining the optimal size of the surface texture feature to minimize the drag.

(1) C. Navier, “Memoire sur les lois du mouvement des fluids,” Memoires de l’Academie Royale des Sciences de l’Institut de France **6**, 389 s1823d.
(2) J. Baudry and E. Charlaix, “Experimental evidence for a large slip effect at a nonwetting fluid-solid interface,” Langmuir **2001**, 5232.
(3) V. S. J. Craig, C. Neto, and D. R. M. Williams, “Shear-dependent boundary slip in an aqueous Newtonian liquid,” Phys. Rev. Lett. **87**, 054504 s2001d.
(4) C.-H. Choi, J. A. Westin, and K. S. Breuer, “Apparent slip flows in hydrophilic and hydrophobic channels,” Phys. Fluids **15**, 2897 s2003d.
(5) Y. Zhu and S. Granick, “Limits of the hydrodynamic no-slip boundary condition,” Phys. Rev. Lett. **88**, 106102 s2002d.
(6) E. Lauga and H. A. Stone, “Effective slip in pressure-driven Stokes flow,” J. Fluid Mech. **489**, 55 s2003d.
(7) Z. Yoshimitsu, A. Nakajima, T. Watanabe, and K. Hashimoto, “Effects of surface structure on the hydrophobicity and sliding behavior of water droplets,” Langmuir **2002**, 5818.
(8) J. Ou, B. Perot, and J. P. Rothstein, “Laminar drag reduction in microchannels using ultrahydrophobic surfaces,” Phys. Fluids **16**, 4635 s2004d.
(9) L. Mahadevan and Y. Pomeau, “Rolling droplets,” Phys. Fluids **11**, 2449 s1999d.
(10) J. Kim and C.-J. Kim, “Nanostructured surfaces for dramatic reduction of flow resistance in droplet-based microfluidics,” Proceedings of the IEEE Conference MEMS, Las Vegas, NV, 2002.
(11) S. S. Prakash, C. J. Brinker, and S. M. Rao, “Silica aerogel films prepared at ambient pressure by using surface derivatization to induce reversible drying shrinkage,” Nature sLondond **374**, 439 s1995d.
(12) D. Richard and D. Quéré, “Viscous drops rolling on a tilted non-wettable solid,” Europhys. Lett. **48**, 286 s1999d.
(13) H. Blasius, “Grenzschichten in Flüssigkeiten mit Kleiner Reibung,” Z. Math. Physik, Bd. **56**, 1 s1908d.

Chapter 4. Characterization of Superhydrophobic Materials Using Multiresonance Acoustic Shear Wave Sensors

In recent years, a variety of synthetic approaches have been developed to create so-called superhydrophobic (SH) surfaces characterized normally by high static contact angles of water (>150◦) [1]–[4]. Superhydrophobicity depends on surface roughness and surface chemistry, but to date rigorous structure-property relationships have not been established, especially the relationship between static and dynamic properties and how superhydrophobicity is influenced by nanoscale structural features. In this paper we use high-frequency shear acoustic waves generated by a piezoelectric quartz resonator thickness-shear mode (TSM) sensor to interrogate SH surfaces loaded with liquid media. For the TSM operating in the frequency range of 1 to ~100 MHz, the depth of penetration is on the order of tens to thousands of nanometers [5]; therefore, these sensors are sensitive to nanoscale interfacial phenomena and processes. Moreover, because the depth of penetration decreases with increasing TSM frequency, a multiresonance excitation of the sensor allows spatial interrogation of the interface with controllable interrogation depth. The purpose of this investigation is to evaluate the multiresonance TSM sensing technique to study the dynamic behavior of the SH/H_2O interface and to correlate the multiresonance TSM (MTSM) response with microscopic and nanoscopic features of SH surfaces. Although all the SH surfaces in this study had similar macroscopic wettability (optical contact angle ~150º), MTSM showed different responses, depending on the surface treatments and film morphology. Thus, MTSM sensing may provide a new means of probing the functional behavior of SH films and help establish needed structure-property relationships.

Experiment

The TSM sensors were 10 MHz fundamental resonant frequency quartz crystals AT-cut and coated initially with gold electrodes on both sides. Five samples of varying hydrophobicity were prepared by coating the sensors and subjecting the coating to various surface treatments (Table I summarizes the sample preparation). Sample 1 was

Films and surface treatment	θ	A[6]	Schematic	Water drop on TSM sensors*
1. Gold, no surface treatment	80°	0%		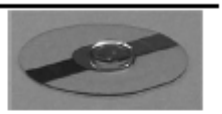
2. SH[1] film, no surface treatment	140°	17%	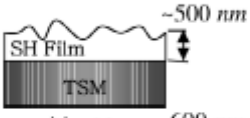	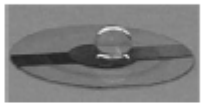
3. SH[1] film + HMDS[2] surface treatment	155°	43%	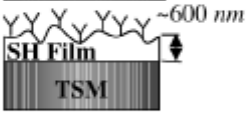	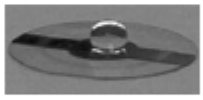
4A. NP[3] mixed SH[1] film + HMDS[2] surface treatment	155°	46%	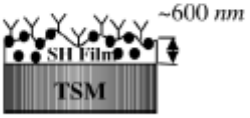	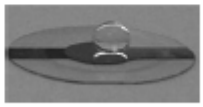
4B. NP[3] mixed SH[1] film + HMDS[2] + UV[4] treatment	90°		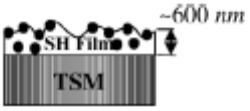	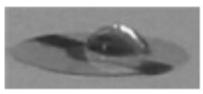

Table I. Physical Properties of SH-Films Deposited on MTSM Sensors.
*These pictures show a water droplet on the various SH surfaces studied; however, for the MTSM experiments the sensors were completely covered by a ~4-mm layer of DI water. SH[1] film: TFPTMOS. HMDS[2], (Y) hexamethyldisilizane, enhances hydrophobicity by replacing hydroxyl groups with trimethyl silyl groups. NP[3], (•) silica nano particles (sizes between 22~66 nm) increase the surface roughness and geometrical SH mechanism. UV[4], Ultraviolet light treatment reduces the water contact angle by removal of trimethyl silyl and trifluoropropyl groups. θ[5], contact angle measured optically. A[6], increase in surface area relative to bare surface measured by AFM (%)

a bare TSM sensor and Samples 2 to 4A were coated with SH coatings of increasing hydrophobicity. Sample 2 was coated with TFPTMOS (trifluoropropyltrimethoxysilane) to produce a low-surface, free energy with submicron-scale roughness [4]. Sample 3 also had a TFPTMOS coating but was further treated with HMDS (hexamethyldisilizane) to derivatize any remaining hydroxyl groups with hydrophobic trimethyl silyl Si(CH3)3 groups on the surface. Sample 4A was prepared by the same techniques as Sample 3 but with the addition of silica nanoparticles (2% by weight) to the TFPTMOS coating, followed by treatment with HMDS. Sample 4B is the same MTSM sensor and coating as Sample 4A but after exposure to ultraviolet (UV)/ozone to reduce its hydrophobicity. All the SH samples were prepared in the laboratory at the University of New Mexico.

The samples were characterized for macroscopic contact angle and surface roughness. Contact angle was measured by the sessile drop method [6]. The surface topology and roughness of samples was measured using atomic force microscopy (AFM) [7]. The AFM images of the SH surfaces were obtained in 3 μm × 3 μm areas

and are shown in Fig. 1. The AFM software enables analysis of relative changes of surface area (Table I).

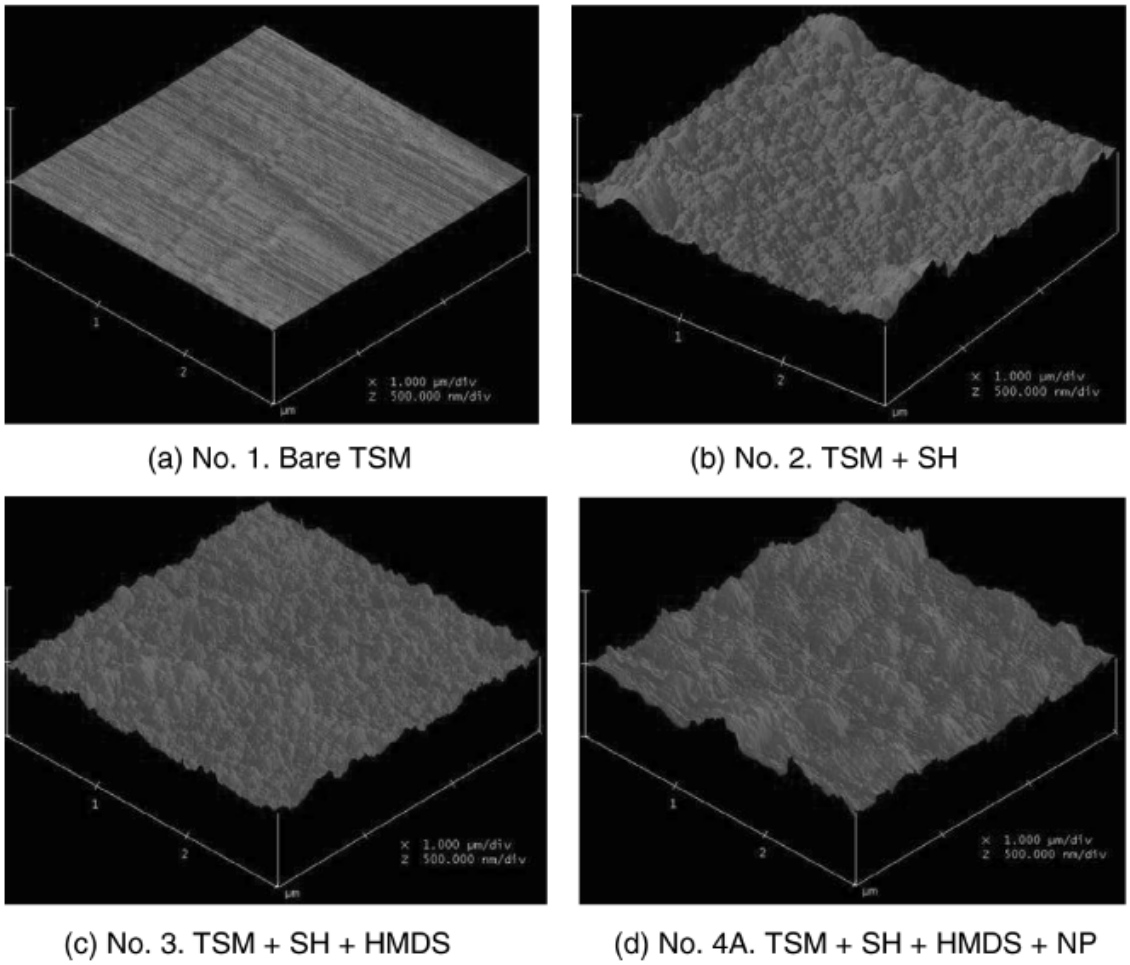

Fig. 1. AFM images of SH films on MTSM sensors. (a) Sample 1, surface of gold electrode on the MTSM sensor; (b) Sample 2; (c) Sample 3; and (d) Sample 4A.

Results and Discussion

The measured macroscopic optical contact angles of water on each of the samples are reported in Table I along with images of a water droplet resting on the sample surface. The contact angle increases from approximately 80º on the bare MTSM sensor to 140º to 155º for the SH coatings; Ultraviolet/ozone treatment reduces the contact angle to approximately 90º by changing the surface energy without affecting morphology. Samples 2, 3, and 4A are all SH with contact angles of 140º or more. The addition of silica nanoparticles in Sample 4A does not significantly increase the contact angle compared to Sample 3. The surface area of the samples, as measured by AFM

(Fig. 1), increases steadily from Sample 1 to 4A. The surface area of Sample 4A was approximately 46% larger than the initial surface area because of roughness resulting from the surface treatment. Samples 3 and 4A had similar surface areas and exhibited high contact angles characteristic of SH surfaces. So according to standard static characterization protocols, both Samples 3 and 4 were equally SH.

A network analyzer measurement system was used to monitor the frequency response of the MTSM sensor exposed to air or submersed in 200 μl (about 4-mm depth) of deionized (DI) water [5]. All measurements were performed in an air-flow controlled chemical hood at room temperature (approximately 25ºC ± 0.1ºC). The multiharmonic frequency response characteristics (i.e., resonant frequency and attenuation at first, third, fifth, and seventh harmonics) of coated MTSM sensors were measured when the sensors were exposed to air (dry) and when covered with a ~4-mm layer of water (wet). The relative changes of resonant frequency of the wet and dry sensors [$\Delta f_{\text{rel.}}(1)$] are plotted in Fig. 2(a): $\Delta f_{rel.} = \left(f_{dry} - f_{wet}\right) / f_{dry}$, (1) where f_{dry} and f_{wet} indicate resonant frequencies of dry and wet conditions, respectively. Changes in attenuation also were measured but are not reported here. Two obvious phenomena can be extracted from Fig. 2(a):

- Sample 4A always shows smaller $\Delta f_{\text{rel.}}$ than the other samples at all harmonics.
- At higher harmonics (fifth and seventh), $\Delta f_{\text{rel.}}$ of Samples 2 and 3 are greater than Sample 1, and $\Delta f_{\text{rel.}}$ of Sample 4A is still smaller than Sample 1.

Sample 4A exhibits much less response to water loading at all the tested harmonics. These trends can be explained based on the hypothesis that, although the macroscopically observed contact angle of water on the SH surfaces are similar, the mechanics of interaction near the water-SH coating interface differ. It is commonly understood that on rough SH surfaces, water does not wet the entire surface at the microscopic or nanoscopic level [4]. Rather at the level of the roughness, water contacts the peaks protruding from the surface but does not penetrate into the valleys, which are filled with air or vapor. For the SH films tested here, the actual penetration depth of the water layer into the valleys of the rough SH surface are dependent on the conditions (surface wettability) of the SH surface, with Sample 4A exhibiting much less interaction (i.e., less water penetration into roughness). At the macroscopic scale, this

reduced interaction could be interpreted as effective slip between the liquid and SH surface due to the reduction of the effective contact area [4], [8], [9].

The MTSM responses displayed in Fig. 2(a) show that SH surfaces with similar contact angles can exhibit different mechanical interactions with water. The contact angle of water droplets on the surface of Samples 2, 3, and 4A are similar with approximately 150º, but the response of MTSM sensors to DI water loading of each SH sample are different and are dependent on the harmonics. Different harmonics probe different acoustic penetration depths into the liquid, with higher harmonics more sensitive to liquid trapped in submicron valleys.

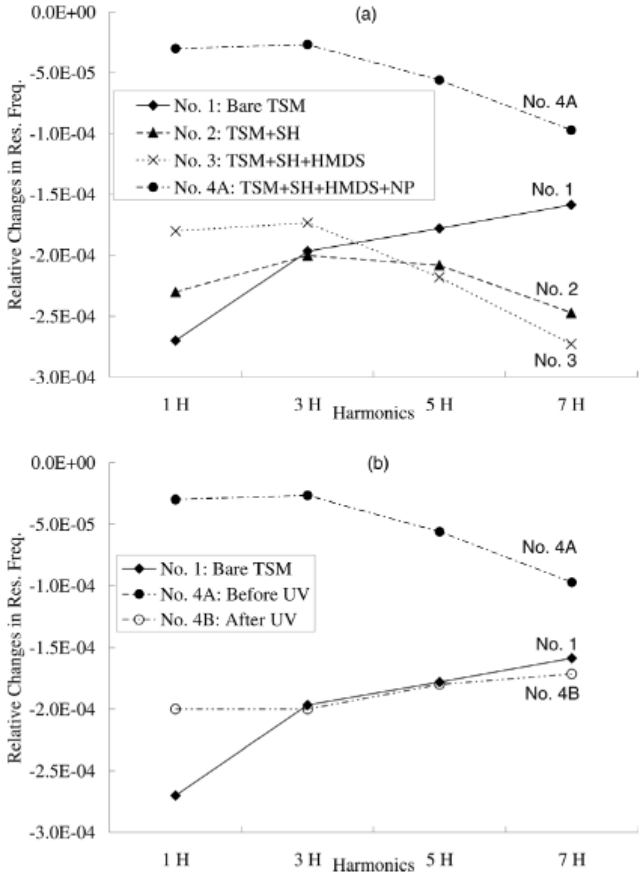

Fig. 2. Relative changes in Δ*f* for (a) MTSM-SH sensors at harmonics, and (b) Sample 4A (before UV), Sample 4B (after UV), and Sample 1 (bare MTSM).

Sample 4B was produced from Sample 4A by treatment with UV light for about 30 minutes. This UV/ozone treatment does not change the surface morphology; rather it replaces hydrophobic CH3 and CF3 groups with hydrophilic hydroxyl groups via an ozone mediated, photo-oxidative process. The contact angle of water on Sample 4B was approximately 90◦ (see Table I). Again, the frequency responses of Sample 4B were monitored and compared with those of the SH film before UV treatment (Sample 4A) and the bare MTSM (Sample 1). As shown in Fig. 2(b), the relative changes of resonant frequency ($\Delta f_{rel.}$) of the UV treated sample (Sample 4B) in response to water loading approaches that of the bare MTSM (Sample 1). The $\Delta f_{rel.}$ curves for Samples 4B and 1 overlap, except for the first harmonic. Although the morphology of the surface of Sample 4B is virtually identical to that of 4A, the surface free energy of Sample 4B is higher than 4A due to the UV treatment as

evidenced by the much lower contact angle of water. Higher surface free energy allows water to penetrate deeper into the valleys. Sample 4B senses the additional mass effect from the trapped water and additional viscous damping from the water load on the SH films. Sample 4B shows a similar response to Sample 1 at larger values of resonant frequency.

Summary and Conclusions

Three superhydrophobic (SH) and two control surfaces were fabricated by five different processes to produce surfaces with varying wettability and submicron scale roughness. The surfaces were characterized with three methods: the acoustic response of MTSM sensors to water loading, nano-scale surface morphology by AFM, and optical measurements of contact angle of water droplets. The AFM measured increases in surface area of 17 to 46% due to roughness of surface treatments. The differences in data were next supported by MTSM results, which also showed the significant differences between those coatings. However, the optical measurements of macroscopic contact angles did not detect differences between the SH coatings. Specifically, the three SH coatings (Samples 2, 3, and 4A), fabricated with and without nanoparticles and with different chemical treatments showed similar macroscopic contact angles; the optical method was capable of only measuring the difference between less hydrophobic Samples 1 and 4B and more hydrophobic Samples 2, 3, and 4A. Thus, although the contact angles of water droplets are similar on all SH films (samples 2, 3, and 4A), the acoustic method using MTSM sensors clearly exhibited different responses in each sample. It is interesting to notice that the MTSM responses were dependent on the harmonic frequency. Sample 4A showed a much smaller frequency shift under water loading than the other samples; this film incorporated three techniques to provide SH: low free surface energy TFPTMOS coating, HMDS surface treatment, kwoun *et al.*: characterization of superhydrophobic materials 1403 and addition of nano-particles in TFPTMOS. The combination of these factors produces a sample SH coating with the optimized SH properties. These MTSM results can be interpreted as the presence of effective slip on the textured surface [4].

References

[1] Z. Yoshimitsu, A. Nakajima, T. Watanabe, and K. Hashimoto, “Effects of surface structure on the hydrophobicity and sliding behavior of water droplets,” *Langmuir*, vol. 18, pp. 5818–5822, 2002.

[2] J. Kim and C. Kim, “Nanostructured surfaces for dramatic reduction of flow resistance in droplet-based microfluidics,” in *Proc. IEEE Conf. MEMS*, 2002, pp. 479–482.

[3] L. Zhai, F. C. Cebeci, R. E. Cohen, and M. F. Rubner, “Stable superhydrophobic coatings from polyelectrolyte multilayers,” *Nano Lett.*, vol. 4, pp. 1349–1353, 2004.

[4] S. Gogte, P. Vorobieff, R. Truesdell, A. Mammoli, F. van Swol, P. Shah, and C. J. Brinker, “Effective slip on textured superhydrophobic surfaces,” *Phys. Fluids*, vol. 17, pp. 051701-1–051701-4, 2005.

[5] G. L. Cote, R. M. Lec, and M. V. Pishko, “Emerging biomedical sensing technologies and their applications,” *IEEE Sens. J.*, vol. 3, pp. 251–266, 2003.

[6] K. Rogers, E. Takacs, and M. R. Thompson, “Contact angle measurement of select compatibilizers for polymer-silicate layer nanocomposites,” *Polymer Testing*, vol. 24, pp. 423–427, 2005.

[7] H. Yang, H. An, G. Feng, and Y. Li, “Visualization and quantitative roughness analysis of peach skin by atomic force microscopy under storage,” *LWT—Food Sci. Technol.*, vol. 38, pp. 571–577, 2005.

[8] G. McHale, R. Lucklum, M. I. Newton, and J. A. Cowen, “Influence of viscoelasticity and interfacial slip on acoustic wave sensors,” *J. Appl. Phys.*, vol. 88, pp. 7304–7312, 2000.

[9] G. McHale and M. I. Newton, “Surface roughness and interfacial slip boundary condition for quartz crystal microbalances,” *J. Appl. Phys.*, vol. 95, pp. 373–380, 2004.

Chapter 5. Drying transition of confined water

Long-range hydrophobic interactions operating underwater are important in the mediation of many natural and synthetic phenomena, such as protein folding, adhesion and colloid stability. Here we show that rough hydrophobic surfaces can experience attractive forces over distances more than 30 times greater than any reported previously, owing to the spontaneous evaporation of the intervening, confined water. Our finding highlights the importance of surface roughness in the interaction of extended structures in water, which has so far been largely overlooked.

The existence of 'long-range' hydrophobic interactions has been debated for more than 25 years[1–5], because their reported range of 1–100 nm exceeds that of van der Waals forces and cannot be explained by water restructuring. However, investigations have been limited to smooth, flat model surfaces[4], even though most surfaces are rough. Roughness strongly influences wetting — as evidenced by the high water-contact angles ($\theta \geq 160^{\circ}$) and rolling of water droplets on lotus leaves[6].

Knowing that superhydrophobic surfaces occur naturally and that living systems operate mainly in water, we investigated the interaction of rough superhydrophobic surfaces beneath the water surface. Interfacial-force microscopy[7] and optical imaging were used to examine the interaction between two approaching or retracting superhydrophobic surfaces (water contact angle θ of about 170°; see supplementary information) submerged in either airequilibrated or de-aerated water.

We discovered a very-long-range hydrophobic interaction that was due to out-of-contact evaporation, or 'cavitation', of the intervening water at tip-to-substrate separations ranging from 0.8 μm to as much as 3.5 μm. Cavitation is a first-order phase transition characterized by a sudden, strong attractive force (Fig. 1a) and by the appearance of a vapor bridge spanning the tip-to-substrate gap (Fig. 1 b–e, and see supplementary information for details).

Pre-existing 'nanobubbles' of a size commensurate with the interaction length have been proposed as a source of long-range interactions[8]. We therefore used *in situ* confocal imaging to search for bubbles on an isolated, flat superhydrophobic surface (for details, see supplementary information). Neither the microscopy nor neutron

reflectivity experiments[9] provide evidence for bubbles — certainly not micrometer-sized

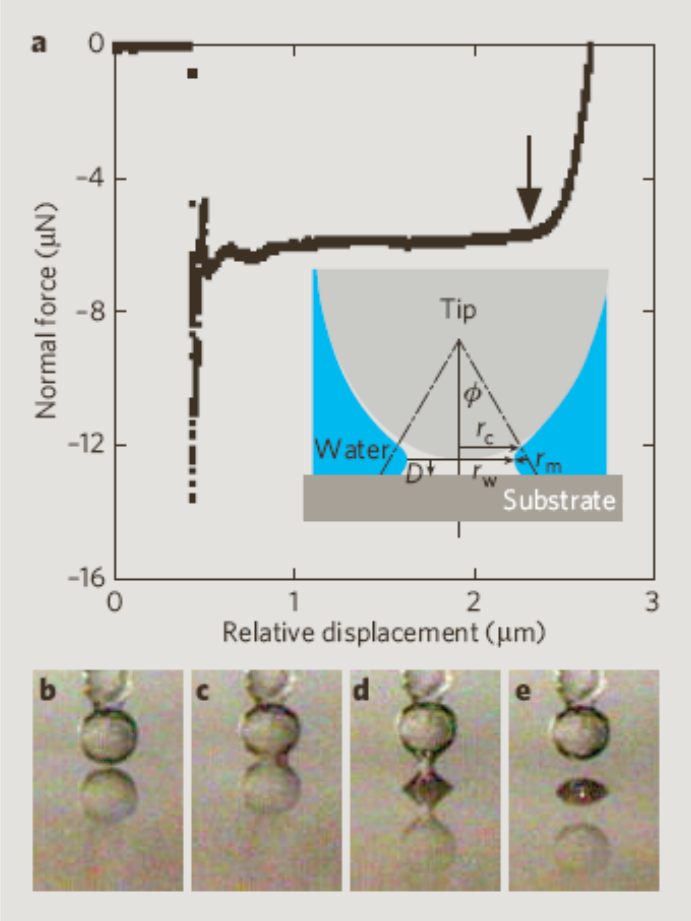

Figure 1. Cavitation between superhydrophobic surfaces (**a**) Plot of force versus displacement for the underwater approach of a tip towards a flat surface. The experiment starts at zero micrometers relative displacement (arbitrarily defined). The sudden development of a negative (attractive) force at about 0.4 μm relative displacement corresponds to cavitation. Contact with the surface is indicated by the inflection at about 2.2 μm (arrow). The distance between the onset of adhesion and contact (1.8 μm) is the distance over which cavitation occurs for this sample. The inset shows the cavitation geometry: $\Delta p=\gamma(1/r_w - 1/r_m)$, where Δp is the pressure difference across the interface, γ is the liquid–vapor interfacial tension, r_m is the radius of the meniscus, r_w is the radius of its waist, and r_c is the contact radius of the cavity on the tip surface. D is the critical separation below which cavitation is thermodynamically favored. See also supplementary information. (**b–e**) Optical images of cavitation: **b**, position of superhydrophobic tip and substrate just before cavitation; **c**, cavitation occurs about 33 ms later; **d**, cavity meniscus, as seen during tip retraction, one frame before its unstable collapse; **e, a** cavity 'bubble' is left behind on both the tip and substrate. These bubbles, attributed to air supplied from water and the porous SH surface, are unstable and are readsorbed in about 6 seconds. In all frames, the circular image at the bottom is the reflection of the spherical 150-μm-diameter tip in the flat SH surface.

bubbles. We therefore argue that cavitation is a consequence of, and thermodynamically consistent with, the properties of confined water[10]. The critical

separation, D, below which cavitation is thermodynamically favored can be estimated from Laplace's equation as 1.4 μm (see supplementary information): this is a lower bound and will increase if Δp, the pressure difference across the interface, is reduced by incorporation of air into the cavity.

Unambiguous cavitation has previously been observed only following the contact of smooth hydrophobic surfaces[3,8,11]. Although it is thermodynamically acceptable, out-of-contact cavitation has been modeled as having a large activation barrier[12], so we need to explain why we observe it and how kinetic barriers are surmounted.

First, we used interfacial-force microscopy[7], in which interfacial forces are counterbalanced, to avoid snap-to-contact (when the rate of change of the force exceeds the spring constant and the two surfaces snap together uncontrollably, as occurs in atomic-force microscopy and in surface-force apparatus studies[5]). Second, the calculated D for submerged superhydrophobic surfaces is more than ten times that of smooth surfaces, which increases the probability of cavity nucleation at larger separations. Third, the submerged superhydrophobic surface presents an intrinsic liquid/vapor/solid interface, which may serve as a heterogeneous nucleation surface.

We simulated the molecular dynamics of a model fluid, which showed the necessary liquid–vapor behavior, confined between two closely spaced surfaces containing opposing (θ =180º) superhydrophobic patches. The simulations show that cavitation occurs by the growth of capillary-like fluctuations of vapor films extending from the super hydrophobic surfaces, leading to the sudden formation and growth of a vapor bridge.

Our experiments reveal that cavitation can be one source of long-range hydrophobic interactions. For rough surfaces, the interaction length extends to micrometer scales. Correspondingly, interaction lengths of hundreds of nanometers, observed for smooth surfaces (for example, snap-to-contact), might also be explained by cavitation, in agreement with thermodynamic expectations.

References

1. Blake, T. D. & Kitchener J. A. *J. Chem. Soc. Farad. Trans. 1* 68, 1435–1442 (1972).
2. Christenson, H. K. & Claesson, P. M. *Adv. Colloid Interface Sci.* 91, 391–436 (2001).

3. Christenson, H. K. & Claesson, P. M. *Science* 239, 390–392 (1988).
4. Israelachvili, J. & Pashley, R. *Nature* 300, 341–342 (1982).
5. Stevens, H., Considine, R. F., Drummond, C. J., Hayes, R. A. & Attard, P. *Langmuir* 21, 6399–6405 (2005).
6. Lafuma, A. & Quéré, D. *Nature Mater.* 2, 457–460 (2003).
7. Joyce, S. A. & Houston, J. E. *Rev. Sci. Instr.* 62, 710–715 (1991).
8. Parker, J. L., Claesson, P. M. & Attard, P. *J. Phys. Chem.* 98, 8468–8480 (1994).
9. Doshi, D. *et al. Langmuir* 21, 7805–7811 (2005).
10. Lum, K., Chandler, D. & Weeks, J. D. *J. Phys. Chem. B* 103, 4570-4577 (1999).
11. Pashley, R. M., McGuiggan, P. M., Ninham, B.W. & Evans, F. D. *Science* 229, 1088–1089 (1985).
12. Luzar, A. *J. Phys. Chem. B* 108, 19859–19866 (2004).

Supplementary Material for Chapter 5

Sample preparation

Superhydrophobic silica surfaces (contact angles of water ≥ 170° see Fig. S1) were prepared on spherical interfacial-force-microscopy tips and flat single crystal Si substrates using a variation of the low temperature/pressure aerogel thin film process developed in our lab[1] where a quarter of the tetraethylorthosilicate (TEOS) was replaced with 3,3,3 trifluoropropyltrimethoxysilane, and the as-deposited films were exposed to hexamethyldisilizane vapor at 50°C. Superhydrophobic surfaces were deposited by dipping (tips) or spin-coating (silicon substrates).

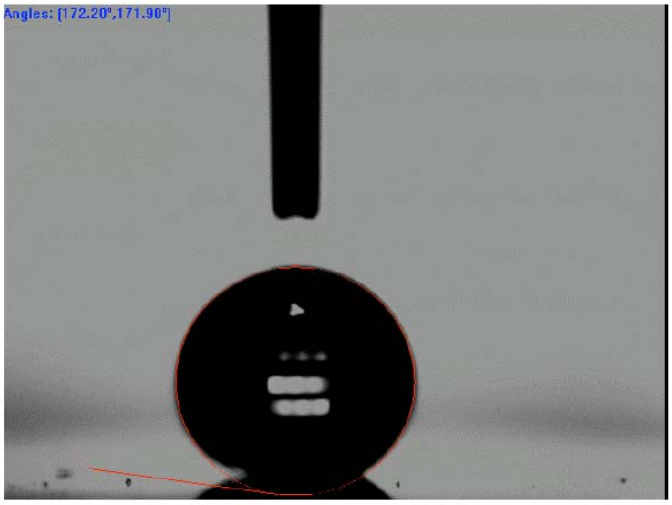

Figure S1. Water droplet on representative superhydrophobic surface prepared on a smooth flat silicon substrate. Contact angle ~ 172°.

Interfacial force microscopy

Interfacial force microscopy experiments were conducted in standard low conductivity (18.2 megaohms) de-ionized (DI) water and deaerated DI water (prepared by repeated freezing/pump/thaw cycles) with similar results. Advancing and retracting tip speeds were 100 nm/sec and 6 μm/sec respectively. We could not measure directly the contact angle of water on the 150-μm tip, so we qualified the tips by doing 'water denting'

experiments (Fig. S2, left) and ensuring that the associated force (Fig. S2, right) was purely repulsive with no measurable attractive force upon contact with the water surface. Video images were acquired using a CCD camera. Figure S3 shows a series of images where we observe out of contact cavitation occurring over a distance of ~3.0-μm.

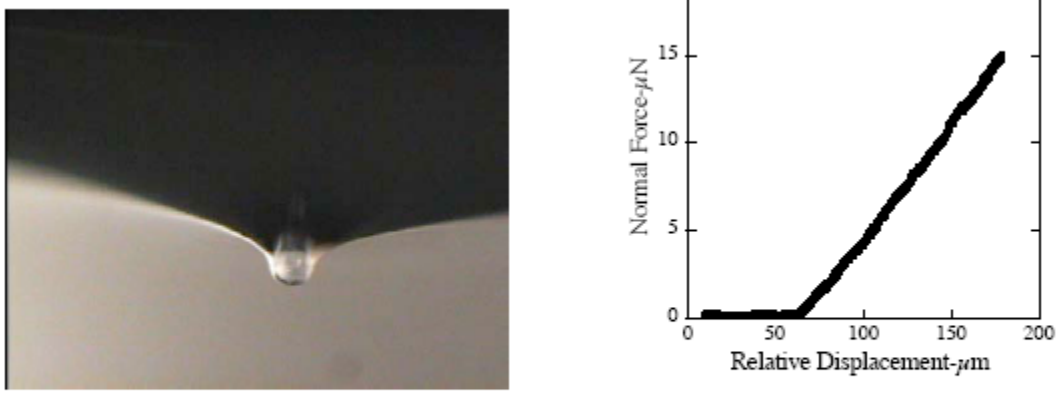

Figure S2. Water denting with the interfacial-force-microscopy probe (left) and force versus displacement plot corresponding to the approach of the superhydrophobic tip to the surface of water. The force is purely repulsive (positive) with no measurable attractive force upon contact.

Fig. S3. Movie frames showing out of contact cavitation at a distance of ~3 micrometres a) one frame prior to b, b) frame showing cavitation c) extended vapour cavity visible during withdrawal. Bottom semicircular shape is a reflection of the spherical superhydrophobic tip from the underlying flat superhydrophobic surface.

Confocal Fluorescence Imaging

Confocal fluorescence imaging was used to look for the presence of vapour bubbles at the superhydrophobic–water interface (see Fig. S4). It has been argued that these

'nanobubbles' are a source of long range hydrophobic interactions[2], and therefore, the growth and coalescence of pre-existing bubbles could conceivably be an explanation of the long range out of contact cavitation we observe. To perform these experiments the superhydrophobic film was fluorescently labeled with the water-insoluble green fluorescent dye fluorescein (Molecular Probes), and submerged in water containing the water-soluble red fluorescent dye rhodamine B (Kodak). Starting in the superhydrophobic film (green) optical sections taken at successively shallower focal planes show the progressive development of a patchwork of red regions corresponding to water and emphasizing the rough three-dimensional nature of the superhydrophobic–water interface. Whereas within the green regions we see heterogeneous black textural features (that eventually become infiltrated with red) indicative of the fractal, nanoscale porosity of the superhydrophobic surface, within the red (water) regions there is no evidence of vapor bubbles (which would appear as black (presumably circular) shapes) on length scales larger than 200 nm, which is the approximate resolution level of this technique. As the size of the pre-existing bubbles is argued to be the length scale over which long range hydrophobic interactions are observed, the absence of any 0.5-3.0-μm bubbles argues against their coalescence as being responsible for long range out of contact cavitation between submerged superhydrophobic surfaces. Rather cavitation is a consequence of the phase behavior of confined water, where spontaneous cavitation/drying is expected for separations below a critical dimension. For smooth hydrophobic surfaces this critical dimension has been modeled to be of the order of 100 nm.

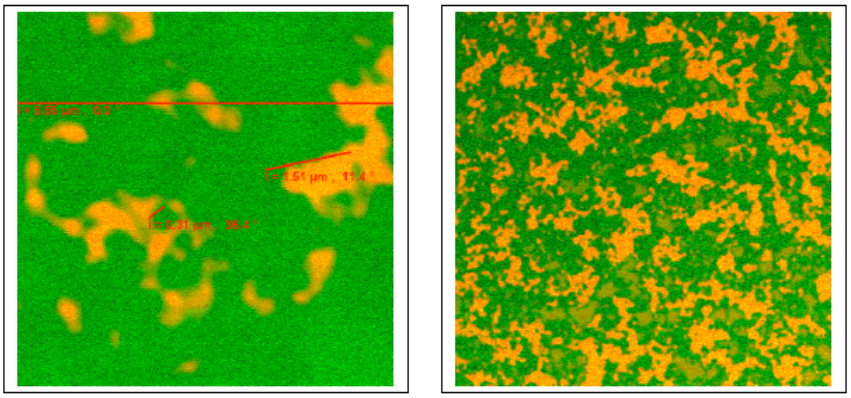

Fig. S4. Left, final frame from laser scanning confocal microscopy Movie 1 and right, final frame from Movie 2. Green corresponds to the nanoporous superhydrophobic film and red to water. There is no evidence of pre-existing nanobubbles, which would appear as black features within the red (water) background. Addition of dyes causes only very minor changes in the wetting characteristics.

Thermodynamics of cavity formation

The critical distance below which cavitation is thermodynamically feasible can be estimated from equating the grand potentials of the liquid and vapor configurations[3]. This naturally leads to an expression that is known as Laplace's equation

$$D = \frac{-2\gamma\cos\theta}{\Delta p} \qquad (1)$$

which expresses mechanical equilibrium across a curved interface[4–6]. At ambient conditions, 25 °C and atmospheric pressure (about 0.89 x 10^5 Pa in Albuquerque, New Mexico, USA) the pressure difference $\Delta p = p_l - p_v = 0.9 \times 10^5$ Pa and the air water interfacial tension, γ, is about 0.072 N/m. Thus, for a contact angle of 170° we find that D = 1.4 μ*m*. This must be considered a lower bound, as the cavity is assumed initially to be free of air and thus to contain only water vapour.

D will grow if the atmospheric pressure is reduced, by reducing the amount of air in the system. If all the air is removed, and the equilibrium considered is that between *pure* water and *pure* vapour, equation (1) is often expressed (see refs 3,6) in terms of the chemical potential difference, $\Delta\mu = \mu_l - \mu_{sat}$, between the chemical potential of the liquid phase and the bulk saturation value.

$$D = \frac{-2\gamma\cos\theta}{(\rho_l - \rho_v)\Delta\mu} = \frac{-2\gamma\cos\theta}{(\rho_l - \rho_v)mgh} \qquad (2)$$

The second form arises when we consider the variation of the chemical potential with distance, *h*, from the planar liquid–vapour interface in a gravitational field of acceleration g. Here m is the mass, and ρ denotes the number density. From equation (2) we see that in a *pure* water system, D = 1.45 mm when h = 1cm. The same observations regarding the role of the air on the value of *D* and similar estimates have been made elsewhere[7].

1. Prakash, S. S., Brinker, C. J., Hurd, A. J. & Rao, S. M. *Nature* **374,** 439–443 (1995).
2. Carambassis, A., Jonker, L. C., Attard, P, & Rutland, M. W. *Phys. Rev. Lett.* **80**, 5357– 5360 (1998).
3. Evans, R. *J. Phys. Condens. Matter* **2,** 8989 (1990).
4. Evans, R. & Marconi, U. M. B. *J. Chem. Phys.* **86,** 7138 (1987).
5. Parker, J. L., Claesson, P. M. & Attard, P. *J. Phys. Chem.* **98,** 8468 (1994).
6. Lum, K., Chandler, D. & Weeks, J. D. *J. Phys. Chem. B.* **103,** 4570 (1999).
7. Wennerström, H. *J. Phys. Chem. B* **107,** 13772 (2003).

Chapter 6. Capillary Phase Transitions

Introduction

We consider the effect of cavitation between two superhydrophobic surfaces, or more precisely capillary evaporation. As this phenomenon naturally takes place 'under water' it is important to address the role of gravity.

Phase equilibria: general considerations

At a given subcritical temperature, T, the conditions for bulk liquid-vapor coexistence are chemical and mechanical equilibrium:

$$\mu_l = \mu_g \qquad (1)$$
$$p_l = p_g$$

In what follows we will denote the value of the chemical potential and the pressure at bulk coexistence by μ_{sat} and p_{sat} respectively. Obviously, for single component system μ_{sat} and p_{sat} are only functions of T. When discussing phase transitions it is convenient to consider the μ, p plane, see figure 1. In this plane there exist a liquid and a gas branch each sloping. The slope of each phase is given by

$$\left(\frac{\partial \mu}{\partial p}\right)_T = \frac{1}{\rho_\alpha}, \alpha = l, g \qquad (2)$$

Coexistence, as expressed by equation 2, occurs at the intersection (μ_{sat}, p_{sat}) of the two branches. Note that each branch continues as a metastable branch beyond the point of intersection.

Phase equilibria in confined geometries

It is well known that confinement, as represented by capillaries, can induce a shift of the bulk phase transition. We will now explore this shift in more detail for the case of a slit consisting of two parallel walls, and introduce an expression that links the shift to the liquid-vapor surface tension, γ_{lv}, the density difference between the liquid and gas phases, and the contact angle, θ, that a liquid drop would exhibit on a single wall, see figure ??. Such geometry can induce a shift of the phase transition. We will see that if

the cosine of the contact angle, $cos\theta$ is positive, the shift will be in the direction of the vapor. That is, the liquid can form inside the capillary before that phase is stable in the bulk. This is known as capillary condensation. The opposite case, $cos\theta < 0$ leads to stabilization of the vapor phase inside the capillary before the vapor is stable in the bulk. This is a less common occurrence, and known as capillary evaporation or sometimes cavitation. Evaporation will be the main focus of this section. Once the geometry is determined (e.g., cylinder, slit, wedge), a relation between the chemical potential, the local pressure and the surface tension can be readily derived by equating the grand potential of the liquid and gas phase.

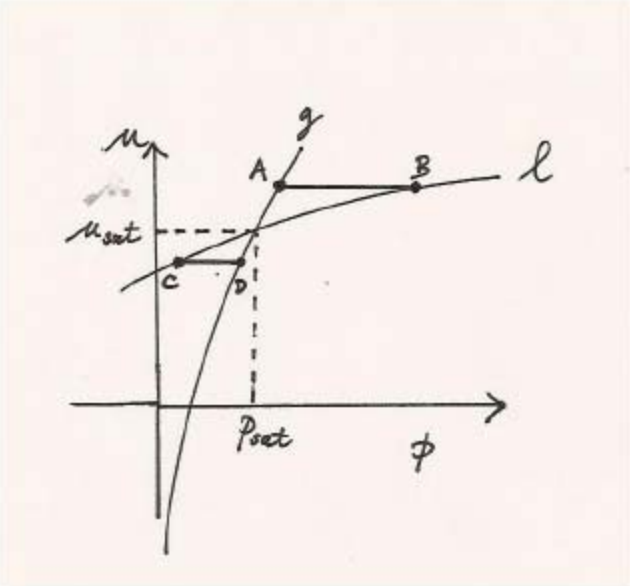

Figure 1: μ, p plane showing $\mu(p)$ for the liquid and the gas branch. Liquid-vapor coexistence occurs at the intersection of the two curves. The chemical potential and pressure at coexistence are labeled as μ_{sat} and p_{sat}. At any pressure the branch with the lowest chemical potential corresponds to the stable bulk phase. Capillary coexistence for chemical potentials above μsat is illustrated by the horizontal line AB. Point A indicates the gas phase that is stabilized by the capillary and point B indicates liquid phase. Since the liquid is the phase stable in the bulk, this is referred to as capillary evaporation. Similarly, the horizontal line CD indicates equilibrium between a gas and liquid phase for a chemical potential less than μ_{sat}. This is an example of capillary condensation, where the gas phase is the stable bulk phase. The slope of the $\mu(p)$ curves is equal to $1/\rho$, where ρ is the density at that p. In the vicinity of the coexistence point both curves can be approximated by straight lines, and hence by straightforward geometry one can easily express the pressure difference p(B) − p(A), say, in terms of μ(A) and $1/\rho_g$. Note that the figure is not drawn to scale. For example, for water at room temperature the ratio of the slopes at coexistence is approximately 43000.

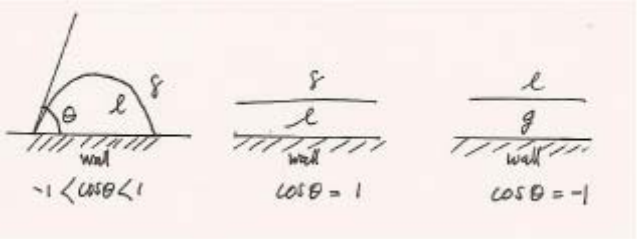

Figure 2: The definition of contact angle used in Young's equation (left panel), see equation 4 of the text. Complete wetting (middle panel) occurs when $\theta = 0$ or $\cos\theta = 1$. Complete drying (right panel) corresponds to $\theta = 2\pi$ or $\cos\theta = -1$.

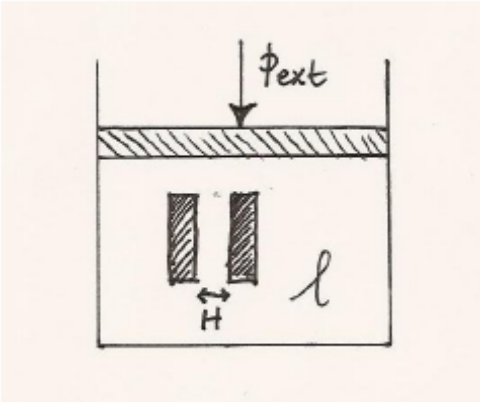

Figure 3: A schematic of an experimental route to studying capillary evaporation by controlling the pressure of the bulk liquid phase. At hydrostatic equilibrium the bulk liquid pressure, p, will be equal to the applied pressure, p_{ext}. Controlling the bulk liquid pressure at constant T is equivalent to controlling the liquid chemical potential, as $\mu = \mu(p)$ (see figure 1).

A detailed derivation is presented in Appendix A. Alternatively, we can expand the pressures of the liquid (cf. point B in figure 1) and gas phase (cf. point A in figure 1) around the saturation point and express the pressure difference between a gas and liquid at the same chemical potential $\mu \neq \mu_{sat}$ and equate the result with Laplace's equation for the pressure difference across a curved interface, which is $2\gamma_{lv}/H$. Thus, for a slit of width H the deviation in chemical potential from that at bulk coexistence is given by,

$$\Delta\mu \equiv \mu_l - \mu_{sat} = \frac{2\left(\gamma_{wl} - \gamma_{wg}\right)}{H\left(\rho_l - \rho_v\right)} \tag{3}$$

Upon using Young's equation,

$$\cos\theta = \frac{\gamma_{wl} - \gamma_{wg}}{\gamma_{lv}} \tag{4}$$

equation 3 can be rewritten as,

$$\Delta\mu = \frac{-2\gamma_{lv}\cos\theta}{H(\rho_l - \rho_v)} \tag{5}$$

which is the familiar form found in the literature. Note that since $\cos\theta < 0$ we have $\Delta\mu > 0$, as expected and indicated in figure 1. Conversely, we can express the distance, H, at which a vapor phase becomes stable in terms of a given $\Delta\mu$ as,

$$H = \frac{-2\gamma_{lv}\cos\theta}{(\rho_l - \rho_v)\Delta\mu} \tag{6}$$

$$\approx \frac{-2\gamma_{lv}\cos\theta}{\rho_l\Delta\mu} \tag{7}$$

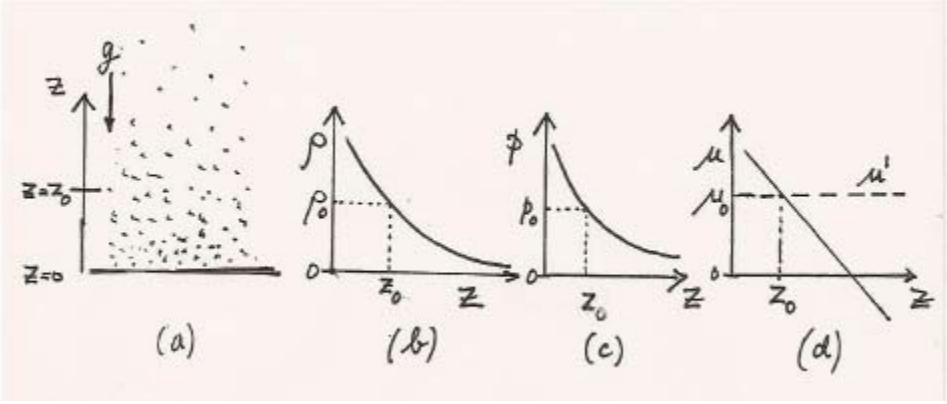

Figure 4: (a) A schematic of an ideal gas in a gravitational field. Gravity is pointed in the negative z-direction and is characterized by a gravitational accelration, g. z_0 indicates a reference height. (b) The exponential density distribution. (c) The exponential pressure distribution, and (d) the chemical potential. The total chemical potential, μ0 (dashed line), is a constant, independent of height. The fluid chemical potential (solid line), defined by equation 13, is a linear function of height.

4 The role of a gravitational field

4.1 ideal gas in a gravitational field

Now let us consider the effects of gravity. Gravity is a one-body external field, $V_{ext}(z)$, acting on (the points of mass of) the system. It is linear in the distance, and the potential energy associated with gravity is proportional to the mass of an atom, i.e., $V_{ext}(z) = mg(z - z_o)$, where z_0 defines the arbitrary zero of the external field. Any fluid in a gravitational field will exhibit a varying density and pressure increasing in the direction of gravity. A familiar example is the ideal gas for which we know all the thermodynamic

properties exactly, with or without an external field. The density distribution of an ideal gas consisting of atoms of mass, *m*, is given by (see figure 4):

$$\rho(z) = \rho_o e^{-mg(z-z_o)/kT} \tag{8}$$

where k is Boltzmann's constant, and ρ_0 is the density at some (arbitrary) reference height z_0. As a consequence, the pressure will also be a function of height, using the ideal gas law $p = \rho kT$ we immediately see that:

$$\rho(z) = \rho_o e^{-mg(z-z_o)/kT} \tag{9}$$

where, again, the subscript '0' denotes the pressure at the reference height z_0. Equations 8 and 9 are known as the barometric law, and is often a good approximation for real gases, such as found in the Earth's atmosphere. The chemical potential, of an equilibrium system is constant, independent of height. From the potential distribution theorem we have for an ideal gas in an external field:

$$\mu'(z) = \mu_o = kT \ln \rho(z) - kT \ln < e^{-mg(z-z_o)/kT} > \tag{10}$$

$$= kT \ln \rho(z) - mg(z - z_o) \tag{11}$$

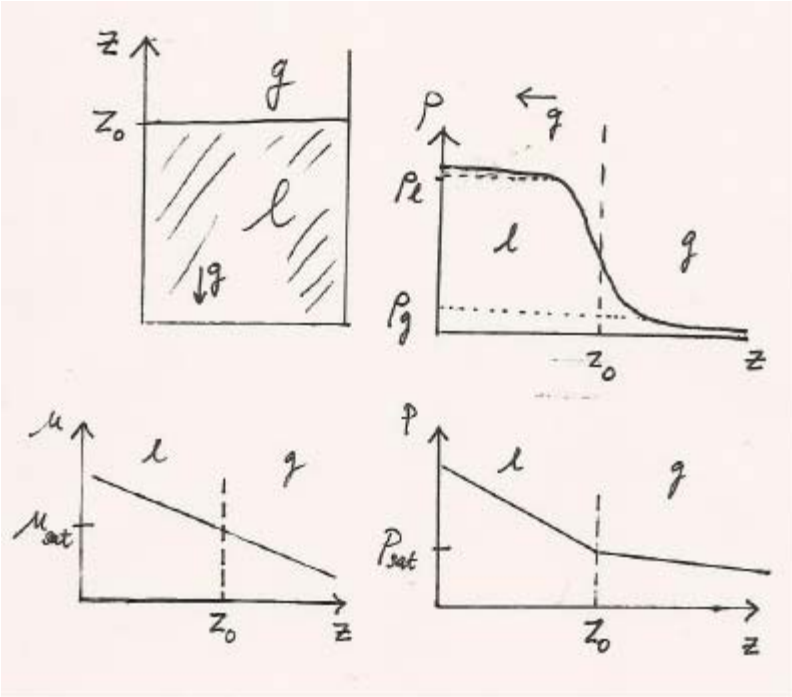

Figure 5: A schematic of liquid and vapor meeting at a planar interface (top left panel). The two coexisting phases meet at $z = z_0$. The top right panel shows the detailed density profile near the interface, where a rapid transition is seen from the coexisting

liquid density, ρ_l, to vapor density, ρ_g. Due to the presence of the gravitational field the density profile is strictly a monotonically decreasing function (exaggerated in the figure) of the height, *z*. For instance, $\rho(z) \rightarrow 0$ as $z \rightarrow \infty$. The bottom left panel shows the linear variation of the local chemical potential through the interface. The pressure variation is shown in the bottom right panel, based on a step profile approximation of the liquid-vapor profile.

From the ideal gas equation of state, $\mu = kT\ln\rho$, we immediately recognize the first term on the second line as the chemical potential of a bulk fluid (in the absence of a gravitational field) with a bulk density equal to the local density $\rho(z)$. Hence we can write

$$\mu'(z) = \mu(z) - mg(z - z_o) \tag{12}$$

which, formally, just serves to define the local chemical potential, $\mu(z)$. This definition of what is sometimes referred to as the 'intrinsic' chemical potential is applicable to all fluids, and not limited to the ideal gas.

For the special case of the ideal gas we find that $\mu(z) = \ln\rho(z)$, for any $V_{ext}(z)$. That is, for the ideal gas the functional relationship between the local chemical potential and the local density, is exactly the same as between the bulk chemical potential and the bulk density.

This is not generally true for non-ideal gases (i.e. interacting fluids), but still a good approximation when $V_{ext}(z)$ is slowly varying with respect to size of the molecules (strictly the fluid correlation length)[6]. A system that nicely demonstrates that the relationship between $\mu(z)$ and $\rho(z)$ can not always be the same as in the bulk is that of a hard sphere fluid at a hard wall. The hard sphere system has a maximum bulk density $\rho_{max} = sqrt(2)$, but local density near a hard wall can easily surpass that by an order of magnitude [7]. Hence there must be a different relation between the local chemical potential and the local density.

Of course, the gravitational field is a good example of a slowly varying field [4]. We will make use of that observation in the sections that follow.

4.2 interacting fluid in a gravitational field

As mentioned above, since the gravitational term is a one-body external field (independent of the fluid-fluid interactions), we can we can define the local chemical potential as

$$\mu(z) \equiv \mu'(z) - mg(z - z_o) \tag{13}$$

Since the gravitational field is slowly varying, we are also justified in assuming that the relationship between the local density (or local pressure) and the local chemical potential is the same as that for g = 0, i.e. given as by the bulk equation of state.

4.3 planar liquid-vapor interface

In practice, a realization of coexistence is manifested when the two phases are in contact at a planar interface. In the presence of gravity, the planar interface will be oriented perpendicular to the direction of gravity (which we will denote by *z*) and a vapor phase will be above the liquid, see figure 5. Not too close to the critical temperature such an interface appears as very a sharp transition, almost a step profile. However, there is some degree of diffusiveness on the molecular scale. The profile through the interface is well described by a *tanh(z)* profile, with a width that is roughly of the order of the molecular size: w = 0.5 − 3 nm, say.

For a liquid-vapor system in the presence of gravity it is convenient to choose z_0 as a point in the 'center' of the interface, i.e. where the density gradient, $\partial\rho(z)/\partial z$ reaches a maximum (see figure 5). At $z = z_0$ we have $\mu_0 = \mu_{sat}$, and $p = p_{sat}$. At any height, z, somewhere away from the interface the local fluid chemical potential is $\mu(z) = \mu_o - mg(z - z_0) = \mu_{sat} - mg(z - z_0)$. Thus, as we move away the location of the liquid-vapor interface the chemical potential continually varies in a linear fashion by an amount $-mg(z - z_0)$. Since the chemical potential is a monotonically increasing (typically non-linear) function of density, this implies that the density continually decreases with z, and increases in the direction of gravity. In practice, the density variation in the liquid is exceedingly small and thus hard to detect over the distances typical of a laboratory experiment.

In each phase, the pressure is also a linear function of height. This easily follows from the hydrostatic balance

$$\Delta p(z) = p(z) - p(z_0) = m\int_{z_0}^{z} dz\rho(z) \tag{14}$$

$$\approx mg\rho(z)(z - z_0); |z - z_0| \gg w \tag{15}$$

If z is located well inside the liquid phase, or well inside the vapor phase, but not too far on a gravitational length scale, i.e. $kT/mg \ll |z - z_0| \gg w$, we can assume that the local density. Hence, we can approximate the pressure difference as

$$\Delta p(Z) = \begin{cases} m\rho_l(z - z_0) \\ m\rho_g(z - z_0) \end{cases}; \begin{matrix} z < z_0 \\ z > z_0 \end{matrix} \tag{16}$$

It is interesting to note that the liquid-vapor system in a gravitational field represents a spatial manifestation of the equation of state. That is, if we start far above the planar interface, $z \gg z_0$ where $\rho \approx 0$ and move steadily down until $z \ll z_0$ we traverse the equation of state ($p(\rho)$, or $\mu(\rho)$) from low to high density along an isotherm. Or, to put it a different way, any state point in the (μ, p) plane (cf. figure 1) corresponds to a certain height, z, in the two-phase system.

5 Capillary rise and capillary depression

5.1 general considerations

When a capillary (e.g. slit or cylinder) is inserted into a planar liquid-vapor interface (located at z_0) one will observe that the liquid in the capillary equilibrates either above z_0 (rise), or below z_0 (depression), see figure 6 Capillary rise occurs when $\cos\theta > 0$ while a depression signals that $\cos\theta < 0$. Capillary rise is a phenomenon that was studied intensely starting during the times of Laplace, when explanations were sought for the observation that the rise in a cylinder is twice that of a slit with a width equal to the cylinder's diameter ($H = 2R$). It also led to the first estimates for the strength of intermolecular attractions.

Let us consider capillary depression for a slit-like geometry, as shown in figure 6 B. From the previous section we immediately can state that the local fluid chemical potential at the level of the mensicus, zM, is given by:

$$\mu(z_M) = \mu_{sat} - mg(z_M - z_0) = \mu_{sat} + mgh \tag{17}$$

using the shorthand notation $h \equiv z_0 - z_M$. This value, once combined with the equation of state, constitutes complete information regarding the densities, and pressures on either side of the meniscus [5].

Performing the hydrostatic balance at the meniscus, we find that the pressure on the liquid side and gas side are given by

$$p_l \approx p_{sat} + mg\rho_g(z_0 - z_M) \tag{18}$$

$$p_g^{\dagger} \approx p_{sat} + mg\rho_g(z_0 - z_M) \tag{19}$$

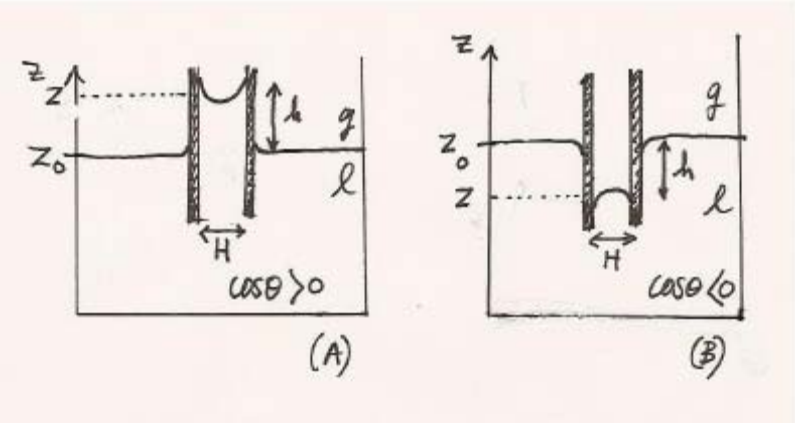

Figure 6: Capillary rise (left) or capillary depression (right) results when a capillary is inserted through a planar liquid vapor interface. Inner surfaces that prefer the liquid ($cos\theta > 0$) show rise while the reverse leads to depression. A measurement of the rise (depression) h combined with knowledge of $cos\theta$ and the surface tension instantly determines the shift of liquid-vapor transition for that H, see text

respectively. From this we find that the difference can be expressed as

$$p_l - p_g^{\dagger} = mg(\rho_l - \rho_g)(z_M - z_0) = mgh(\rho_l - \rho_g) \tag{20}$$

Combining this expression with Laplace's equation, $p_l - p_g^{\dagger} = 2\gamma_{lv}\cos\theta / H$, we obtain H as a function of $\Delta\mu$, ie.,

$$H(\Delta\mu) = \frac{-2\gamma_{lv}\cos\theta}{(\rho_l - \rho_v)mgh} \tag{21}$$

$$= \frac{-2\gamma_{lv}\cos\theta}{(\rho_l - \rho_v)\Delta\mu} \tag{22}$$

Where on the second line we used equation 17, $\Delta\mu = mgh$. This result is identical to equation 7 presented before and, moreover, this illustrates that capillary rise and capillary depression are, in fact, 'spatial' manifestations of capillary condensation and evaporation, respectively. This is because in the presence of gravity there is a one-to-one correspondence between the thermodynamic quantity $\Delta\mu$ and the spatial quantity h. Just as, in the presence of gravity, every height in a liquid-vapor profile corresponds to a unique fluid state point, every height inside the capillary corresponds to a unique capillary state point.

To be specific, at every height z we can instantly (and visually) determine which is the stable phase inside the capillary. Only for positions located between planar interface z_0 and the meniscus z_M, do we find that the phase inside the capillary is the 'opposite' of the bulk phase outside the capillary. Clearly then, if a capillary of fixed size, H, is inserted in a planar liquid-vapor interface a measurement of the rise or depression, h, instantly determines the shift of the phase transition

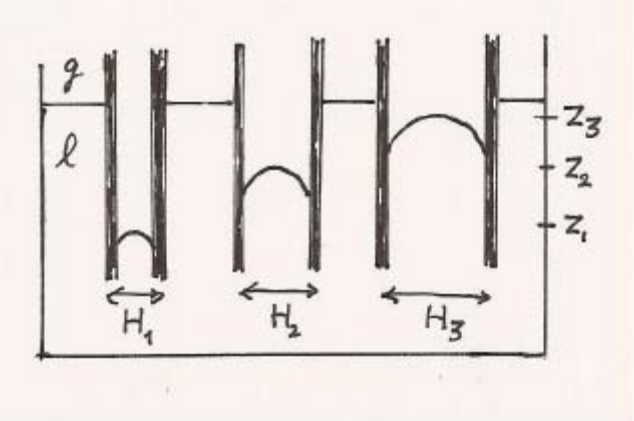

Figure 7: Capillary depression for various sized slit-like capillaries inserted through a planar liquid vapor interface. Different values of $\Delta\mu$ can be chosen by selecting different levels, e.g. z_1, z_2, z_3, which correspond to the crest of the mensicus, and determining for each level the width, H, of the unique capillary for which the meniscus level matches the selected level z.

for that value of H, viz.,

$$\Delta\mu(H) = \frac{-2\gamma_{lv}\cos\theta}{H(\rho_l - \rho_v)} \tag{23}$$

Conversely, a straightforward experimental determination of H in terms of $\Delta\mu$, i.e. H($\Delta\mu$), can be obtained by inserting a collection of capillaries of different widths, Hi, into a

planar liquid vapor interface, as illustrated in figure 7. One fixes $\Delta\mu$ by selecting a particular level z_i, and then determines the width of the capillary for which the mensicus is located at precisely at z_i. Such an experiment therefore would constitute the 'spatial' realization of equation 5

5.2 estimates for water

We are now in a position to make specific estimates for the capillary phase transitions described above. All that is needed are the physical properties of water. These are presented for a range of temperatures in table 1. Other constants needed are given in table 2. From the tables we calculate that the gravitational length $kT/mg = 1.404 \times 10^4$m = 14.04km, and for room temperature:

$$\frac{2\gamma_{lv}}{mg(\rho_l - \rho_v)} = 1.472 \times 10^{-5}\,\mathrm{m}^2; \qquad \mathrm{T} = 25\ ^{\circ}\mathrm{C} \tag{24}$$

It is useful to rearrange equation 22 to

$$Hh = -\frac{-2\gamma_{lv}\cos\theta}{mg(\rho_l - \rho_v)} \tag{25}$$

or,

$$Hh = \cos\theta \times 1.472 \times 10^{-5}\,\mathrm{m}^2; \qquad \text{at T} = 25\ ^{\circ}\mathrm{C} \tag{26}$$

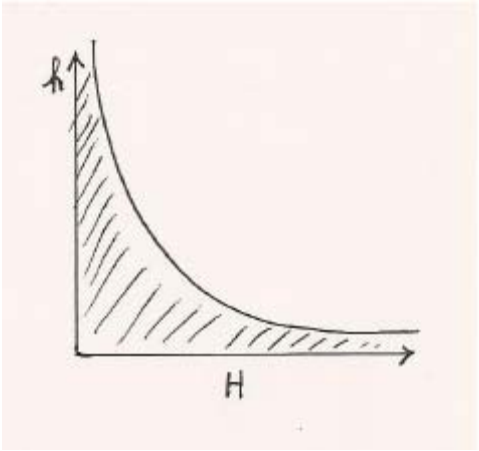

Figure 8: The relationship between the capillary width, H, and capillary rise (or depression), h is a hyperbola. A hyperbolic ("all or nothing") capillary is a capillary for which the width w is a function of the height ℓ, i.e., $w(\ell) = w\ell$. Completely wetting capillaries for which the product $w\ell$ falls inside the cross-hatched region, below the $Hh = c$ curve, are completely filled with liquid, otherwise the capillary will be completely empty (filled with vapor). The opposite result applies to completely drying capillaries.

Table 1: Physical properties of water at coexistence as a function of temperature

T °C	γ_{lv} dynes/cm $= 10^{-3}$N/m	ρ_l mol/m^3	ρ_g mol/m^3
10	74.22	55556	0.52214
20	72.75	55444	0.96117
25	71.97	55389	1.2801
30	71.18	55334	1.6886
40	69.56	55114	2.8417
80	62.60	53990	16.302

Table 2: Physical constants

k	1.38054×10^{-23} J K^{-1}
N_A	6.02252×10^{23} molecules/mol
g	9.80665 m/s^2
m	18 g/mol

Thus, for example, if θ = 45º and H = 1 mm we find that h = 1.04 cm. Similarly, for a superhydrophobic surface (θ = 170º) at a depth of h = 1 cm we obtain H = 1.45 mm.

It is interesting to note that equation 25 expresses the fact that the locus of capillary rise (or depression) conditions is a hyperbola in the h, H plane, given the fact that the right hand side of equation 25 is a constant for a given liquid, given temperature and given contact angle. This relationship is sketched in figure 8.

An amusing consequence of this geometric relationship is the behavior of a special shaped capillary. If the capillary has width w that is a function of the height `, such that w` equals a constant, c, then it follows that depending on the absolute dimensions this hyperbolic capillary will act as a 'binary' switch: it will either be completely filled or completely empty! If $c \le -2\gamma_{lv}\cos\theta / mg(\rho_l - \rho_v)$ then the capillary will be completely filled with liquid (i.e. for all h, [8]). If, on the other hand $c > -2\gamma_{lv}\cos\theta / mg(\rho_l - \rho_v)$ the capillary will be completely empty. The same is true for any capillary whose shape, w(ℓ), is such that it lies entirely under the hyperbolic curve sketched in figure 8. Finally, if the capillary shape cuts the hyperbole, the capillary will exhibit bands of liquid and vapor. An example of a linear function, w(ℓ) is shown in figure 8.

6 Effects of temperature

The temperature dependence of the capillary phase transition is of interest. We will start from equation 5 and consider the temperature dependence at a constant width *H.*

$$\left(\frac{\partial \Delta\mu}{\partial T}\right)_H = \frac{-2}{H}\frac{\partial}{\partial T}\left(\frac{\gamma_{lv}\cos\theta}{\rho_l - \rho_v}\right) \tag{27}$$

Two types of behavior can be expected, depending on the temperature regime. At high temperature, and above the drying temperature, T_D, we have $\cos\theta = -1$ for all T. Hence,

$$\left(\frac{\partial \Delta\mu}{\partial T}\right)_H = \frac{2}{H}\frac{\partial}{\partial T}\left(\frac{\gamma_{lv}}{\rho_l - \rho_v}\right); \qquad T > T_D. \tag{28}$$

We know that both lv, and the density difference $\rho_l - \rho_g$ decrease with T as both will vanish at the critical temperature T_c. However, γ_{lv} decreases more rapidly than does $\rho_l - \rho_g$, i.e. $\partial/\partial T\left[\gamma_{lv}/\rho_l - \rho_g\right] < 0$ and thus we expect $\Delta\mu$ to decrease with T, when $T > T_D$. For $T < T_D$, where $\cos\theta < -1$, we still have γ_{lv}, and $\rho_l - \rho_g$ decreasing with T. However, we also have to factor in $\partial\cos\theta/\partial T$. The latter is negative when $\cos\theta < 0$, and can be large in magnitude.

Alternatively, we can focus on the behavior of H with temperature, i.e.,

$$\left(\frac{\partial H}{\partial T}\right)_{\Delta\mu} = \frac{-2}{\Delta\mu}\frac{\partial}{\partial T}\left(\frac{\gamma_{lv}\cos\theta}{\rho_l - \rho_v}\right) \tag{29}$$

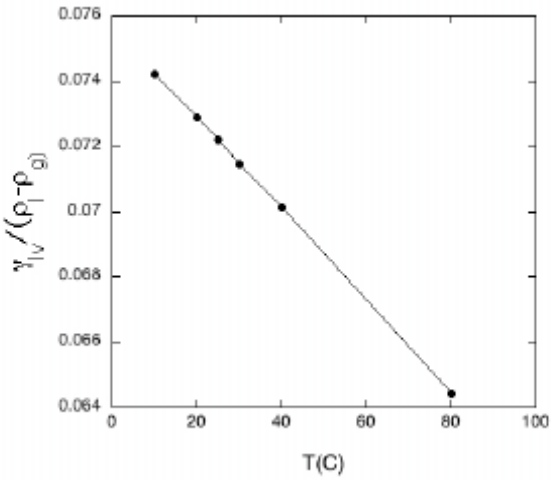

Figure 9: The temperature dependence of the ratio $\gamma_{lv}/m(\rho_l-\rho_v)$ for water. Over the range shown the ratio decreases by about 10 %.

7 Appendix A

7.1 Capillary Evaporation in a Slit

Following Evans [1] and Evans and Marini Bettolo Marconi [2] we first consider capillary evaporation in a slit of area *A* and width *H*, addressing other geometries toward the end of this section. We can derive an expression for the shift of the liquid-vapor transition by equating the grand potential of the two phases. In the limit of large *H* and large *A* the density profile of either phase is almost constant throughout the slit and hence we can consider the grand potentials of the fluid phases as the sum of two terms, a surface and a bulk contribution,

$$\begin{aligned}\Omega_l &= -p_l AH + 2\gamma_{wl}A \\ \Omega_g &= -p_g^{\dagger} AH + 2\gamma_{wl}A\end{aligned} \tag{30}$$

where p_l is the pressure of the bulk liquid (possibly in a reservoir) while $p_g^{\dagger}$ is the pressure of the gas phase at the same chemical potential. Such a gas phase would be metastable in the bulk, its density $p_g^{\dagger}$ would fall between the bulk coexisting densities. Capillary phase coexistence occurs when $\Omega_l = \Omega_v$, that is when

$$p_l - p_g^{\dagger} = \frac{2(\gamma_{wl}-\gamma_{wg})}{H} \tag{31}$$

It is convenient to expand the pressures $p(\mu)$ about the bulk coexistence values, p_{sat} and μ_{sat}, i.e. by using

$$p_l \approx p_{sat} + \left(\frac{dp}{d\mu}\right)_T^l (\mu - \mu_{sat}) = p_{sat} + \rho_l(\mu - \mu_{sat}) \tag{32}$$

$$p_g^\dagger \approx p_{sat} + \left(\frac{dp}{d\mu}\right)_T^g (\mu - \mu_{sat}) = p_{sat} + \rho_g(\mu - \mu_{sat}) \tag{33}$$

Here the densities, ρ_l and ρ_g, are those of the two coexisting bulk phases. Thus, upon combining equation 31 and equations 32 and 34 we obtain

$$\Delta\mu = \mu - \mu_{sat} = \frac{2(\gamma_{wl} - \gamma_{wg})}{H(\rho_l - \rho_g)} \tag{34}$$

which is equation 3 of the main text. Finally, note that equation 31 is a statement of Laplace's law, relating the pressure difference across a (here cylindrical) meniscus separating the bulk liquid from the gas phase inside the capillary. It is often rearranged to express H in terms of the pressure difference $\Delta p \equiv p_l - p_g^\dagger$ (see references [9, 10]),

$$\Delta\mu = \mu - \mu_{sat} = \frac{2(\gamma_{wl} - \gamma_{wg})}{H(\rho_l - \rho_g)} \tag{35}$$

as it allows a quick estimate of H. For example, using the liquid-vapor tension of Table 1 and $p_l \approx 1\text{atm} \approx 10^5\,\text{Nm}^{-2}$ and simply neglecting the vapor pressure gives $H \approx 1.4\mu\text{m}$.

7.2 Capillary Evaporation between two circular disks

We note that in the derivation of the preceding section we tacitly assumed that the only interfaces that contributed to the grand potential were the interfaces at the wall. Of course, there are also two liquid-vapor interfaces at the entrances of the pore. The derivation essentially assumed that these could be neglected, in other words the walls were infinite in extent. In many situations such assumptions are not justified, and hence in this section we specifically address the contributions of any liquid-vapor interfaces present.

As a representative example we will consider a slit of finite cross-sectional area A, consisting of two circular disks separated by a distance H. Once capillary evaporation

takes place there will be a liquid-vapor interface created of roughly cylindrical form, and area A_{lv}. Hence, the grand potentials of the liquid and gas phase now read,

$$\begin{aligned} \Omega_l &= -p_l AH + 2\gamma_{wl} A \\ \Omega_g &= -p_g^{\dagger} AH + 2\gamma_{wl} A + \gamma_{lv} A_{lv} \end{aligned} \tag{36}$$

while the condition for coexistence, $l = v$, becomes

$$\rho_l - \rho_g^{\dagger} = \frac{2\left(\gamma_{wl} - \gamma_{wg}\right)}{H} - \frac{\gamma_{lv}\left(A_{lv} / A\right)}{H} \tag{37}$$

from which we find (using equation 32 and 34) the shift of the liquid-vapor transition as,

$$\Delta\mu = \mu - \mu_{sat} = \frac{2\left(\gamma_{wl} - \gamma_{wg}\right)}{H\left(\rho_l - \rho_g\right)} - \frac{\gamma_{lv}\left(A_{lv} / A\right)}{H\left(\rho_l - \rho_g\right)} \tag{38}$$

Since γ_{lv} is always a positive quantity, the effect of the presence of the liquid-vapor interface is to reduce $\Delta\mu$, moving the capillary transition closer to the bulk transition. For the case of two circular disks, each of radius R_d, and assuming a cylindrical liquid-vapor interface, we have $A_{lv} / A \approx 2H / R$, and hence the last term of equation 38 reduces to

$$\frac{2\gamma_{lv}}{R_d\left(\rho_l - \rho_g\right)} \tag{39}$$

which, as expected, vanishes in the limit $R_d \to \infty$. Finally, expressing H in terms of $\Delta\mu$ leads to the following modification of equation 22

$$H\left(\Delta\mu\right) = \frac{-2\gamma_{lv}}{\left(\rho_l - \rho_g\right)\Delta\mu}\left[\cos\theta + \frac{H}{2R_d}\right] \tag{40}$$

8 Appendix B

8.1 Lum, Chandler and Weeks

Capillary evaporation is also the topic of a feature article by Lum, Chandler and Weeks [3]. These authors provide an estimate of when a separation of two hydrophobic plates is sufficiently small for capillary evaporation to occur. We quote the authors who state that:

The bounded liquid has an unfavorable surface energy proportional to the net surface area, where the surface tension, γ, is the constant of proportionality. This energy is counteracted by the favorable bulk free energy proportional to the average number of molecules in the bounded liquid, where the proportionality constant is the difference between liquid and gas chemical potential, $\mu_l - \mu_g$. For large enough D, provided $\mu_l - \mu_g < 0$, the bulk energy dominates over the surface energy, and the bounded liquid is stable. On the other hand, when D is less than the critical separation

$$D_c \approx \frac{2\gamma}{n_l \left| \mu_l - \mu_g \right|} \tag{41}$$

surface energy is dominant and the bounded liquid is destabilized with respect to the vapor. Here, n_l is the molecular density of the bulk liquid (the average number of molecules per unit volume). Accordingly, for water at room temperature and atmospheric pressure, $D_c \approx 100$nm.

We can directly compare the above expression with our equation 7. Neglecting the small gas density, and assuming that the contact angle represents complete drying, i.e. $\cos\theta = -1$

$$h = \frac{2\gamma_{lv}\cos\theta}{\Delta\mu\left(\rho_l - \rho_g\right)} \approx \frac{2\gamma_{lv}}{\rho_l\left(\mu(z) - \mu_{sat}\right)} = \frac{2\gamma_{lv}}{\rho_l mgh} \tag{42}$$

where $\mu(z)$ is the chemical potential of the liquid at a distance $h = z - z_0$ below the planar liquid-vapor interface (located at z_0), and where we have neglected the small density of the gas.

There are two issues that arise from this comparison. The first concerns the interpretation of Lum et al.'s difference between the liquid and the gas chemical potentials " $\mu_l - \mu_g$". As pointed out in the derivation of in Appendix A at the capillary phase transition the chemical potentials of liquid and gas ought to be equal. The discrepancy only disappears when we replace (or interpret) Lum et al.'s " μ_g" by μ_{sat}.

The second issue centers around arriving at a value for D_c. This requires one to assign a value to Lum et al.'s "$\mu_l - \mu_g$", or (hopefully equivalently) to our $\mu(z) - \mu_{sat}$. As pointed out in the text, the latter is directly related to the height, i.e., $\mu(z) - \mu_{sat} = -mg(z - z_0)$.

Hence we need to specify $z - z_0$, the distance below the planar liquid-vapor interface. It is clear that as $z \to z_0$ that $h \to \infty$.

References

[1] R. Evans, J. Phys.: Condens. Matter, 2, 8989 (1990)

[2] R. Evans and U. Marini Bettolo Marconi, J. Chem. Phys., 86, 7138 (1987)

[3] K. Lum, D. Chandler, J.D. Weeks, J. Phys. Chem. B., 103, 4570 (1999)

[4] At the other extreme lies van der Waals' treatment of the planar liquid-vapor interface, where the properties of the rapidly varying density through the interface are mapped onto the bulk equation of state.

[5] In particular, from $\mu(z)$ and the $\mu(p)$ curves of figure 1 we obtain ρ_l and ρ_g (strictly speaking, since the liquid is the stable bulk phase, this is $p_g^{\dagger}$). Inverting either $\mu(\rho)$ or $p(\rho)$ provides ρ_l and ρ_g. Note that according to Laplace's equation the pressure difference can be expressed in terms of the surface tension and the width H, that is we have $p_l - p_g = 2\gamma_{lv} / H$.

[6] An explicit, but usually approximate, expression linking $\mu(z)$ to the local density $\rho(z)$ can be written down in density functional theory of inhomogeneous fluids.

[7] J.R. Henderson and F. van Swol, Mol. Phys., 51, 991 (1984).

[8] Of course, there exists a cutoff when H approaches molecular dimensions (approximately 1nm) limiting the total rise in the hyperbolic capillary to about 14 km.

[9] J.L. Parker, P.M. Claesson and P. Attard, J. Phys. Chem., 98, 8468 (1994).

[10] V.S. Yushchenko, V.V. Yaminsky and E.D. Shchukin, J. Colloid and Interface Science, 90, 307 (1983).

[11] Handbook of Chemistry and Physics, 69TH edition, p F-33, (1988-1989).

SUPPLEMENTARY INFORMATION

Structure Property Relationship – In order to understand the complete structure property relationships of the modified SH aerogel, we performed phenomenological modeling based upon two models relating microscopic surface roughness to macroscopic contact angle. Table I shows the change in macroscopic contact angles (θ_f) with microscopic contact angle θ according to the models Onda et al. and Feng et al. Both are based on the fractal dimension (determined by GISAXS analysis); and in addition, the model of Feng et al. takes into account the fraction of the surface under the water droplet occupied by solid material or air (f_s and f_v determined by AFM tomography). Using the microscopic contact angle θ = 91° measured for a dense/smooth film of comparable composition to the SH film, we must use the Feng et al. model that accounts for areal fraction porosity f_v = 0.95 to explain the measured macroscopic contact angle $\theta_f \cong 160°$. This requires the water to penetrate ~42.4-nm into the SH surface.

Table I:

θ	θf (Onda et al)	θf (Feng et al)					
	l=0.032 L=0.2 (L/l)D-2 = 3.6	*f*s=0.4 *f*v=0.6	*f*s=0.3 *f*v=0.7	*f*s=0.2 *f*v=0.8	*f*s=0.1 *f*v=0.9	*f*s=0.05 *f*v=0.95	*f*s=0.01 *f*v=0.99
86	75.4	120.0	128.6	138.6	151.0	159.6	170.9
91	93.6	128.7	136.0	144.3	155.0	162.4	172.2
95	108.3	136.5	142.6	149.6	158.7	165.0	173.3
100	128.8	148.3	152.6	157.7	164.3	168.9	175.0
103	144.2	157.6	160.6	164.2	168.9	172.1	176.5
105	159.0	166.8	168.5	170.6	173.4	175.3	177.9

Patterned SH Surfaces– We developed a procedure to optically control wetting. Exposure of SH surfaces to UV light (using an uncoated mercury grid lamp) causes the macroscopic contact angle to vary continuously from

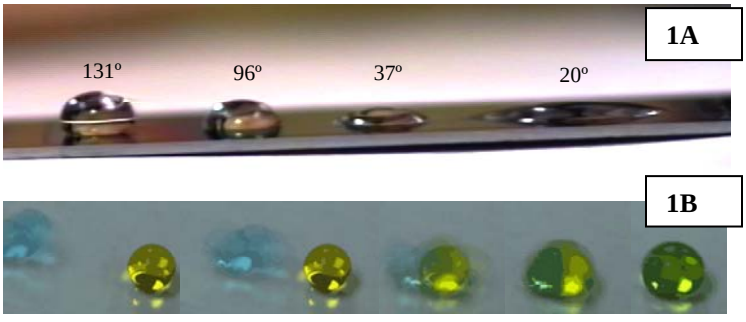

Figure 1. (A) water droplets on a UV/Ozone patterned SH surface after exposure of (from L to R) 2, 3, 4 and 5 minutes. (B) Directed droplet coalescence and mixing (of blue and yellow drops to form green) on a patterned SH surface.

about 160˚ to 0˚ depending on exposure time (see Figure 1A). UV light photolyzes oxygen forming ozone that removes perfluoro ligands on the SH surface, thereby decreasing the solid/liquid interfacial energy and increasing the solid/vapor interfacial energy. The result is a UV dose-dependent decrease in contact angle. Spatial patterning is achieved by UV exposure through a mask as for conventional lithography. This treatment changes the surface energy without affecting the surface structure – vapor phase exposure to a trimethylsilane restores the contact angle to nearly its original value. Patterning is of importance to define pathways for droplet motion, coalescence, and collection – see Figure 1B. We anticipate that patterned superhydrophobic/philic surfaces could effect mixing in capillaries by a convective advection process – overcoming a major limitation in microfluidic reactors and analysis systems.

The behavior of water or aerosol droplets impinging on an SH surface is a central issue that impacts particle collection and the (self-)cleaning of (bio-)contaminated surfaces as well as other applications such as water exclusion and inkjet printing. In general, water droplets will bounce off a SH surface, deforming on contact and reforming upon leaving the surface. The degree and the dynamics of droplet deformation are of great relevance to the removal of small foreign objects (Figure 2). The impacting droplet covers an area that is substantially larger than its size (dynamic spreading), and this effect can be exploited to collect and pre-concentrate foreign particles (e.g. spores) without any further mechanical contact or manipulation! Depending on the droplet's size and viscosity, as well as surface friction and impact velocity, a large variety of outcomes are possible, and these have been the focus of much recent fundamental work in this area. For similar reasons the understanding of the detailed nature of *lateral* motion of droplets, rolling and/or sliding is of equal importance. These phenomena and recent experiments have inspired us to perform molecular dynamics (MD) simulations of both bouncing and rolling.

MD simulations, using the Lennard-Jones potential, were initiated to study the dynamic behavior of droplets bouncing off SH surfaces as well as rolling down inclined SH surfaces. Droplet diameters ranging from about 6 nm to 32 nm were brought in contact with a planar wall, representing the surface. The interactions of the wall and the

fluid could be tuned to control the contact angle over the full range of 0º for complete wetting to 180º for SH surfaces. In addition, an optional dissipative force was added within approximately 1 nm of the wall. This latter force represents the friction that fluid molecules in contact with a surface experience. Finally, we added an optional one-body external field to account for the gravitational force.

Bouncing Droplets – Experimental observations (Richard et al. (2002)) using a high speed camera have shown that the contact time for bouncing droplets (of constant radius R) is *independent* of impact velocity, despite the wide range of deformations observed. In contrast, the collision's impact time is a strong function of R (i.e. ~ $R^{3/2}$). We conducted MD simulations to study the contact time behavior for nano-sized droplets, a size regime where conventional hydrodynamics might be expected to breakdown. A variety of sizes and impact velocities were studied, covering the *same* range of Weber ($We = V^2 R\rho\gamma$) numbers as probed in the experiments. An example of high impact velocity is shown in Figure 2. The drop is seen to flatten and spread over

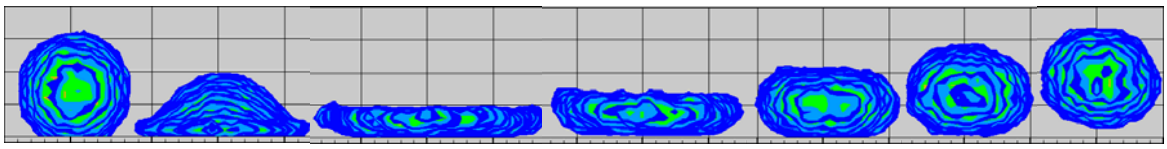

Figure 2. Snapshots of a 9.2 nm droplet bouncing on a SH wall. Time increases from L to R.

the surface to a diameter that is about twice the original size before reconstituting itself and lifting off. Observed contact times are collected in Figure 3, where we plot the contact time (t_c) as a function of drop radius (R). We note that the observed R dependence, ~$R^{1.66}$, is slightly stronger than what is predicted (and experimentally confirmed) for the continuum limit: ~$R^{3/2}$. The droplet's deformation upon impact varies widely with impact velocity. At small values of *We*, the droplets simply exhibit an ellipsoidal shape upon contacting the wall, but at high *We* the droplets are seen to spread into toroidal shapes that can even exhibit cavitation, or dry spots in the center. We find that lift-off first starts at the

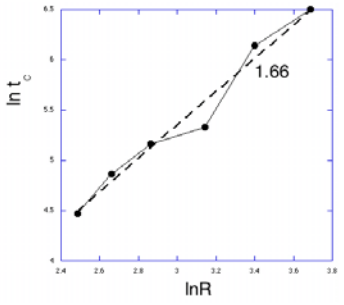

Figure 3 MD results of the contact time of a bouncing droplet for various droplet radii.

edge of the drop, and, at high *We*, the droplets will actually leave the wall while still in a deformed toroidal state. These results have implications for devising the most efficient particle collection strategies from SH surfaces.

Rolling Droplets – Recently, Mahadevan and Pomeau (MP) have provided several predictions for droplets on an inclined SH plane. Under the influence of gravity a droplet will start to move down the plane in a manner (sliding versus rolling) that has long been debated. MP distinguish droplets smaller (or larger) than the capillary length $a_c = (\gamma / mg\rho)^{1/2}$. Larger droplets flatten into a "puddle" shape of thickness $2a_c$, and reach a terminal velocity, V_0, that is, remarkably, found to be *independent* of either mass or gravity! Specifically, $V_o = 0.75(\gamma/\eta)\sin\alpha$, where α is the tilt angle, γ is the surface tension and η the viscosity. The terminal velocity stems from the balance of viscous dissipation and gravitational energy. An issue of great fundamental importance concerns the extent and the details of the dissipation region. The dissipation region of "puddle" drops coincides with the entire droplet (see predictions by MP). Smaller droplets ($R<a_c$) are expected to remain quasi-spherical, and their terminal velocity can *exceed* V_0. MP predict a dissipation region limited to the wall contact region with elsewhere a rigid-body rotation that induces zero dissipation, and this has been advanced as an explanation for why smaller droplets can move faster. (On traditional non-SH surfaces, so-called partially wetted surfaces, the drop *slides* and the velocity *increases* with R.) Quere et al. have confirmed some of the MP predictions for rolling mm-sized drops, but no microscopic information regarding the dissipation region has yet been obtained.

We have recently embarked on MD simulations of rolling droplets that are of nm size to investigate what modifications occur at the nanoscale due to the increased role of fluctuations and to identify in detail the nature of the motion and the extent of the dissipative region. Our initial calculation of the terminal velocity for a larger drop (i.e. $R>a_c$) agrees with MP. Density Functional Theory (DFT) calculations were performed to study the detailed contact between the fluid and a rough surface. The macroscopic contact angle was studied as a function of roughness to compare with the phenomenological Wenzell and Cassie predictions. The 3D calculations show that

small protrusions or ‘spikes’ on a surface, although partially wetting by themselves, can collectively support a droplet of sizes of about 5-10 times the spike width, with small pieces of liquid-vapor interface spanning the inter-spike gaps.

Rolling drops and Hydrofoil Experiments – An interface between a viscous fluid and a solid surface is usually characterized by a no-slip boundary condition, although the notion of possible slip on the boundary was introduced almost 200 years ago. Slip on the boundary can occur on a scale on the order of tens of nanometers, but the effects of this phenomenon are not appreciable for macroscopic flows. In countless applications, a limited slip boundary condition would be highly desirable. The motivations include drag and pressure drop reduction. We used our SH coating to investigate slip. The defining property of SH surfaces is a very high contact angle θ, measured as the angle between the plane of the surface and the tangent to the surface of a droplet resting on it: $\theta > 140$ [Fig. 1 (a)]. We show that in fluid flow near a textured SH surface (e.g., a drop moving down a grooved incline), due to this high θ, the contact area between the fluid and the surface is reduced, producing effective macroscopic slip on scales consistent with the characteristic size of the surface features.

Our basic notion of the flow behavior near a textured SH surface is illustrated in Fig. 1. The characteristic size of the texture is much larger than any surface roughness associated with the SH coating itself, but smaller than the capillary length (2.7 mm for water). The texture can be regular (grooves) or irregular (random peaks). The direct contact area between the surface and the fluid is limited to the protruding parts of the surface (mesas for the regular texture, peaks for the irregular texture), with free fluid surface areas above the depressed parts (grooves for the regular texture, valleys for the irregular texture). We assume that these areas exist because there is insufficient energy to deform the fluid boundary to bring it in contact with the entire surface [Fig. 1 (a)]. This will lead to a

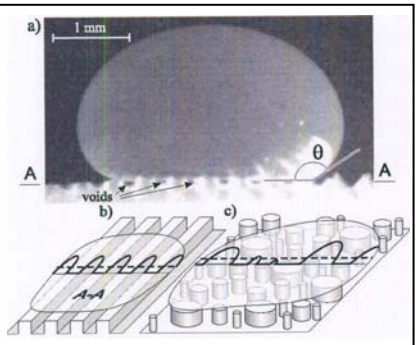

FIG. 1. Schematics of fluid behavior near a SH surface: (a) side view of a droplet on regularly grooved surface with voids (no-contact areas) and contact angle θ shown, *A-A* indicates the location of the plane of the nominal fluid boundary, (b) perspective view of the grooved surface showing fluid velocity profile in the *A-A* plane with the dashed line indicating average (i.e., slip) velocity, (c) perspective view of an idealized irregularly textured surface showing the fluid velocity profile and effective slip velocity at the fluid boundary.

velocity profile in the plane of the mesas with zero velocity in the contact area and nearly parabolic velocity distribution in the grooves. A velocity average at the nominal fluid boundary (the plane of the mesas) would be greater than zero [Fig. 1 (b)]. Similar behavior can be expected for an irregular texture [Fig. 1(c)], although the shape of the real-life boundary of the fluid in the latter case is likely more complicated.

For a flow inside a round pipe with alternating slip/noslip boundary condition, an analytical solution manifests nontrivial effective slip velocity. For a fixed ratio between the widths of the mesas and the grooves, this solution predicts effective slip to increase linearly with the mesa width. To visualize a plausible velocity distribution near a surface in partial contact with fluid, we conducted a simple finite element numerical simulation of a Poiseuille flow in a circular cross-section tube with alternating boundary conditions for a 1:1 ratio between the widths of the mesas (no slip) and the grooves (slip). The calculation shows effective slip increasing with the mesa width linearly in good agreement with the analytical results. Thus one should expect macroscopic effective slip velocity to emerge on the boundary as the no-contact areas reach macroscopic size (for water, at least microns).

In real life, the fluid boundary is not perfectly flat, and the patterns shown in Fig. 1 can only be sustained for feature sizes below a certain limit dictated by the capillary length. Moreover, surface deformation in areas above the protruding features (grooves, peaks) is likely to contribute to the overall energy balance of the flow above the surface. Thus one could expect some optimal size for the surface features that maximizes effective slip. An earlier investigation of textured SH surfaces indicates that the pattern of the texture influences the water-repelling properties of the surface, with a regular grooved design being optimal for surface drag reduction and maximization of effective slip, as confirmed recently. With these considerations taken into account, we conducted two simple experiments to benchmark the properties of smooth and textured SH surfaces.

In the first experiment, drops move down an inclined surface. The angle of the incline attached to a self-leveling support is measured with a high accuracy (up to 0.5 arc min). 20 cm long samples of materials are placed on the incline. At the elevated end of the sample, a syringe pump dispenses 1.5 mm radius drops. The working fluid is water or a mixture of water and zinc chloride.

The results of the trajectories are shown in Fig 2, for smooth and textured surfaces.

Drops move faster on textured surfaces, suggesting a combination of sliding and rolling motion with a nonzero effective slip. The second experiment is a study of water flow near a Joukovsky hydrofoil with chord length *L=4.3* cm, span 3.2 cm, and thickness 25% of the chord. The hydrofoil is installed in a water tunnel at a zero angle-of-attack and attached to a force transducer measuring the drag force. The flow speed *U,* can be varied to produce a range of Reynolds numbers $Re=UL/\rho$ from 1500 to 11000. The observed drag reduction is shown in Fig. 3. The drag reduction increases as Re drops (i.e. 2% at Re=11000 to 17% at Re=1500). The slip velocity is estimated at 1.4 cm/s at Re=11000 and 0.5 cm/s at Re=1500.

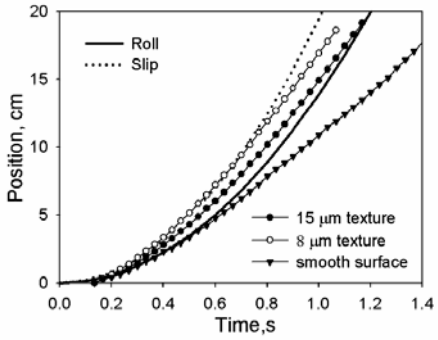

FIG. 2. Ensemble-averaged position of the drop rolling down the SH-coated surface vs time. Plots for each material are labeled in the graph. For reference, graphs for a solid-body rolling and frictionlessly sliding down the incline are also shown.

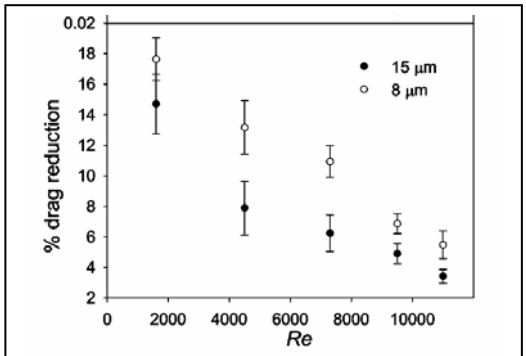

FIG. 3. Drag reduction on a SH coated Joukovsky hydrofoil for coated textured surfaces, using the smooth surface as a reference.

Anthrax Simulant pore removal – The Lotus plant illustrates that the ability of a surface to support rolling droplets is closely linked to self-cleaning. This is borne out for synthetic SH surfaces, where droplet rolling results in cleaning of 100 μm-sized particles. We are questioning whether rolling drops can be exploited to easily and efficiently remove small pathogens such as Anthrax spores. To investigate this three SH aerogel slides and three glass control slides were inoculated with approximately 10^6 organisms (Anthrax simulant spores, *Bacillus globigii)* from a spore suspension and allowed to dry for 4 days at ambient temperature. Three different extractions methods were used to remove the spores from the surface. In each case we found that the SH surface displayed superior removal than the glass slide controls. Following the removal

procedure, each slide was subsequently cultured to determine the amount of spores left behind despite the cleaning. Significantly, on the SH surface the extraction step showed no countable plates, indicating essentially 100% removal of spores. This finding could significantly impact and simplify the cleaning procedures employed for a wide variety of commonly encountered environments ranging from operation theaters to air ducts. We stress that cleaning by rolling droplet action provides inherent advantages compared to traditional rinsing methods. Most importantly, the picked up pathogens remain sequestered inside (or on) a small droplet, and are present at high concentration, thus allowing easy detection and/or further analysis.

Neutron Scattering – The nature of the water/SH surface is crucial to the realization of many practical applications of SH coatings. Of particular interest is understanding how this solid/liquid/vapor interface controls phenomena such as rolling instead of sliding of individual droplets and avoiding the nearly ubiquitous no-slip boundary condition. While scanning electron microscopy (SEM) and atomic force microscopy (AFM) have been used to image SH surfaces in air, a non-invasive technique like x-ray or neutron scattering is required to study the buried water-SH film interface. Neutrons are particularly useful for such a study due to their large penetration depth, isotopic sensitivity and ability to contrast match portions of the system. Neutron reflectivity (NR) has been used to study buried thin-films and their interfaces, it provides information about the scattering length density, thickness and interfacial roughness of different layers in a system.

We used neutron reflectivity to elucidate the properties of SH films in contact with water. UV/ozone treatment is used to vary the water contact angle and understand the resulting effect on the SH film interaction with deuterated water (D_2O). By comparing AFM results, DFT simulations and NR we arrived at the location, width and nature of the SH-water

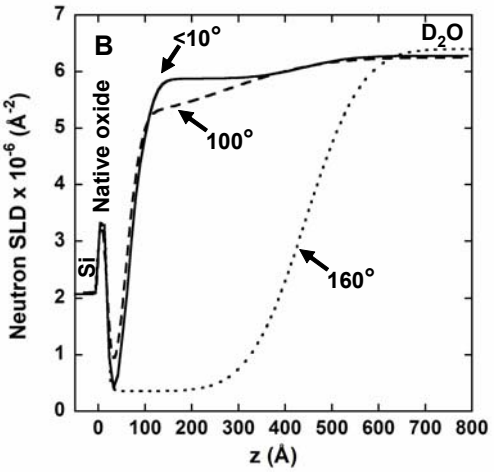

FIG. 4. Scattering length density (SLD) profiles obtained from normalized Fresnel NR data for films with different contact angles in contact with D_2O.

interface. UV/ozone treatment was performed to photocalcine the organic ligands. The time of exposure controlled the surface occupancy of the CH_3 and CF_3 groups, thereby adjusting the apparent contact angle, θ^{α}, while maintaining constant porosity, Φ_s and roughness. The Neutron reflectivity measurements were performed on the SPEAR beamline, a time-of-flight reflectometer, at the Manuel Lujan Neutron Scattering Center, Los Alamos National Laboratory. The scalar value of the momentum transfer vector Q_z is determined from $Q_z=4\pi*\sin(\alpha)/\lambda$, (where α is the angle of incidence measured from the sample surface and λ is the wavelength of the probe) and its range is covered by performing measurements at two angles of incidence, typically 0.5°and 2.5°. SH films were spin coated onto 10 cm diameter, 6 mm thick silicon substrates. Spectroscopic ellipsometry measurements indicate a film thickness of 440 Å and a refractive index, n_f = 1.1188. Sessile drop contact angle measurements on SH films indicate an apparent water contact angle of 158 ± 2°. Our NR experiments combined with additional structural analyses and molecular simulations have established the nature of rough silica surfaces submerged in water or exposed to 100% RH. For SH surfaces characterized by water contact angles ~ 160˚, water penetrates to a depth of about 100 Å, which is on the order of the surface roughness probed by AFM. At this level of penetration the interface comprises about 5% of solid, and the interface is defined by the topology of the pinned solid/liquid/vapor contact points. Using 5% of solid and 91˚ for θ, we derive an apparent contact angle of 154˚ from the Cassie Baxter relationship. Complete removal of hydrophobic ligands via photo-calcination (θ < 10˚), while preserving the roughness, should yield $\theta^{\propto}$ > 130˚ according to the Cassie-Baxter relationship. However, this is not observed which suggests that we are in the Wenzel regime. The inherent presence of air in the porous aerogel films may be a contributing factor for the validity of the Cassie-Baxter regime, but, when the hydrophobic ligands are removed, the Wenzel regime is thermodynamically favorable. This mix of trapped air and surface roughness makes these films an interesting system to study from a theoretical viewpoint. Observing such a high water contact angle for a film <500 Å thickness is remarkable when compared to micron scale roughness required by previous by studies and also observed in nature. Photocalcination procedures allow, change in surface chemistry with minimal effect on surface topography. A systematic trend of increased water infiltration with decreasing surface coverage of the hydrophobic ligands is observed.

Surprisingly, a ~35 Å buried layer with low scattering length density is observed in photocalcined films. Its origin is not well understood and will be the subject of future investigations.

Macroscopic Flow Experiments – A zero slip velocity at solid-liquid interfaces (the no-slip boundary condition) has long been held as an empirically proven law of fluid mechanics. SH coatings may allow for the relaxation of this constraint. The implications of this are far-reaching. For example, one could passively impose boundary conditions on fluids in microfluidic devices to enhance transport phenomena such as mixing. The hypothesis in this work is that wall slip is in reality apparent slip caused by the fact that on a rough SH surface only a small fraction of the fluid is in contact with the solid, while the remaining fraction is separated from the solid by vapor pockets that may contain air. To test this hypothesis, a number of experiments were performed. First, a self-leveling inclined plane with finely adjustable inclination angle was built. As shown in Figure 6, small drops of fluid were allowed to roll/slip down the inclined plane and were tracked using purpose-designed digital tracking software. The fluid flow inside the droplet is a complex combination of deformation and rolling motions. An order-of-magnitude analysis of this motion was recently performed by MP. Several experiments were conducted with this apparatus. In particular, the motion of drops of varying viscosity rolling and/or slipping along SH surfaces of various kinds was recorded and analyzed. In all cases, the drops reached terminal velocity, consistent with the MP theoretical predictions. This is due to the fact that shearing within the drop eventually absorbs energy at the same rate as the reduction in potential energy due to the loss of elevation of the drop. The surprising finding is that the energy dissipation for rough surfaces (with a lower fraction of fluid/solid contact area) is higher than for smooth surfaces.

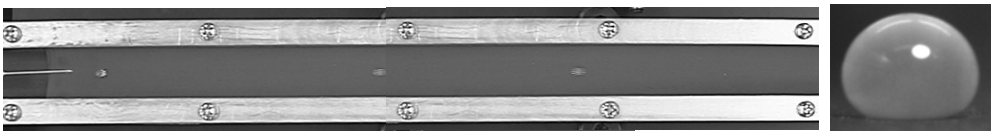

Figure 6 Experimental setup for rolling droplets (left) show three superimposed droplet images from which we determine the (terminal) velocity. A large 1:1 water:$ZnCl_2$ drop deformed due to gravity (right).

A more direct measurement of apparent slip can be made with a simpler velocity field. One of the simplest velocity fields is that found in a cone-and-plate viscometer,

where the shear rate is everywhere constant. Measurements of apparent viscosity were made with untreated (hydrophilic) plates, plates with a smooth SH coating and plates with SH surfaces of varying roughness. In this case, the results are in accordance with expectation. The untreated and smooth SH surfaces result in the same apparent viscosity. On the other hand, the apparent viscosity of the rough surfaces is approximately 5% lower.

Microfluidic devices – Fused silica microcapillaries and Si/glass microfluidic channels were successfully coated with SH surfaces with contact angles up to 160 degrees. Slip velocities were deduced from pressure measurements in the range of 0.1 to 1 psi at various flow rates in the capillaries and channels, but up to this point significant slip was not found. This may be due to coating damage inside the capillaries. In the no-slip limit, the terminal settling velocity is just 2/3 the velocity for the full-slip condition.

QCM Experiments – In collaboration with Cairncross at Drexel University, we initiated a set of new acoustic experiments to interpret the interface between an SH surface and water response. We used a Multiresonant Acoustic Interfacial Biosensor (MAIB) consisting of a Thickness-Shear Mode quartz crystal dip coated with a SH film and exposed it to deionized (DI) water. The film thicknesses ranged from 510 to 600 nm, with refractive indices of 1.12 – 1.16 and a contact angle of 144°-155°. In addition, some of the films contained 2 wt% silica nanoparticles to enhance the scale of the surface roughness. The acoustic characteristics, including the resonant frequency, attenuation, and frequency range (harmonics) were determined for SH surfaces in contact with air or a 4mm thick layer of water. Each MAIB was then loaded with 200 ml of DI water, which creates a film of approximately 4mm in thickness. This was followed by another measurement of the acoustic characteristics, and the changes in frequency, attenuation and phase were then recorded for four harmonic frequencies. The initial results show that films with larger contact angles and 2 wt% silica nanoparticles and treated with HMDS (hexamethyldisilazane) exhibit negligible changes in the acoustic characteristics. This is consistent with the presence of microslip.

Dielectrophoretically Controlled Micro-Droplet Reactors – Single droplets can be manipulated by dielectrophoresis using non-uniform electric fields. Droplets can be held in place or directed to move around by applying an AC current. Directed motion of water drops on SH surfaces has enormous potential for containerless sensing systems and micro-reactors, which could be used for synthesizing a novel class of materials. Our current SH coatings show rolling angles of > 20° for 50-80 mg droplet sizes due to the inherent roughness in the aerogel based coating. However, for our SH surfaces to become a useful tool for dielectrophoretic directed motion, the rolling angle needs to be reduced to 1-5° for droplet sizes of a few hundred nano-liters. In general, dielectrophoretic applications require thinner SH films with small rolling angles. Since the degree and scale of roughness have a dramatic influence on the rolling angle, we focused on the use of diamond lapping films which can be readily obtained with varying roughness (0.5-30 μm). These films were coated with a SH film, and rolling angles in the range of 2-9º were measured. To enhance roughness and further reduce the rolling angle, we have also tried imparting diamond lapping-like roughness in our SH coating by using silica particles of different sizes. So far, minimum rolling angles (5-9°) are observed for 10 μm diameter silica particles (<0.01 wt%).

IFM Experiments – Interfacial force microscopy (IFM) was used to examine synthetic aerogel like SH films (with measured contact angles of greater than 165º and a contact angle hysteresis between 2-5º) underwater. We discovered a very-long-range hydrophobic attraction that was due to out-of contact evaporation, or 'cavitation', of the intervening water at tip-to-substrate separations ranging from 0.8μm to as much as 3.5μm. Cavitation is a first-order phase transition characterized by a sudden, strong attractive force and by the appearance of a vapor bridge spanning the tip-to-substrate gap. Pre-existing 'nanobubbles' of a size commensurate with the interaction length have been proposed as a source of long-range interactions. We therefore used *in situ* confocal imaging to

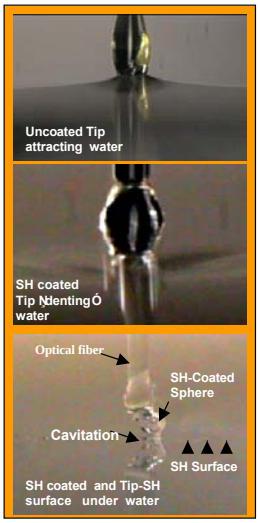

Figure 5 IFM experiments with uncoated (top) and SH-coated (middle and bottom) tips. Cavitation is seen in the bottom panel.

search for bubbles on an isolated, flat SH surface. Neither the microscopy nor neutron reflectivity experiments provide evidence for bubbles — certainly not micrometer-sized bubbles. We therefore argue that cavitation is a consequence of, and thermodynamically consistent with, the properties of confined water. The critical separation, *D*, below which cavitation is thermodynamically favored can be estimated from Laplace's equation as 1.4μm: this is a lower bound and will increase if Δp, the pressure difference across the interface, is reduced by incorporation of air into the cavity.

Cavitation – When two submerged SH surfaces are brought together sufficiently close a phase transition from liquid to vapor will take place inside the gap. This phenomenon is known by various names, but commonly referred to as capillary condensation or cavitation. We studied cavitation with the Interfacial Force Microscope (IFM), and observed the formation of a vapor bridge that started at an unusually large surface-to-surface distance, ~1-2 mm. These experiments motivated us to look at this phenomenon in model setting, i.e. with a molecular dynamics simulation. The simulations were performed for a planar slit consisting of two planar walls in the z-direction with periodic boundary conditions applied top the remaining x- and y- directions. The walls were made 'hydrophilic', preferring the liquid phase, by making them sufficiently attractive. Running the simulation in the NVT ensemble, with a constant number of particles, N, and choosing an overall density inside the liquid-vapor bulk coexistence envelope results in a liquid bridge spanning part of the gap, separated on both sides from the vapor phase by a curved meniscus. We then

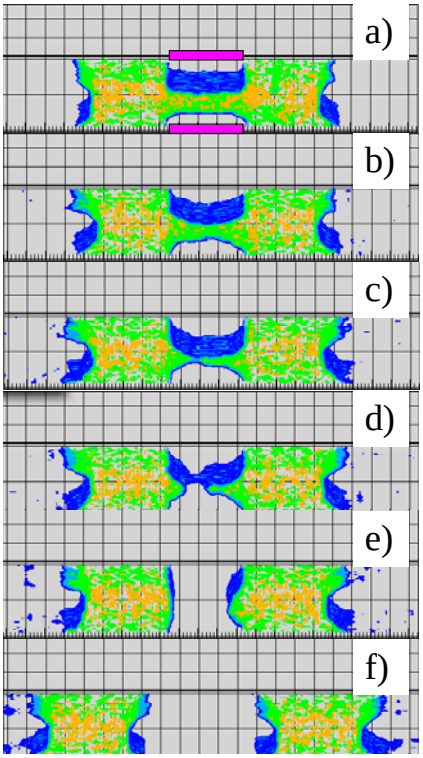

FIG. 5 Molecular dynamics results of cavitation inside a capillary slit. At time is zero a SH patch is created on the walls of an otherwise hydrophilic slit. The SH patch stimulates the growth of two vapor bubbles (a-c), separated by a thin liquid bridge. The liquid bridge ruptures (c-d) corresponding to cavitation. Panel (f) shows the final equilibrium state when all menisci have reached the correct curvature.

modified the wall-fluid interaction along part of the wall, thus creating a SH strip (indicated in Fig 5a). This instantaneous surface modification sets in motion a change in the liquid distribution (see Fig. 5) that culminates in the formation of a vapor bridge, i.e. cavitation. The formation of the vapor bridge proceeds through several stages. It starts when at each wall a thin layer of vapor emerges (Fig. 5a) that starts to grow in thickness. The shape of each vapor layer morphs into a (horizontal) curved meniscus (Fig. 5b) that, because of chemical and hydrostatic equilibrium must approach the same radius of curvature as the outer (vertical) menisci near the capillary end. Depending on the relative dimensions of the width of the SH patch and the capillary gap size, the bottom and top menisci will be separated by a thick or thin liquid bridge. Large fluctuations of the bridge are observed during the simulation. For the sequence shown the liquid bridge that separates the vapor bubbles ultimately ruptures and cavitation takes place (Fig. 5d). At this point (Fig. 5e) the capillary liquid has been cleaved into two separate parts. The horizontal menisci have been replaced by two new vertical ones, whose initial curvature is not the equilibrium curvature, as it has clearly has the opposite sign. The equilibration that follows consists of the new menisci rapidly adopting their proper curvature while the newly created cavity rapidly expands, thus re-establishing hydrostatic and chemical equilibrium as evidenced by the uniform curvature of all menisci present (Fig. 5f).

Bio-films – Bio-films are composed of populations or communities of microorganisms adhering to environmental surfaces. These microorganisms are usually encased in an extra cellular polysaccharide that they themselves synthesize. Their development is most rapid in flowing systems where adequate nutrients are available. The presence of microbial bio-films translates into a cost of billions of dollars incurred yearly in the form of equipment damage, product contamination, energy losses and medical infections. The literature suggests, when a clean sterile glass slide placed in a stream of water containing at least minimal nutrients, typically, within minutes, an organic monolayer adsorbs to the surface of the slide substrate. This changes the chemical and physical properties of the glass slide. The adsorption process is influenced by various physical forces (electrostatic, van der Waals) although the precise nature of the interaction is still a matter of intense debate. In order to understand the adhering mechanism, we developed a simple test, immersing a

clean sterile glass slide and hydrophobic coated glass slide in a Tryptic soy broth inoculated with E.Coli for seven days. To enhance visual effects under light microscopy, glass coupons were stained with red color Gram Safranin. Preliminary results (Figure 1) indicate that the hydrophobic coated glass slide did not exhibit any stains. This clearly indicates that the hydrophobic coating has inhibited (or completely stopped) the mechanism of bio-film formation. Future experiments will focus on determining what degree of hydrophobicity represents an optimal choice for the coating of the glass.

Publications

Kwoun, SJ; Lec, RM; Cairncross, RA; Shah, P; Brinker, CJ., *Characterization of superhydrophobic materials using multiresonance acoustic shear wave sensors*, IEEE TRANSACTIONS ON ULTRASONICS FERROELECTRICS AND FREQUENCY CONTROL; AUG 2006; v.53, no.8, p.1400-1403

Singh, S., Houston, J., van Swol, F., Brinker, CJ., "*Superhydrophobicity - Drying Transition of Confined Water*", NATURE, v.442(3) p.526, 2006.

Truesdell, R; Mammoli, A; Vorobieff, P; van Swol, F; Brinker, CJ; *Drag Reduction on a Patterned Superhydrophobic Surface;* Physical Review Letters volume 97 issue 4, page 044504. (2006)

Challa, S.; van Swol, F; *Molecular Simulations of Lubrication and Solvation Forces,* Phys. Rev. E.73, 016306 (2006)

Doshi, D., Shah, P., Singh, S., Branson, E.D., Malanoski, A.P., Watkins, E.B., Majewski, J., van Swol, F., Brinker, C.J., *Investigating the interface of superhydrophobic surfaces in contact with water*, Lagmuir; 21(17) p.7805, 2005.

Presentations

Brinker, CJ.; *Bridging the Gap: Observation of ultra long-range hydrophobic interactions*, ACS National meeting, Sept 11, 2006.

Brinker, C.J.; *Evaporation Induced Self-Assembly of Porous and Composite Nanostructures*, Argonne National Laboratory Center for Nanoscale Materials, Sept, 2006, Dedication of new center for nanoscale materials.

Brinker, CJ.; *Evaporation Induced Self-Assembly of Porous and Composite Nanostructures*, University of Virginia, March 3, 2006, Distinguished Alumnus Award Address

van Swol, F.B.; *Superhydrophobic Surfaces: Bouncing and Rolling droplets*., Pacifichem 12/17/2005; Honolulu, HI.

van Swol, F.B; Challa, S.; *On the interplay between hydrodynamic and solvation interactions.*, Pacifichem 12/18/2005; Honolulu, HI.

van Swol, F.B.; *Molecular Simulations of Lubrication and Solvation Forces.*, ASCR, LANL, 08/23/2005; Los Alamos, NM. Invited

Challa S. R.; van Swol F.; "*The Interplay of Solvation Forces with Lubrication Forces in Thin Gaps*", 58th Annual Meeting of the APS Division of Fluid Dynamics, Chicago, Illinois, Nov. 20-22, 2005

Challa S. R.; van Swol F.; "*Influence of Solvation Forces on Material Characterization*", 17th Annual Rio Grande Symposium on Advanced Materials, Albuquerque, New Mexico, Oct. 11, 2005

Distribution

1	MS1349	Eric D. Branson, 1815
1	MS1349	Seema Singh, 1815
1	MS1349	Frank van Swol, 1114
3	MS1349	Carol S. Ashley, 1815
1	MS1415	Jack E. Houston, 1114
1	MS1349	C. Jeffrey Brinker, 1002
2	MS9018	Central Technical Files, 8944
2	MS0899	Technical Library, 4536